Investigation of High Latitude Ionospheric Irregularities Utilizing Modeling and GPS Observations

Kshitija B. Deshpande

Dissertation submitted to the faculty of the
Virginia Polytechnic Institute and State University
in partial fulfillment of the requirements for the degree of

Doctor of Philosophy
in
Electrical Engineering

C. Robert Clauer, Chair
Gary S. Bust
Gary S. Brown
Wayne A. Scales
Timothy Pratt
John H. Simonetti

3 June 2014
Blacksburg, Virginia

Keywords: Ionosphere, Irregularities, High Latitude, GPS, Modeling, SIGMA

Investigation of High Latitude Ionospheric Irregularities Utilizing Modeling and GPS Observations

Kshitija B. Deshpande

ABSTRACT

Complex magnetosphere-ionosphere coupling mechanisms result in high latitude irregularities that are difficult to characterize. Until recently, the polar and auroral irregularities remained largely unexplored. Inadequate infrastructures to deploy and maintain advanced dual frequency Global Navigation Satellite System (GNSS) receivers at high latitudes, especially in the Southern hemisphere, makes such an investigation a formidable task. Additionally, the complicated geometry of the magnetic field lines in these regions pose challenges in designing global scintillation models. This dissertation takes some steps towards bridging these gaps while advancing the state-of-the-art high latitude irregularity studies.

In the first part of this dissertation, we briefly describe the Autonomous Adaptive Low-Power Instrument Platforms (AAL-PIP) experimental setup. These space science instrument platforms are being deployed in remote locations in Antarctica, improving the coverage of GNSS data availability. We explain in detail the method developed for analyzing high rate (typically 50 Hz) data from a novel dual-frequency Global Positioning System (GPS) receiver called Connected Autonomous Space Environment Sensor (CASES). We also report first observations from CASES at high latitudes. From this study, we established that CASES can be reliably used as a science grade GPS scintillation monitor.

Following this, a novel three dimensional (3D) electromagnetic (EM) wave propagation model called "Satellite-beacon Ionospheric-scintillation Global Model of the upper Atmosphere" (SIGMA) was developed to simulate GNSS scintillations on ground. GPS scintillation simulations of significantly high fidelity are now possible with this model. While the model is global, it is the first such model which accounts for the complicated geometry of magnetic field lines at high latitudes. Using SIGMA, a sensitivity study is presented to understand the effect of geographical, propagation and irregularity parameters on the phase scintillations. This allows us to reduce the dimensionality of the design space while solving the inverse problem described next.

In the final part, we utilize the tools developed for GPS measurement analysis and SIGMA to characterize the high latitude irregularities. We propose an inverse modeling technique to derive irregularity parameters by comparing the high rate (50 Hz) GNSS observations to the modeled outputs. We consider interhemispheric high latitude datasets for this investigation. We also implement SIGMA for analyzing a substorm event observed by AAL-PIP stations. One of the unique contributions of this research is to demonstrate that such an inverse modeling technique can form a basis in the investigation of the ionospheric irregularities. Moreover, availability of ample auxiliary data from multi-instrument observations can assist in this quest of understanding the physics of high latitude irregularities and their generation mechanisms.

To my better half, Mandar.

Acknowledgments

I would like to start by expressing my deepest gratitude to my advisors Dr. Bob Clauer and Dr. Gary Bust. Their patience, encouragement, and immense knowledge were key motivations throughout my graduate studies. I would not have imagined having any better mentors for my research. This dissertation would not have been possible without their constant support and confidence in me. I would also like to thank Dr. Scales, Dr. Brown, Dr. Simonetti and Dr. Pratt for accepting to be on my committee, for their encouragement and valuable suggestions.

My sincere thanks go to many friendly colleagues and collaborators without whom I could not have completed my work. After interacting with numerous researchers during plenty of conferences and meetings, I believe Space Science is the friendliest research field. I feel lucky to be a part of this area and especially, Space@VT group. I would especially like to mention Dr. Hyomin Kim for advising me in every possible aspect of research life. I would like to thank Dr. Dan Weimer, Dr. Xia Cai for their guidance whenever I needed. My experience with the AAL-PIP project has taught me a lot of organizational and interpersonal skills. Some of my life-long memorable experiences are from Antarctica. During this time, I thoroughly enjoyed working with my colleagues Joseph Macon and Dr. Zhonghua Xu. I am thankful to Steve Musko for preparing me for the AAL-PIP ground operations. Without his perfect coaching, I could not have been confident in operating these remote systems on the other end of the world while sitting at my desk. I would like to acknowledge Maitrayee, Kalyani, Shubhangi, Shvetha, Debbie Collins and Nancy Goad. They have been like a surrogate family, bearing the brunt of the frustrations, and sharing in the joy of the successes. I more than thankful to Dr. Kathleen Meehan, John Harris, Branden McKagen, Pankaj and many others who have been my well

wishers at my second home Blacksburg.

I have spent most of my grownup life in the United States. Friends and family here helped me never miss my home country. I would like to thank Priyanka, Mausami, Trupti, Niyati and Vinaya for always believing in me and my abilities. Similarly, my *dadas* Wasim, Prasun, Sameer, Parag have always motivated me throughout my endeavors.

I cannot express my gratitude and love in words to my husband, Mandar. I feel blessed to have him in my life. He truly has been the driving force behind me and this Ph.D. I would like to dedicate this dissertation to him. Finally, I am deeply thankful to my parents, in-laws and sisters Shreya and Kavita for supporting me in innumerable ways. Both my parents and in-laws have been extremely patient with us and encouraging during all this time. My thanks also goes to little Aarya for encouraging her aunt to study.

I would like to acknowledge the National Science Foundation for supporting this research under grants ANT-0839858, ATM-922979, ANT-0840650 and PLR-1243398.

ATTRIBUTION

Several colleagues aided in writing, figures, providing data and research behind four of my manuscripts presented as chapters 2, 3, 4 and 6 in this dissertation. A brief description of their contributions is included here.

Gary S. Bust, PhD (The Johns Hopkins University Applied Physics Laboratory (JHUAPL), Laurel) is a Research Scientist at JHUAPL. He was a co-author for Chapters 2, 3, 4 and 6, and is the principal investigator for some of the NSF grants supporting this research. Dr. Bust has provided guidance for the research on processing of CASES data, SIGMA model, and its use in inverse modeling. He has also provided some text in the discussion section of Chapter 3, IDA4D figure for Chapter 4 and contributed editorial comments.

C. Robert Clauer, PhD (Space Science, Electrical and Computer Engineering (ECE) Department, Virginia Tech) is a Professor of Space Science at Virginia Tech. He was a co-author for Chapters 2, 3, 4 and 6, and is the principal investigator for the NSF grants supporting this research. Dr. Clauer has provided guidance for the substorm research in Chapter 6 and contributed editorial comments.

Hyomin Kim, PhD (Space Science, ECE Department, Virginia Tech) is Research Associate at Virginia Tech. He was a co-author on Chapters 2 and 6, and was a part of the team that deployed the AAL-PIP systems in Antarctica. Dr. Kim also provided some plots for Chapter 6 and editorial comments.

Joseph E. Macon (ECE Department, Virginia Tech) was a Masters student at Virginia Tech. He was a co-author on Chapter 2 and was a part of the team that deployed the AAL-PIP systems in Antarctica. Joseph also contributed editorial comments.

Todd E. Humphreys, PhD (Aerospace Engineering and Engineering Mechanics (AE-EM) Department, University of Texas (UT) at Austin) is an Assistant Professor at the UT at Austin. He was a co-author on Chapter 2 and has been involved in the development of the CASES GPS

receiver. Dr. Humphreys also contributed editorial comments.

Jahshan A. Bhatti, (AE-EM Department, UT at Austin) is pursuing PhD at the UT at Austin. He was a co-author on Chapter 2 and has been involved in the development of the CASES GPS receiver.

Steve B. Musko, (Department of Atmospheric, Oceanic and Space Sciences, University of Michigan, Ann Arbor) is Engineer in Research Lead at University of Michigan. He was a co-author on Chapter 2 and has been involved in the development and support of AAL-PIP systems. He has also provided ground support training and some codes mentioned in Chapter 5.

Geoff Crowley, PhD (Atmospheric & Space Technology Research Associates (ASTRA), Boulder) is the President/Chief Scientist at ASTRA. He was a co-author on Chapter 2 and has provided support for CASES receivers. Dr. Crowley also contributed editorial comments.

Allan T. Weatherwax, PhD (Physics Department, Sienna College) is a Professor of Physics and the Associate Dean of Science at Siena College, NY. He was a co-author on Chapters 2 and 4. Dr. Weatherwax has provided Novatel GPS data for Chapter 2 and a riometer plot for Chapter 4.

Charles Rino, PhD (Rino Consulting, Menlo Park) is a consultant at Rino Consulting. He was a co-author on Chapter 3. Dr. Rino has provided help with development of SIGMA model.

Charles S. Carrano, PhD (Institute for Scientific Research (ISR), Boston College) is a Senior Research Physicist and Principal Investigator at ISR. He was a co-author on Chapter 3. Dr. Carrano has provided valuable inputs and also contributed to editorial comments for this chapter.

Daniel R. Weimer, PhD (ECE Department, Virginia Tech) is a Research Professor at Virginia Tech. He was a co-author on Chapter 6 and has provided ACE IMF data plot for the chapter.

Contents

List of Figures

List of Tables

Chapter 1

Introduction

The ionosphere is the ionized layer of the Earth's upper atmosphere ranging from about 50 km to 1000 km above the surface of the Earth. The ionosphere is divided into three major regions: D region is below 90 km, E region stretches from approximately 90 to 150 km and F region is above 150 km. The electron density appears to peak at around 120 km in E-region and at 350 km in F-region. Plasma instabilities and other magnetospheric sources may generate fluctuations in electron densities that are called "ionospheric irregularities". The irregularities may disturb a traversing radio signal leading to distortion of its phase and amplitude. These signal distortions, as observed from the ground, are known as ionospheric scintillations. *Wernik et al.* [2003] describe the relationship between ionospheric irregularities and scintillations in detail. Scintillations are frequently observed in high latitude and equatorial regions. *Aarons* [1982] mention that the occurrence of scintillations is also dependent on the phase of the solar cycle, the season, and the time of the day. Global Positioning System (GPS) signals can suffer fading, and GPS receivers may even lose lock on the signal due to ionospheric scintillations.

As will be described shortly, ionospheric irregularities have been studied extensively in low latitude regions. The high latitude irregularities on the other hand are dynamic and largely unexplored. The nearly worldwide availability of GPS signals, especially in high latitudes with recent development in dual frequency GPS receivers enables us to utilize scintillation-induced GPS signal variations in the study of high latitude irregularities. Furthermore, if these observations are coupled with modeling, it is possible to derive the physics of the irregularities and explore their generation mechanisms. With this background, I introduce my dissertation

topic as: "Investigation of High Latitude Ionospheric Irregularities utilizing Modeling and GPS Observations".

In Section 1.1, I describe the motivation to study the GPS scintillations at high latitudes. The research objectives of this work are specified in Section 1.2. The outline of this dissertation is presented in Section 1.3.

1.1 Motivation

Geomagnetic storms and substorms create disturbances in the ionosphere that adversely affect the accuracy of GPS [*Kintner et al.*, 2007]. Meticulous space weather forecasts are essential to avoid the effects of degraded performance of GPS in the sensitive navigation applications such as the aviation, where position accuracy is important. A better characterization of plasma irregularities in the ionosphere that are triggered by geomagnetic activity will assist in space weather forecasting.

As *Beach* [1998] and *Basu et al.* [2002] indicate, equatorial ionospheric irregularities display ordered motion, are field-aligned, and have been studied in detail for several years. The high latitude irregularities produce short-lived GPS scintillations, making them more challenging to characterize. Moreover, solar wind and magnetospheric plasmas are connected to the auroral regions of the ionosphere through complex magnetosphere-ionosphere coupling mechanisms. High latitude irregularities are, therefore, a result of different systems interacting with each other. Furthermore, study of scintillations observed on a GPS signal traversing through these irregularities involves the problem of electromagnetic (EM) wave propagation in random media. Modeling GPS scintillations from high latitude ionospheric irregularities can be considered as a 3 dimensional (3D) EM wave forward propagation problem. Additionally, the path of signal from satellite to ground has a variable angle of incidence. This delivers more challenges for the problem in addition to those created by inhomogeneity in the random media of irregularities

as well as by the geometry of magnetic field lines at high latitudes.

A lot of work has been done on equatorial irregularities. Also, abundant number of GPS scintillation monitoring receivers have been deployed in the near-equator regions to provide observations to support modeling [*Beach*, 1998; *Kintner et al.*, 2004; *Aveiro and Hysell*, 2010; *Béniguel and Hamel*, 2011]. But, polar and auroral irregularities remain largely unexplored because of lack of high latitude models and observations, especially in the Southern polar regions. With increasing accessibility, more GPS scintillation studies have been reported recently at high latitudes [*Mitchell et al.*, 2005; *Prikryl et al.*, 2011; *Kinrade et al.*, 2012]. Also, some work has been done in modeling the high-latitude scintillations [*Gherm et al.*, 2005a; *Maurits et al.*, 2008], though with the interest of characterizing the transionospheric path of propagation. The model developed as part of this Ph.D. Satellite-beacon Ionospheric-scintillation Global Model of the upper Atmosphere (SIGMA), on the other hand, focuses on generating time realizations of GPS signal observed on ground to assist the investigation of the physics of high latitude irregularities.

1.2 Research Objectives

The main objective of this study is to achieve a better understanding of the physics of small and medium scale ionospheric structures at high latitudes. This improved understanding of the characteristics can be used to investigate the large scale physics that created these irregularities (e.g. gradient drift, two stream instability, precipitation). At high latitudes, depending on the geophysical conditions, the source of irregularities may provide a window into the coupling between solar wind, magnetosphere and ionosphere.

In case of high latitude irregularity study, it is not straightforward to solve a problem by a forward method which is to first hypothesize the irregularity characteristics, design experiments to observe such an irregularity, and then conclude from those observations. If the predictions

from the theory do not match the observations within some error bar, then the hypothesis needs to be revised. Thus, we plan to use an inverse method which is to first observe an irregularity, estimate the physical characteristics of the irregularity and then conclude about the irregularity physics. This can be accomplished by using the GPS scintillation observations and observations from other ancillary instruments, and physical and propagation parameters derived with the help of a high latitude propagation model. The broad objectives of this work are:

1. Build scintillation data analysis tools for the new Connected Autonomous Space Environment Sensor (CASES) GPS receiver being deployed on the Antarctic Plateau as a part of the Autonomous Adaptive Low-Power Instrument Platforms (AAL-PIP) project.

2. Develop a full 3D propagation model to simulate GPS scintillations on ground at high latitudes.

3. Extract irregularity physics related to selected GPS scintillation observations from Northern and Southern polar regions by trying to solve an inverse problem with the help of the 3D model.

Each of these objectives is addressed as a separate journal paper presented as three chapters in this dissertation.

1.3 Dissertation Organization

The organization of this dissertation is as follows. Chapter 2 presents the work on post processing software developed to analyze data from the novel CASES GPS dual frequency receiver. CASES receivers were deployed to Antarctica as a part of the AAL-PIP project. We briefly introduce AAL-PIP experimental setup in this chapter. This project has been described in detail by *Clauer et al.* [2014] and is also discussed in Chapter 5. This part of the research was to develop the tools to analyze raw data from CASES and other GPS receivers. This

work was published in the Radio Science journal in 2012. The 3D EM wave propagation model, SIGMA, and its sensitivity study are described in Chapter 3. Using the analysis tools described in Chapter 2, the model SIGMA presented in Chapter 3, and an inverse modeling technique, a detailed interhemispheric study of high latitude irregularities was performed. The inverse modeling technique, and the findings from this investigation are presented in Chapter 4.

The description of the AAL-PIP project, excerpts from my Antarctica expedition in December 2010-January 2011 and the details of AAL-PIP remote operations are given in Chapter 5. An application of SIGMA inverse modeling is demonstrated in Chapter 6 along with a preliminary analysis of one of the recent substorm events recorded by the AAL-PIP instruments.

Chapter 7 offers concluding remarks and some recommendations for future work. Finally, the detailed simulation procedure of SIGMA, a derivation of the spatial phase at the bottom of the irregularity, and the daily downloading alert codes for AAL-PIP remote operations are presented in Appendices A, B and C.

Chapter 2

Initial GPS Scintillation results from CASES receiver at South Pole, Antarctica

K. B. Deshpande,[1] G. S. Bust,[2,6] C. R. Clauer,[1] H. Kim,[1] J. E. Macon,[1] T. E. Humphreys,[3] J. A. Bhatti,[3] S. B. Musko,[4] G. Crowley,[2] A. T. Weatherwax,[5].
Radio Science, 47, RS5009, doi:10.1029/2012RS005061, Published 31 October 2012.

[1] Bradley Department of Electrical and Computer Engineering, Virginia Tech, Blacksburg, Virginia, USA
[2]Atmospheric and Space Technology Research Associates, Boulder, Colorado, USA.
[3]Aerospace Engineering and Engineering Mechanics, The University of Texas at Austin, Austin, Texas, USA.
[4]Department of Atmospheric, Oceanic and Space Sciences, University of Michigan, Ann Arbor, Michigan, USA.
[5]Siena College, Department of Physics, Loudonville, NY, USA.
[6]Now at Johns Hopkins University Applied Physics Laboratory, Laurel, Maryland, USA.

Abstract

Connected Autonomous Space Environment Sensor (CASES) Global Positioning System (GPS) software-defined receivers developed for ionospheric scintillation studies have been deployed on Autonomous Adaptive Low-Power Instrument Platforms (AAL-PIP) at South Pole, Antarctica. In this paper, we describe the AAL-PIP experimental setup focusing on CASES. We explain in detail the method developed for analyzing CASES data, and report initial AAL-PIP CASES results. Furthermore, we compare the CASES measurements with those from a modified Novatel GSV4004 GPS Ionospheric Scintillations and TEC Monitor (GISTM) receiver at the South Pole. CASES receivers have been successfully deployed and reliably operated in

equatorial and mid-latitude regions. Four of these GPS receivers, for the first time, are deployed in high-latitude regions as a part of the National Science Foundation (NSF) funded project of deploying space science instrument platforms, AAL-PIPs, in Antarctica since December 2010-2011. We present initial scintillation results recorded by a CASES receiver at South Pole during the storm on 24 January 2012 along with AAL-PIP magnetometer observations. We have deduced that the CASES receiver scintillation observations agree with those from the Novatel GPS scintillation receiver. Since this is the first time a CASES receiver has been deployed to operate in a high latitude, low temperature, and low humidity environment, we consider this comparison a demonstration of its reliable operation as a science-grade scintillation receiver in such conditions. We plan to study high latitude ionospheric irregularities by using observations from CASES and other ancillary instruments from Antarctica coupled with physical parameters derived from models.

2.1 Introduction

Ionospheric irregularities caused by electron density fluctuations in the ionosphere disturb a traversing radio signal leading to distortion of its phase and amplitude. These signal distortions, as observed from the ground, are known as ionospheric scintillations. Detailed information on the relationship between ionospheric irregularities and scintillations can be found in the work of *Wernik et al.* [2003]. Scintillations are frequently observed in high latitude and equatorial regions. As summarized by *Aarons* [1982], the occurrence of scintillations is also dependent on the phase of the solar cycle, the season, and the time of the day. Global Positioning System (GPS) signals can suffer fading, and GPS receivers may even lose lock on the signal due to ionospheric scintillations. However, if these scintillation-induced GPS signal phase and amplitude variations are regarded as valuable scientific data instead of nuisance, then the nearly worldwide availability of GPS signals can be utilized for studies of scintillations at high latitudes. Considering the historic inaccessibility of these regions, such studies could prove extremely

useful.

Much prior research has exploited GPS as a tool for studying scintillations. *Akos et al.* [2001] and *Ganguly et al.* [2004] present different software-based approaches for implementing a GPS ionospheric monitoring receiver. Furthermore, *Skone et al.* [2005] offer test results for a GPS software receiver in simulated high-latitude scintillation conditions. As *Beach* [1998] and *Basu et al.* [2002] indicate, equatorial ionospheric irregularities display ordered motion, are field-aligned, and have been studied in detail for several years with an abundant number of GPS scintillation monitoring receivers deployed in the near-equator regions. *Basu et al.* [2002] imply that high latitude irregularities produce short-lived GPS scintillations, making the former more challenging to characterize. Moreover, solar wind and magnetospheric plasmas are connected to the auroral regions of the ionosphere through complex magnetosphere-ionosphere coupling mechanisms. High latitude irregularities are, therefore, a result of different systems interacting with each other. GPS scintillation measurements combined with physical parameters such as width, height, drift speed of the irregularities, and other values derived from modeling can be used to study the physical properties of ionospheric irregularities. *Coster et al.* [2005] reviewed characteristics of scintillations in the auroral and polar cap regions and their relationship with storm enhanced density (SED) by using GPS total electron content (TEC) mapping. Additionally, diffractive fading of GPS signals has been observed by *Smith et al.* [2008] in the auroral region as a consequence of E-region precipitation. High latitude GPS scintillations have been reported in the northern polar regions over a few years (*Skone and Knudsen* [2000]; *Mitchell et al.* [2005]; *Spogli et al.* [2009]; *Prikryl et al.* [2010]).

The southern high latitudes have been inaccessible for several years mostly due to the lack of infrastructure and the harsh environment in Antarctica. Advances in the cold weather operations in Antarctica as well as state-of-the-art power system technology have allowed the deployment of autonomous GPS scintillation receivers in remote regions. Some recent GPS scintillation studies by *Ngwira et al.* [2010]; *Prikryl et al.* [2011] and *Kinrade et al.* [2012] from

Antarctica display promise for the high latitude GPS studies from the southern polar and auroral regions.

In this paper, a geomagnetic storm on 24 January 2012 is studied as a means to evaluate the performance of a new, custom-designed, relatively inexpensive Connected Autonomous Space Environment Sensor (CASES) GPS scintillation monitoring receiver in Antarctica. This is the first time a CASES receiver has been used at high latitudes. In Section 2.2, we describe our experimental setup, including a description of the CASES instrument. A data analysis procedure developed for analyzing scintillation data from the CASES receiver is described in Section 2.3. Storm day results from the CASES receiver on System 4, one of the Autonomous Adaptive Low-Power Instrument Platforms (AAL-PIP), which is deployed at the South Pole for testing purposes for a year, are described in Section 2.4. In the same section, we validate our results by comparing them with scintillation data from a modified Novatel GSV4004 GPS Ionospheric Scintillations and TEC Monitor (GISTM) receiver deployed at the South Pole and maintained by the University of Bath, UK and the British Antarctic Survey (BAS).

2.2 Experimental Setup

As a part of collaborative efforts to understand the space environment of the Earth and its global dynamical response to external and internal influences, a Polar Experiment Network for Geospace Upper-atmosphere Investigations (PENGUIn) team has been established. The PENGUIn AAL-PIP project under National Science Foundation (NSF) support calls for deployment of a chain of six AAL-PIPs, four of which support fluxgate and induction magnetometers as well as dual frequency CASES GPS receivers. The other two stations are of an earlier design and support only fluxgate magnetometers.

The array of AAL-PIP Antarctic stations will boast a handful of cutting-edge technological advances designed to optimize data collection and power management for year-round sustained

operation. As described by *Musko et al.* [2009], a major focus of the original system development was to build a low-power platform with a single fluxgate magnetometer specifically designed to operate autonomously in remote Antarctic regions. The platform has now been upgraded to support three instruments: a fluxgate magnetometer, a search coil magnetometer, and CASES. The upgraded platforms are capable of unattended operation for at least three years at temperatures as low as $-80°$ Celsius and near real-time data retrieval via satellite communications.

An AAL-PIP utilizes solar energy and stores power in sealed lead-acid batteries for winter operation. The AAL-PIP power system consists of six 40 W solar panels and 16 lead-acid batteries. A super-insulated electronics box supports power control, communication electronics, and data management for all three instruments. The temperature inside the electronics box is maintained at $-28°$ Celsius throughout the winter.

CASES, originally developed to be paperback-novel sized, was customized to a cubic form factor (10 cm×10 cm×10 cm) to fit inside the compact electronics box of AAL-PIP. Furthermore, during the development, the receiver passed the cold soak test below $-50°$ Celsius and demonstrated reliable operation at about $-40°$ Celsius before and after the test. CASES receivers on the AAL-PIP systems are connected to Antcom GPS antennas.

The CASES receiver is a scientific grade, low-cost, dual-frequency GPS receiver developed by Cornell, UT Austin, and Atmospheric & Space Technology Research Associates (ASTRA). *Crowley et al.* [2011] and *O'Hanlon et al.* [2011] describe the development of CASES, its specifications, characteristics, and operation in detail. All the data acquisition and tracking operations as well as science and navigation related operations, such as TEC computations, scintillation monitoring, and calculation of navigation solution and GPS observables, are performed on a general purpose digital signal processor (DSP). Based on real-time data processing by a scintillation monitor called "SCINTMON," the DSP outputs low-rate scintillation data at up to 10 Hz and high-rate data at up to 100 Hz. The data are then routed to a single board computer that

runs a server program for data logging and remote monitoring. As an ionospheric scintillation monitor, CASES has many advantages as described by *Crowley et al.* [2011], including GPS L2 civil code (L2C) tracking capability, incorporation of specialized tracking loops designed for operation in both weak-signal and scintillating environments, and connectivity via a number of different options. CASES on AAL-PIPs may be accessed through an Iridium link for remote logging, reconfiguration and reprogramming.

CASES employs a temperature-compensated crystal-oscillator (TCXO) as its reference oscillator. As *Van Dierendonck et al.* [1993] point out, phase variations caused by instability manifest a significant spectral overlap with those induced by ionospheric scintillation. It is imperative, therefore, to isolate and remove these clock effects to avoid false detection of phase scintillation. As suggested by *Van Dierendonck et al.* [1993], receiver clock errors can be removed by subtracting a non-scintillating "reference" channel from a scintillating channel. In the unlikely scenario that all channels are scintillating, the reference channel is chosen to be one of two channels with the lowest scintillation power ratio, a metric defined in the work of *O'Hanlon et al.* [2011]. Once these clock effects are removed, SCINTMON operates on the clock-free phase time history and complex accumulations to estimate scintillation of interest.

At high latitudes, phase scintillations are observed more often than amplitude scintillations. A study on the distribution and dynamics of irregularities in the dayside auroral region by *Basu et al.* [1998] indicated large-scale phase variations without the presence of amplitude scintillations. More recent observations reported by *Mitchell et al.* [2005] in northern high latitudes and *Kinrade et al.* [2012] in southern high latitudes also showed a predominance of phase scintillations. To ensure triggering sensitivity to both phase and amplitude scintillations, CASES implements a novel triggering strategy, whose detection statistic is based on the power spectrum of complex (in-phase and quadrature) accumulations. The triggering strategy, first described by *O'Hanlon et al.* [2011], has been shown to be a reliable indicator of scintillation when tested on historical scintillation data from both low and high latitude regions.

CASES implements data capture and retrieval as follows. To prevent loss of interesting scintillation data, CASES temporarily collects high-rate data on a variable-length circular buffer (a 120-second buffer was used to obtain the empirical results reported in this paper). SCINTMON processes these data in real-time in batch intervals (typically 100 seconds) and implements the scintillation triggering algorithm. A trigger indicates the presence of a phase or amplitude fluctuation more vigorous than the user-specified triggering threshold. In response to a triggering event, CASES outputs the contents of the circular buffer, thereby ensuring that a complete picture of the scintillation event is captured, including the quiet prelude before the onset of scintillation. High-rate data are recorded typically at 50 Hz as raw complex accumulations and beat carrier phase. As mentioned earlier, the communication with each remote AAL-PIP is provided by an Iridium link. With a daily upload-download limit of 16 MB, data collected by all three space science instruments on board, namely, the fluxgate magnetometer, the search coil magnetometer and the CASES GPS receiver, need to be constrained. Each of the magnetometers collects about 1 MB of data per day. Thus, in normal daily operation, CASES collects low-rate data and triggered high-rate data until the daily memory limit for GPS data collection of about 12 to 13 MB is reached. Its scintillation triggering strategy enables CASES to make maximal use of its allotted daily data limit by capturing and passing along high-rate data only spanning the most vigorous scintillation events. Moreover, a special AAL-PIP "storm mode" can be enabled in anticipation of an incoming solar storm. In storm mode, CASES is allowed to store much more than the standard daily data limit. Data stored locally in storm mode are retrieved over a period of several days post-storm. Data presented in this paper were collected in storm mode.

2.3 Data Processing

In scintillation studies, two scintillation parameters, viz., scintillation index $S4$ and standard deviation of detrended phase σ_ϕ, are commonly used to indicate the occurrence of am-

plitude and phase scintillations, respectively. These parameters are computed from detrended high-rate power and phase data. Analysis of single-frequency GPS data for ionospheric scintillation studies requires removing low frequency systematic effects such as those from the troposphere, satellite geometry, and the receiver oscillator. Post-processing involved in the analysis of CASES single frequency high-rate data is elaborated in this section.

As described in Section 2.2, CASES continuously collects low-rate processed data, but only collects high-rate carrier phase and IQ data (typically at 50 Hz) when the scintillation trigger detects an interesting event. The receiver outputs low-rate and high-rate data in the form of binary files that can be converted into ASCII text files called *scint.log* and *iq.log*, respectively. As mentioned earlier, the receiver clock errors introduced into the phase data by the CASES TCXO may generate phase fluctuations that appear similar to phase scintillations. These errors can be eliminated by a simple operation of subtracting carrier and IQ phase of a non-scintillating reference channel from those of a possibly scintillating channel. The IQ phase is defined in terms of the in-phase and quadrature phase components as $\arctan(Q/I)$. In this description, a continuous stream of data from a single GPS satellite identified by its pseudo random noise (PRN) number is referred to as a channel. We have adapted a simple method of reading and processing high-rate data for the clock error removal. For each PRN, we accumulate the available high-rate data from the *iq.log* file and determine the reference channels from the *scint.log* file at times corresponding to these data. Following this examination, we construct data segments of continuous carrier phase of scintillating PRNs at times coinciding with those of the high-rate carrier phase for reference PRNs. We subsequently subtract the reference PRN phase data from the scintillating PRN phase data to obtain differenced carrier phase, free of receiver clock error.

Elimination of clock error is followed by removal of satellite geometry effects. We use a method of polynomial fit subtraction on the continuous segments of data to remove most of the satellite geometry effects, followed by a high-pass filtering operation to ensure that we extract

fluctuations on a scale of 10 seconds or less. A third-order polynomial fit to the differenced carrier phase over a continuous interval of time can be subtracted from the differenced carrier phase to remove the satellite geometry effects. More details on the procedure of removing receiver clock effects and satellite geometry effects from the CASES carrier phase are discussed by *O'Hanlon et al.* [2011].

For our scintillation studies, we are interested in high-frequency variations introduced by scintillations. Therefore, a differenced IQ phase is added to the differenced carrier phase to obtain phase which contains frequency components up to the pre-detection bandwidth of 50 Hz. This differenced phase then undergoes polynomial fit subtraction. To obtain the final detrended phase, any residual low frequency variations are subsequently removed from the phase by using a high-pass sixth-order Butterworth filter in the frequency domain as indicated by *Van Dierendonck and Hua* [2001]. We generally use a 3-dB cut-off frequency of 0.1 Hz for the filter. In the case of data segments shorter than 60 seconds, we use a cut off frequency of 0.2 Hz. In Figure 2.1, we demonstrate the effectiveness of the high-pass filter to extract high frequency phase. Ionospheric scintillation data detrending is discussed in detail by *Forte and Radicella* [2002].

The data analysis procedure to detrend the high-rate phase data can be summarized symbolically as follows. If $\phi_{c_s}(t)$ and $\phi_{c_{ref}}(t)$ are the time series of the carrier phase on scintillating and reference channels, respectively, we obtain differenced carrier phase time series $\phi_c(t)$ as

$$\phi_c(t) = \phi_{c_s}(t) - \phi_{c_{ref}}(t). \tag{2.1}$$

Similarly, differenced IQ phase time series $\phi_{iq}(t)$ is obtained by subtracting the IQ phase on the reference channel ($\phi_{iq_{ref}}(t)$) from the IQ phase on the scintillating channel ($\phi_{iq_s}(t)$):

$$\phi_{iq}(t) = \phi_{iq_s}(t) - \phi_{iq_{ref}}(t). \tag{2.2}$$

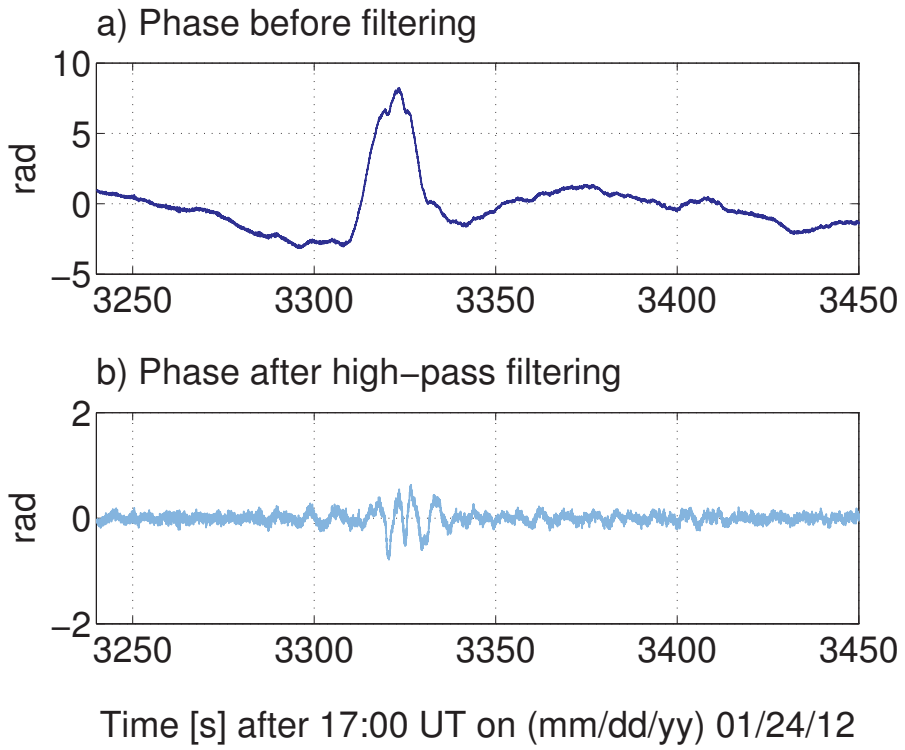

Figure 2.1: Phase of PRN 9 signal on 24 January 2012, System 4. Plot (a) shows the phase after polynomial fit-subtraction, and plot (b) shows the phase after high-pass filtering using a Butterworth filter implemented in the frequency domain.

The differenced carrier and IQ phases are added together to obtain the phase $\phi(t)$ which contains frequency components up to the pre-detection bandwidth:

$$\phi(t) = \phi_c(t) + \phi_{iq}(t). \tag{2.3}$$

A third-order polynomial fit $\widetilde{\phi}(t)$ of the phase $\phi(t)$ is subtracted from itself to obtain phase $\phi'(t)$ with predominantly high frequency components:

$$\phi'(t) = \phi(t) - \widetilde{\phi}(t). \tag{2.4}$$

A high-pass filtering of phase $\phi'(t)$ removes any residual low-frequency components and produces the final filtered phase $\phi_f(t)$. This data processing procedure used to obtain the

detrended high-rate CASES phase is summarized in Figure 2.2.

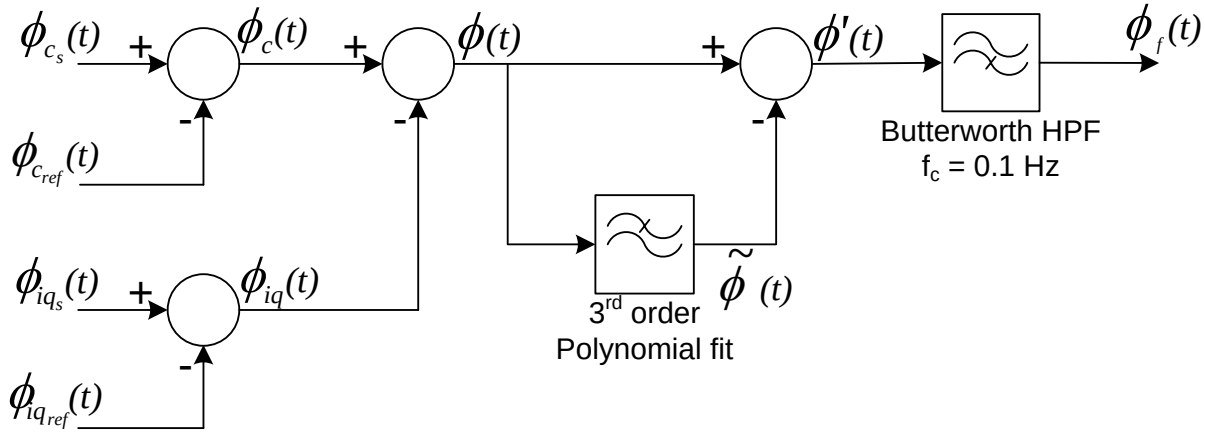

Figure 2.2: A block diagram summarizing the data processing procedure used to obtain the detrended phase data from the CASES receiver. HPF stands for high-pass filter.

To detrend the high-rate power time history, we follow the procedure described by *Van Dierendonck and Hua* [2001], where the raw power data $(I^2 + Q^2)$ are high-pass filtered with a sixth-order Butterworth filter. Note that receiver clock variations do not significantly affect signal power; thus, signal differencing to remove clock errors is not required for power data. However, it should be mentioned that the detrending of power is carried out on continuous segments with times corresponding to those of the processed phase data segments. To detrend power, high-pass filtering is performed by initially generating a sixth-order low-pass Butterworth filter with a typical 0.1 Hz cut-off, applying this filter to the power of a scintillating PRN to obtain a low-pass-filtered output, and finally dividing the original power of that PRN by the low-pass-filtered power. Therefore, if $P_r(t)$ is the data segment with a time series of the raw power, and $P_{LPF}(t)$ is the time series obtained by low-pass filtering $P_r(t)$, the high-pass filtered power $P_f(t)$ is given as

$$P_f(t) = \frac{P_r(t)}{P_{LPF}(t)}. \tag{2.5}$$

The 0.1 Hz cut-off is flexible and can be adjusted to ensure that all low-frequency effects are removed from the data. If the continuous data segments are smaller than 60 seconds, we use a cut-off frequency of 0.2 Hz instead of 0.1 Hz, as with the phase filtering operation. The

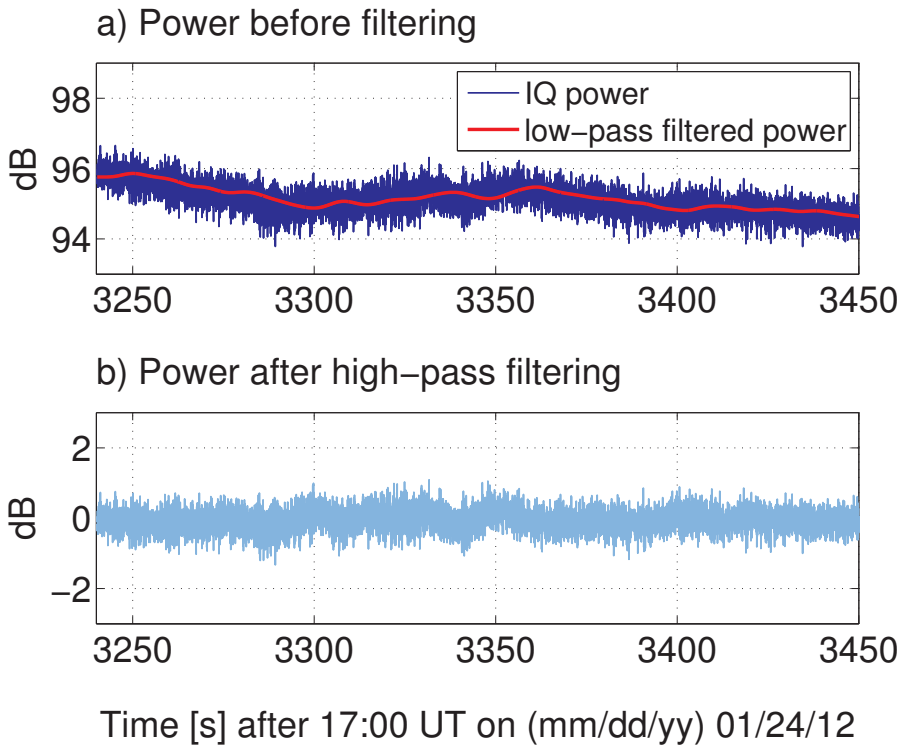

Figure 2.3: Power of PRN 9 signal on 24 January 2012, System 4, (a) before and (b) after high-pass filtering. High-pass filtered signal (plot (b)) is obtained by dividing the IQ "raw" power (blue graph in plot (a)) by low-pass filtered power (red graph in plot (a)).

effectiveness of high-pass filtering on power, i.e. dividing out the low-pass filtered power, is seen in Figure 2.3.

The scintillation index $S4$ is typically derived from detrended signal intensity SI which is in turn obtained by taking the square root of detrended power. $S4$ is defined as follows:

$$S4 = \sqrt{\frac{\langle SI^2 \rangle - \langle SI \rangle^2}{\langle SI \rangle^2}}, \tag{2.6}$$

where the angular bracket represents a time average, commonly taken over a 60-second interval. The standard deviation of the phase σ_ϕ is computed over the same interval. For CASES power and phase data segments longer than 60 seconds, we use a 1 minute-long sliding window for both $S4$ and σ_ϕ computations. CASES low-rate data consists of $S4$ and σ_ϕ precomputed by SCINTMON, which can be used with the high-rate scintillation parameters to determine the

scintillating time periods as illustrated in the next section.

2.4 CASES Results and Comparison with Data from the Novatel Receiver

The CASES measurements reported here were recorded from AAL-PIP System 4 (89.998°S, 124.075°E) on 24 January 2012. About 17 hours of low-rate and about 9 hours of high-rate data were collected during the CASES storm mode within the period of 24 January to 26 January 2012. The GPS receiver was switched to storm mode a little after 17:00 UT on 24 January 2012. This was to capture any interesting scintillating events possibly originated by a CME reaching the Earth from an M9-class solar flare that erupted on 23 January around 03:59 UT from sunspot 1402. The CASES receiver recorded low-rate data on 2 frequencies during these measurements, namely, GPS L1 legacy civil code (L1CA) and GPS L2 civil L code (L2CL). Useful high-rate data were detected on L1CA. Concern over high temperatures in the insulated AAL-PIP electronics enclosure limited CASES operation to a 50% duty cycle in 1-hour increments. It is expected that this limitation will be eliminated in the future as the AAL-PIP electronics prove their ability to operate at high temperatures.

Stack plots of low-rate standard deviation of phase σ_ϕ for each available PRN as recorded on 24 January 2012 by System 4 CASES on the L1CA signal are shown in Figure 2.4. For each PRN, σ_ϕ is normalized using the maximum detected value of σ_ϕ in all the available low-rate data on that day. The horizontal axis on the plot represents time in UT, while the vertical axis displays the PRN of the available satellite. The vertical scale on the right hand side of the plot corresponds to the maximum value of phase standard deviation in the stack plot, which might occur on any of the PRNs (for this case, it is PRN 9). The stack plots reveal some interesting possible phase scintillation events, for example, on PRN 9 and PRN 12. Figure 2.4 can be considered as a daily summary plot as it depicts the availability of different satellites with recorded low-rate data. During the four hours of ON time on January 24, the receiver collected

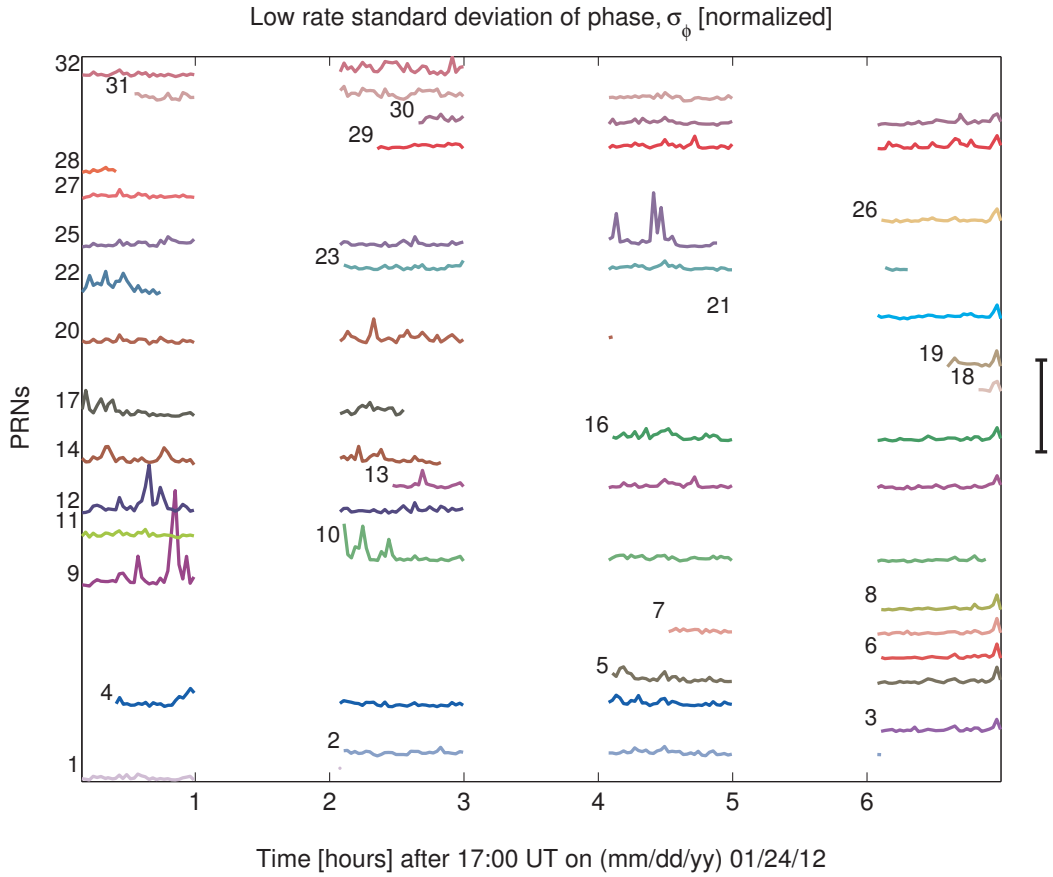

Figure 2.4: Stack plots from System 4 of low-rate σ_ϕ for all available PRNs. This figure shows GPS satellite availability with respect to time in UT on 24 January 2012.

about 37 MB of low-rate and raw high-rate data. The high-rate data were then analyzed using the post-processing technique described in Section 2.3. We have generated stack plot similar to Figure 2.4 with high-rate standard deviation of phase. This plot indicated the availability of different satellites with recorded high-rate data. Because of the facility of selecting and storing interesting events, the high-rate data availability covered much less total time than the low-rate data.

The two events considered for study in this paper are observed using the signals from PRN 9 and PRN 12 on L1CA frequency after 17:30 UT on 24 January 2012. These events are clearly visible in Figure 2.4. The processed high-rate data for these events showed strong phase scintillations for a duration of about 60 seconds. The scintillations were found to have

a dominant period of 6 seconds. The Novatel receiver used for comparison was about 1.5 kilometers away from the CASES GPS receiver. With such a short baseline, the scintillation data from the two receivers should be strongly correlated. In order to compare the two events with the Novatel data, the power and phase obtained from the Novatel receiver at South Pole were processed with the same techniques used for CASES. Specifically, the power was divided by the low-pass filtered power, and for the phase, a polynomial fit was subtracted followed by a high-pass Butterworth filtering operation in the frequency domain. The Novatel receiver uses an oven-controlled SC-cut crystal oscillator (OCXO), which is stable enough that clock variations do not significantly corrupt phase measurements, as discussed by *Van Dierendonck and Hua* [2001]. Therefore, no differencing operation was required for phase from the Novatel receiver.

A comparison between detrended phase obtained from the CASES and Novatel receivers for the 2 PRNs is shown in Figure 2.5. It is evident from the plot that CASES reproduces phase as obtained from the Novatel receiver. The detrended power for the CASES and Novatel receivers also agree closely, but the power variation was observed to be less than 1 dB, indicating that these events are predominantly phase scintillations. A careful examination of phases in a shorter time duration, as shown in Figure 2.6, revealed that the CASES phase for PRN 9 leads the Novatel phase by 0.12 seconds. Scintillations on PRN 12 indicated that the Novatel phase leads the CASES phase by 0.12 seconds. The close agreement between the two receivers implies little to no horizontal motion of the irregularities causing scintillation.

For the case of this 24 January 2012 study, a thorough comparison of the available CASES data with Novatel data showed that apart from the two scintillation events from Figure 2.5, all the events in CASES were confirmed detections. However, a few weak scintillation events from the Novatel receiver were not detected by the CASES receiver, presumably because they were not sufficiently strong to trigger CASES high-rate data output for the triggering threshold that was implemented at the time. To obtain good statistics of CASES performance at high latitudes, a large amount of additional data needs to be collected to ensure statistical significance. We

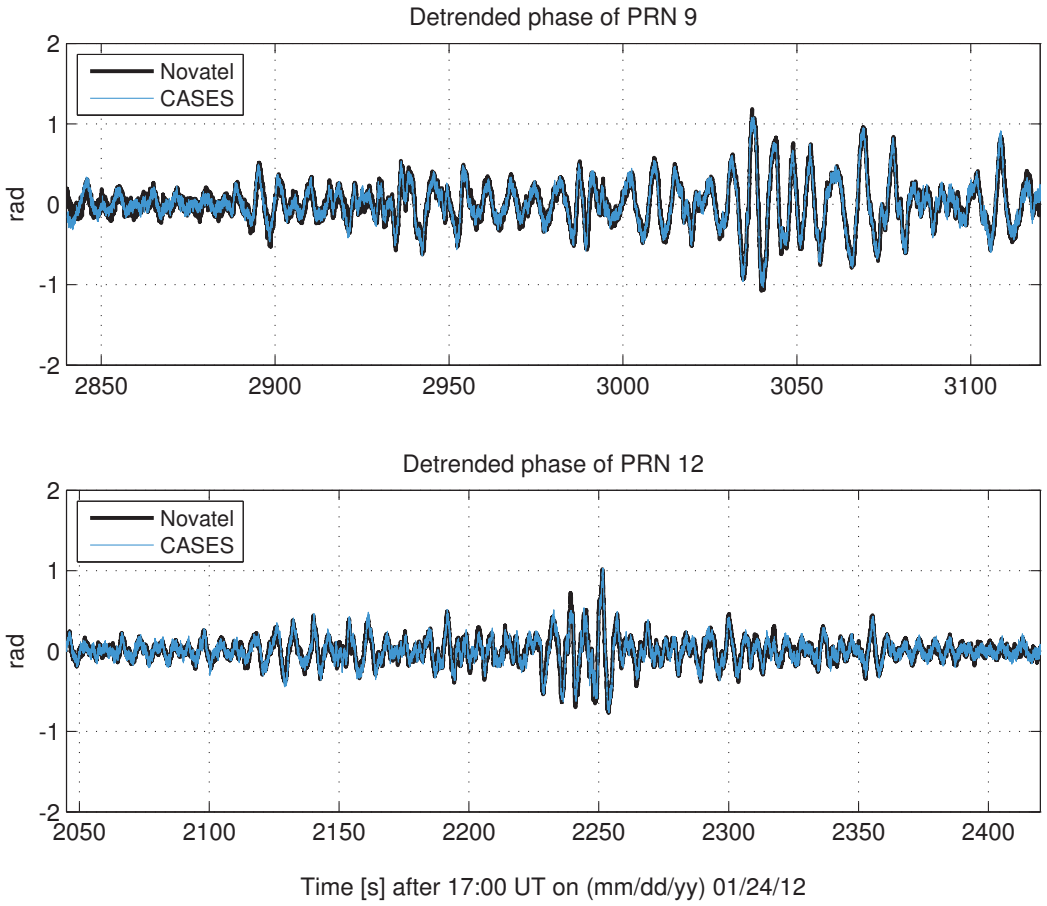

Figure 2.5: Plots comparing Novatel and System 4 CASES phase data on 24 January 2012 for PRN 9 and PRN 12.

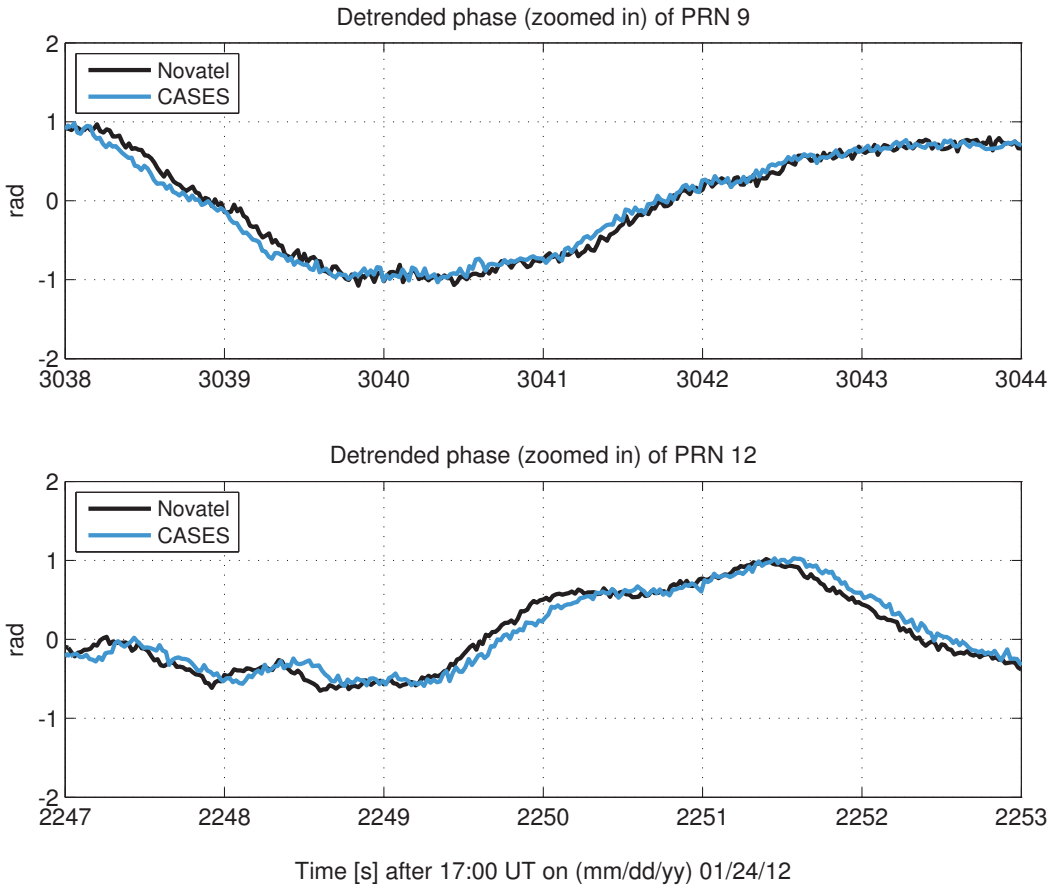

Figure 2.6: Plots after zooming in on Figure 2.5 showing the time delay between the Novatel and System 4 CASES phase data on 24 January 2012 for PRN 9 and PRN 12.

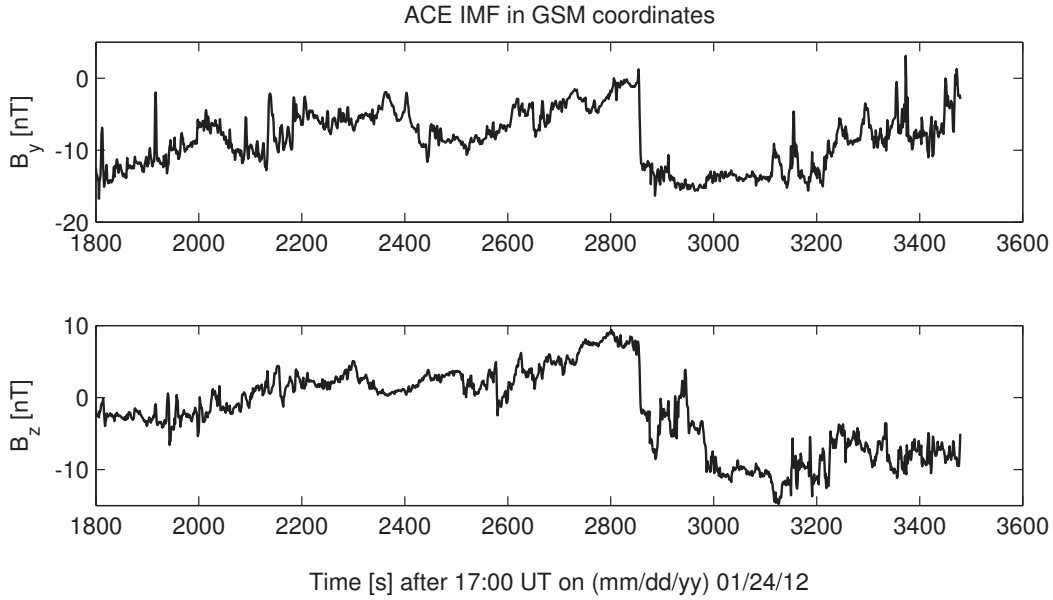

Figure 2.7: ACE IMF B_y and B_z components with 1 Hz sampling frequency at the ACE satellite position in geocentric solar magnetospheric (GSM) coordinates on 24 January 2012 from 17:30 UT to 18:00 UT.

are experimenting with different storm mode strategies and different threshold values for the AAL-PIP CASES to permit collection of large data sets useful for statistical study.

The interplanetary magnetic field (IMF) observations obtained from the Advanced Composition Explorer (ACE) spacecraft are plotted in Figure 2.7 from 17:30 UT to 18:00 UT. ACE is located close to the L1 Lagrange point, a position between the Sun and the Earth about 1.5 million km from the Earth. The solar wind data recorded during this time was 285 km/s. This implies that, at this time, the solar wind observed at ACE took about 88 minutes to arrive at the Earth. The magnetic field components in Figure 2.7 are in geocentric solar magnetospheric (GSM) coordinate system. Both B_y and B_z displayed sharp changes ∼3000 seconds after 17:00 UT, with B_y going from ~ 0 nT to -15 nT and B_z going from $\sim +10$ nT to -10 nT. These changes in B_y and B_z appear to occur at approximately the same time as the GPS phase fluctuations shown in the bottommost panel in Figure 2.8.

Furthermore, we compared the CASES phase fluctuations with observations from the AAL-PIP fluxgate and search coil magnetometers for the same time period. Our preliminary compar-

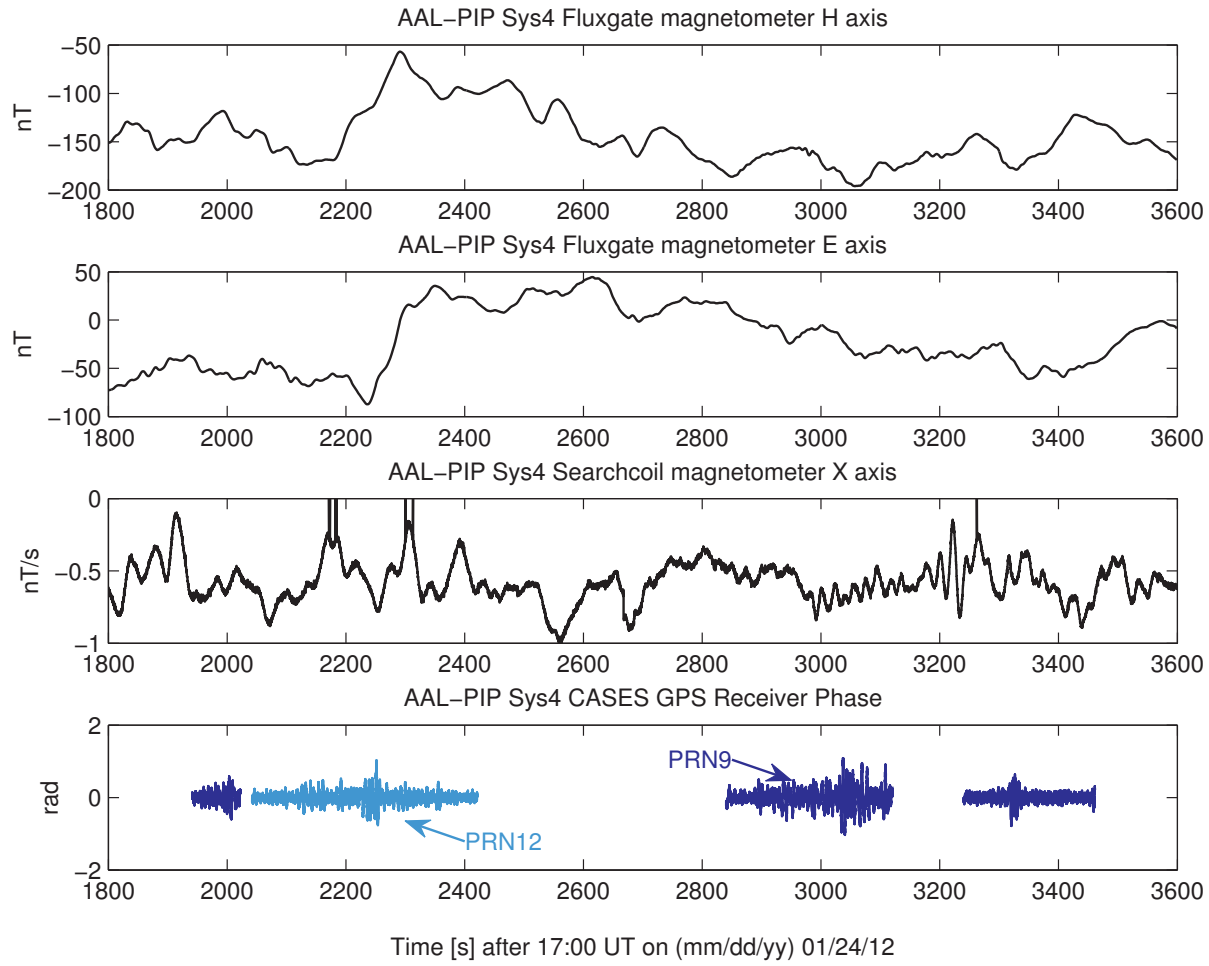

Figure 2.8: System 4 CASES GPS receiver phase for PRN 9 and PRN 12 plotted with observations from System 4 AAL-PIP magnetometers on 24 January 2012.

ison of the CASES GPS phase with observations from AAL-PIP magnetometers on System 4 is illustrated in Figure 2.8. The coordinate system for fluxgate magnetometer conforms to H(geomagnetic north), E(geomagnetic east) and Z(vertically down toward the center of the Earth) system. The coordinate system for search coil magnetometer is X(geomagnetic south), Y(geomagnetic west) and Z(along the field line). A cursory inspection of the plots suggests that the GPS scintillation events may be causally connected to the magnetometer observations. Comparing the plots, it appears that the GPS phase fluctuations from PRN 12 starting approximately at 2200 seconds after 17:00 UT are correlated with significant deflections in the fluxgate H and E axes, while the fluctuations on PRN 9 at ∼3100 seconds after 17:00 UT seem to be correlated with wave-like variations in the search coil X axis. The possible correlations between the observed GPS phase scintillations and the changes in IMF, the deflections in the fluxgate H and E axes, and the wave-like variation in the search coil X axis, will be investigated in detail in a later paper.

2.5 Summary and Conclusions

Initial results from a CASES GPS receiver deployed at high latitudes have been presented. Our experiment of deploying to the Eastern Antarctic Plateau autonomous space science platforms, AAL-PIPs, equipped with the novel CASES GPS receiver, has also been discussed. For testing purposes, three AAL-PIP systems with CASES receivers have been established at the South Pole. As part of our study, we have developed and applied specialized post-processing techniques to analyze CASES high-rate data. Results of GPS phase scintillations observed during the solar storm of 24 January 2012 have been reported. We have compared the CASES high-rate IQ data with data from a Novatel GSV4004 GPS scintillation receiver at the South Pole, and we have determined that there is a good match in phase scintillations between the two. From this study, it is clear that CASES can be reliably used as a science grade GPS scintillation detection monitor to record phase scintillations at high latitudes.

For further study, scintillation events such as those from the 24 January 2012 storm can be inspected in detail using ancillary observations from other AAL-PIP instruments. Specifically, the fluxgate and search coil magnetometers suggest a connection between GPS scintillations and IMF and magnetometer observations. A detailed study examining observations from these instruments and a forward propagation model should prove useful to understanding the physics of high latitude ionospheric irregularities. Utilizing all available AAL-PIP CASES receivers at the South Pole along with the Novatel receiver for correlation scintillation studies should also be explored.

When the AAL-PIP stations are deployed to their final destinations along the 40° magnetic meridian and are each separated by a couple hundred kilometers from the nearest adjacent station, AAL-PIP CASES scintillation results may yield information about possibly drifting irregularities. This will facilitate comparison of occurrence of scintillations in the auroral, polar cap, and cusp regions. We will then be able to compare these observations with those from GPS receivers in the northern high latitudes to investigate whether simultaneous scintillations occur in the conjugate auroral regions.

Acknowledgments

We would like to thank the National Science Foundation for supporting this research under grants ANT-0839858, ATM-922979 and ANT-0840650. We are grateful to Dr. Cathryn Mitchell and Joe Kinrade of University of Bath, UK for sharing the South Pole Novatel GPS data with us.

Chapter 3

Satellite-beacon Ionospheric-scintillation Global Model of the upper Atmosphere (SIGMA) I: High latitude sensitivity study of the model parameters

K. B. Deshpande,[1] G. S. Bust,[2] C. R. Clauer,[1] C. L. Rino[3], C. S. Carrano[4]
Journal of Geophysical Research (Space Physics), 119, 4026-4043, doi: 10.1002/2013JA019699, published online: 27 May 2014.

[1] Bradley Department of Electrical and Computer Engineering, Virginia Tech, Blacksburg, Virginia, USA
[2]The Johns Hopkins University Applied Physics Laboratory, Laurel, Maryland, USA.
[3]Rino Consulting, Menlo Park, California, USA.
[4]Boston College, Chestnut Hill, Massachusetts, USA.

Abstract

Complex magnetosphere-ionosphere coupling mechanisms result in high latitude irregularities that are difficult to characterize using only Global Navigation Satellite System (GNSS) scintillation measurements. However, GNSS observations combined with physical parameters derived from modeling can be used to study the physics of these irregularities. We have developed a full three dimensional (3D) electromagnetic (EM) wave propagation model called "Satellite-beacon Ionospheric-scintillation Global Model of the upper Atmosphere" (SIGMA), to simulate GNSS scintillations. This model eliminates the most significant approximation

made by the previous simulation approaches about the correlation length of the irregularity. Thus, for the first time, using SIGMA we can accomplish scintillation simulations of significantly high fidelity. While the model is global, it is particularly applicable at high latitudes as it accounts for the complicated geometry of the magnetic field lines in these regions. Using SIGMA we simulate the spatial and temporal variations in the GNSS signal phase and amplitude on the ground. In this paper, we present the model and results from a study to determine the sensitivity of the SIGMA outputs to different input parameters. We have deduced from our sensitivity study that the peak to peak (P2P) power gets most affected by the spectral index and line of sight (LOS) direction, while the P2P phase and standard deviation of the phase (σ_ϕ) are more sensitive to the anisotropy of the irregularity. The sensitivity study of SIGMA narrows the parametric space to investigate when comparing the modeled results to the observations.

3.1 Introduction and Motivation

Ionospheric scintillations are rapid variations in the amplitude and phase of the radio signals resulting from the electron density irregularities in the ionosphere. Such rapid variations in the radio signals can have deleterious effects on the societal systems. For example, ionospheric irregularities can affect Global Navigation Satellite Systems (GNSS) and produce scintillations that may cause distortion in the signal's phase and amplitude. As summarized by *Aarons* [1982], the scintillations are frequently observed in the high latitude and equatorial regions.

The study of ionospheric scintillations involves the problem of electromagnetic (EM) wave propagation in random media. An extensive discussion of scintillation theories such as the Phase Screen theory, Rytov solution, Parabolic Equation Method (PEM) and Fresnel-Kirchhoff diffraction formulation can be found in the work of *Yeh and Liu* [1982]. *Costa and Basu* [2002] describe slant propagation of a plane wave through a bi-dimensional irregularity layer using the Huygens-Fresnel convolution integral. *Fremouw and Secan* [1984], *Secan et al.* [1995] and *Secan et al.* [1997] present Wideband ionospheric scintillation model (WBMOD) and its high

latitude upgrade SCINTMOD. These employ a phase screen model introduced by *Rino* [1979] in which the irregularity or a phase screen is characterized by a power-law electron density spectrum. *Knepp* [1983] and *Knepp and Nickisch* [2009] discuss the multiple phase screen (MPS) simulation that solves for transionospheric propagation involving a number of layers of ionization, and directly computes a realization of the signal received on ground. Each of these layers is characterized by a spatially varying electron density power spectrum. *Béniguel* [2002] introduce a Global Ionospheric Scintillation propagation Model (GISM) based on the MPS technique. *Béniguel and Hamel* [2011] implemented this model for equatorial regions showing a good agreement of the model with measurements. *Humphreys et al.* [2010] present an equatorial scintillations model for improving the scintillation performance of phase tracking loops. *Grimault* [1998] demonstrate a numerical technique also based on MPS, modified to be applicable for cases when the EM wave source is close to the turbulent medium and the receiver is far away. A propagation model by *Gherm et al.* [2000] and *Gherm et al.* [2005a] for scintillations on transionospheric links makes use of the extended Rytov approximation. Based on their work, *Maurits et al.* [2008] modeled the scintillation effects on high-latitude transionospheric paths.

Modeling the random EM wave propagation through ionospheric irregularities at high-latitudes has a different set of complications and issues from modeling in the equatorial regions. At high latitudes, the magnetic field is nearly vertical, and the irregularities that extend along the magnetic field over large distances have to be treated carefully. In particular, an approximation often made for the equatorial or statistically-based models is that the thickness of the irregularity layer being integrated through is much larger than the scale of the irregularities. While this is true at the equatorial latitudes, where the magnetic field is horizontal and the integration is through the vertically extended regions, it is not true at the high latitude regions. Another issue at high latitudes, particularly for modeling Global Positioning System (GPS) signals, is that the maximum elevation angle to the GPS satellites gets smaller as you go to higher latitudes ($\sim$ 46 degrees at the geographic pole). This poses a numerical issue since

for thick layers and smaller elevation angles, the signal can cut through several hundreds of kilometers horizontally. A third issue is the arbitrary geometry, when considering three coordinate systems: the satellite-receiver line-of-sight (LOS) system, the irregularity layer (the geographic or geomagnetic) coordinate system and the magnetic field coordinate system. For such complex geometries, no simplifying approximations can be made and the high-latitude scintillation problem must be treated as a full 3-dimensional (3D) EM wave propagation problem. To address these issues we have developed a new 3D EM random-media propagation model: "Satellite-beacon Ionospheric-scintillation Global Model of the upper Atmosphere" (SIGMA). While SIGMA has been developed to be applicable over the entire globe, and for all transionospheric frequencies (low VHF and above), it has been specifically developed to handle the particular complications of the high-latitude scintillation problem. Inside SIGMA we propagate a signal from a moving satellite to the ground through multiple phase screens as illustrated in Figure 3.1. We first obtain a spatial electron number density distribution from a spectral model for high latitude irregularities, and then utilize a hybrid method that combines the MPS technique with a split-step solution to the forward propagation equation (FPE) [*Rino*, 2010; *Rino and Carrano*, 2011]. As mentioned by *Rino and Carrano* [2011], FPE is the most general way to solve a scintillation problem as it encompasses refraction, diffraction and the effects of small scale structure. The split-step method has been used recently by *Ghafoori* [2012] to achieve a physics-based scintillation simulations, but at equatorial latitudes.

Radio propagation measurements are sensitive to the small and intermediate-scale structures, structure transport and total electron content (TEC). Although TEC measurements are more abundantly available than scintillation measurements, they cannot resolve the small and intermediate-scale structures. GNSS scintillation measurements alone are insufficient to extract information about these structures. SIGMA can give us a capability to infer the physics of these structure from the scintillation measurements.

Our ultimate goal is to try to have better understanding of the physics of the small and

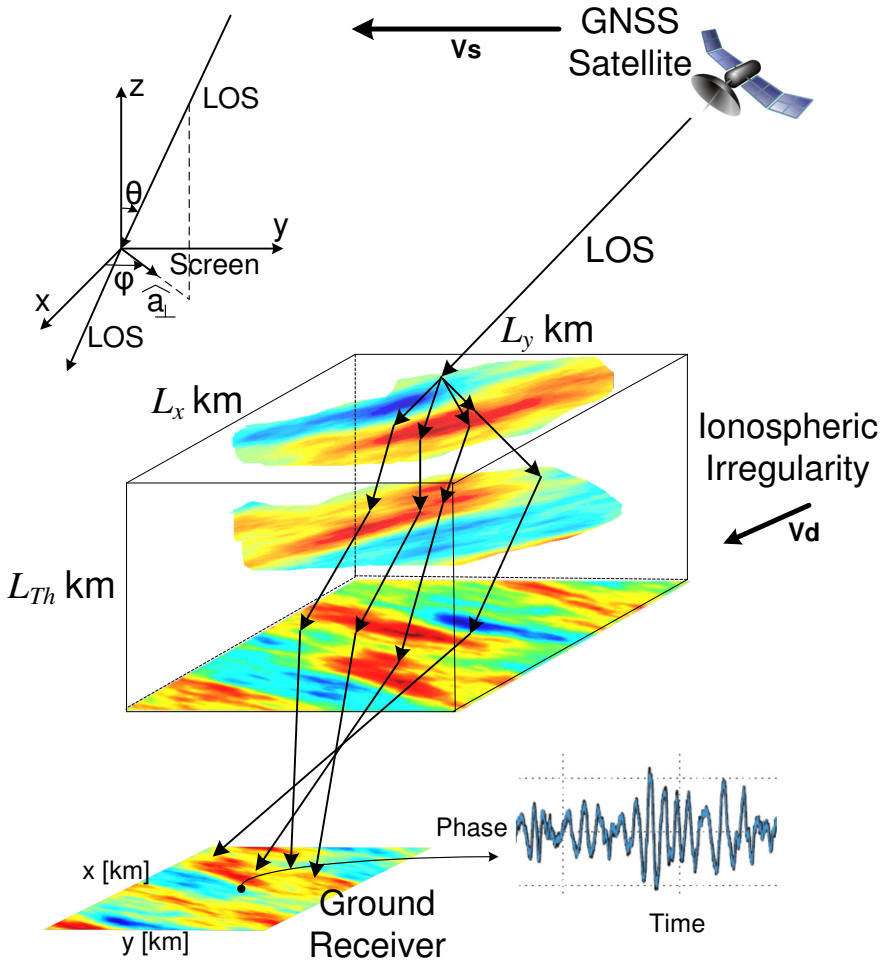

Figure 3.1: An illustration showing the components covered by SIGMA. The figure is not to scale. Although, only 3 phase screens are shown in the illustration, the number of screens can be changed in the model. The inset coordinates represent the slant geometry of SIGMA.

intermediate-scale ionospheric structures at the high latitude regions. This can be achieved using the GNSS scintillation observations and observations from other ancillary instruments coupled with the physical and propagation parameters derived from SIGMA. The sensitivity study of SIGMA presented in this paper will be useful when comparing our results with the GNSS observations which will be our follow-up work. The parameters derived from such a comparison and an inverse method can be used to extract the physics of the irregularity involved in the generation of those scintillations. Good examples of the inverse modeling technique can be found in the works of *Keskinen* [2006] and *Carrano et al.* [2012b], where they use the technique to infer turbulence parameters from intensity scintillation data from the low latitude regions.

In this paper, we investigate the physical, propagation and geometrical input parameters using a sensitivity analysis of the model. Physical parameters include the inner and outer scales of the irregularity, the power index and anisotropy of the irregularity spectrum, while propagation parameters consist of altitude, thickness of the irregularity and the number of layers. Geometrical parameters include the elevation and azimuth of the LOS signal. The outputs from SIGMA are the peak to peak (P2P) variations in the power and phase received on the ground, the GPS scintillation indices S4 (normalized variance of amplitude fluctuations) and σ_ϕ. These outputs are obtained by applying a high-pass filter with a cutoff frequency of 0.1 Hz to the amplitude and phase on the ground. These are also the observables that can be derived from the high rate (typically 50 Hz) data collected by the GPS scintillation monitors. The goal of this work is to determine which observables on the ground are the most sensitive to the SIGMA input parameters.

We describe SIGMA and its implementation in Section 3.2. In Section 3.3, we present our results from the sensitivity study of our model with a discussion about the results in Section 3.4. Finally, we summarize our work and describe our future plans in Section 3.5.

3.2 Description of SIGMA

With a goal to study the physics of the ionospheric irregularities, this work attempts to simulate the 3D propagation of an obliquely incident satellite signal through an irregularity. The irregularity is assumed to be a set of diffractive phase screens or layers aligned along the magnetic field lines. As defined by *Yeh and Liu* [1982], the phrase "phase screen" is used to depict an assumption that every layer is thin enough to introduce random phase fluctuations in the incident signal that are proportional to the electron content in that layer. On the other hand, the amplitude remains unchanged. As the wave propagates in free space between two layers, fluctuations in the amplitude may start to develop. Similar to an approach described by *Grimault* [1998], in SIGMA, we utilize a hybrid numerical technique with the MPS and a split-step method to propagate a satellite signal through an ionospheric irregularity.

The 3D random realization of the electron density in the irregularity can be produced by different types of models. For example, first principle numerical simulations of irregularity density fields can be used [*Gondarenko and Guzdar*, 2001, 2003, 2006; *Keskinen et al.*, 2003, 2006] to generate the realization of the electron density fields. Another way of generating a random realization of the electron density field could be the use of the empirical spectral models of the density irregularities.

While SIGMA can take in any electron density field, for this study, we use spectral models to generate the density field. In this section, we initially present the ionospheric irregularity spectral model and a coordinate system transformation to obtain the spectral model in a reference coordinate system. Following that, we demonstrate the use of the spectral model to obtain a phase at the bottom of a layer. We then discuss updating the incoming electric field at the bottom of the layer, and then obliquely propagating it to the next layer or to the ground. Finally, we briefly describe the split step method and the simulation procedure of SIGMA. We save either 2-dimensional (2D) snapshots of the spatial complex signal at one time instance, or

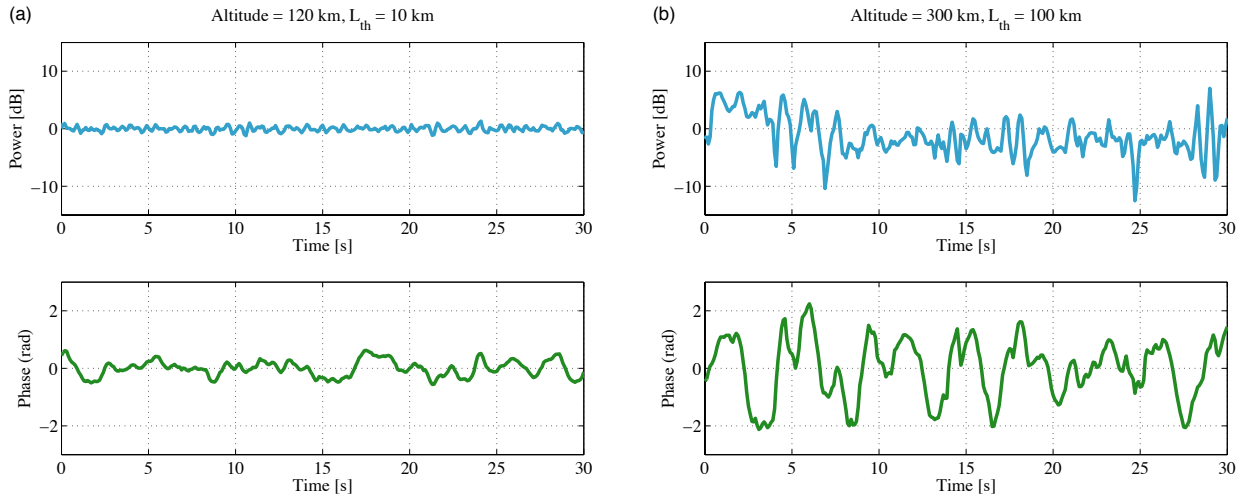

Figure 3.2: Examples of the power and phase time series on ground modeled using SIGMA at altitudes of (a) 120 km and (b) 300 km with irregularity thickness of 10 km and 100 km, respectively. To generate these time series, we used the remaining input values the same as those introduced later in Table 3.1.

a time series of the complex signal at the receiver location on the ground. Two examples of the modeled power and phase time series on the ground with different altitudes and irregularity thicknesses are shown in Figure 3.2. Here, the phase and power are subjected to high-pass filtering with 0.1 Hz cutoff frequency, similar to that used for the real observations to eliminate any low frequency effects including the satellite motion. For the sensitivity study presented in this paper, we use 2D snapshots at one time instance, the examples of which will be shown in the later sections of the paper. Since each of the time series simulations demands higher computation time and memory, we base our sensitivity study on the statistics extracted mainly from the 2D plots.

3.2.1 Spectral Model

For the ease of implementation and because of insufficient high latitude empirical and observational electron density data, we begin with the high latitude power spectral density (PSD) of the electron density fluctuations in an ionospheric irregularity, instead of the actual

spatial distribution of electrons in a slab. There are a number of different types of power spectra that can be used, a simple isotropic power law spectrum, a simple anisotropic power law spectrum [*Rufenach*, 1975] and a generalized "Shkarofsky" spectrum [*Shkarofsky*, 1968], to name a few. In our work, we are using a "Hybrid" spectrum introduced by *Costa and Kelley* [1977] for the high latitude irregularities.

The Hybrid spectrum depicts a Gaussian distribution along the magnetic field in the direction of k'_z and a power law variation in the direction perpendicular to it. The Hybrid spectrum in the irregularity field aligned irregularity coordinate system (introduced in the next paragraph) is defined as:

$$P'_{NH}(\vec{k'}) = \frac{a(\gamma_H - 2)}{2\pi^{3/2}k_0^2}\ \Delta N^2 \left(1 + \frac{k_x'^2 + k_y'^2}{k_0^2}\right)^{-\gamma_H/2}\ \exp\left(-(ak_0)^2 \frac{k_z'^2}{k_0^2}\right), \tag{3.1}$$

where γ_H is the spectral index, ak_0 depicts the axial ratio, and k_0 is the wave number associated with the outer scale l_0. The outer scale is the largest spatial dimension of the ionospheric irregularities. $\Delta N = \langle N^2(\vec{r})\rangle^{1/2}$ is the root mean square (RMS) of the electron density fluctuations $N(\vec{r})$ which are assumed to be generated by a zero-mean stationary random process. Following works of *Costa and Kelley* [1977] and *Gola et al.* [1992], for this study, we assume that the irregularities are field aligned and rod-shaped. The Hybrid spectral model considers different variations in the directions parallel and perpendicular to the magnetic field. The axial ratio is a parameter in this spectral model that defines the anisotropy of the rod-shaped irregularities.

The irregularity spectrum is given in terms of the irregularity coordinate system (in primed coordinates), which is assumed to be aligned with the magnetic field B_0. The field aligned irregularity coordinate system and a reference (topocentric) coordinate system (in unprimed coordinates) centered locally at the receiver location in the Northern hemisphere are shown in Figure 3.3(a). This figure is adapted from the works of *Rufenach* [1975] and *Costa and Kelley* [1977], and is modified to obtain the transformation in the Southern hemisphere as shown in

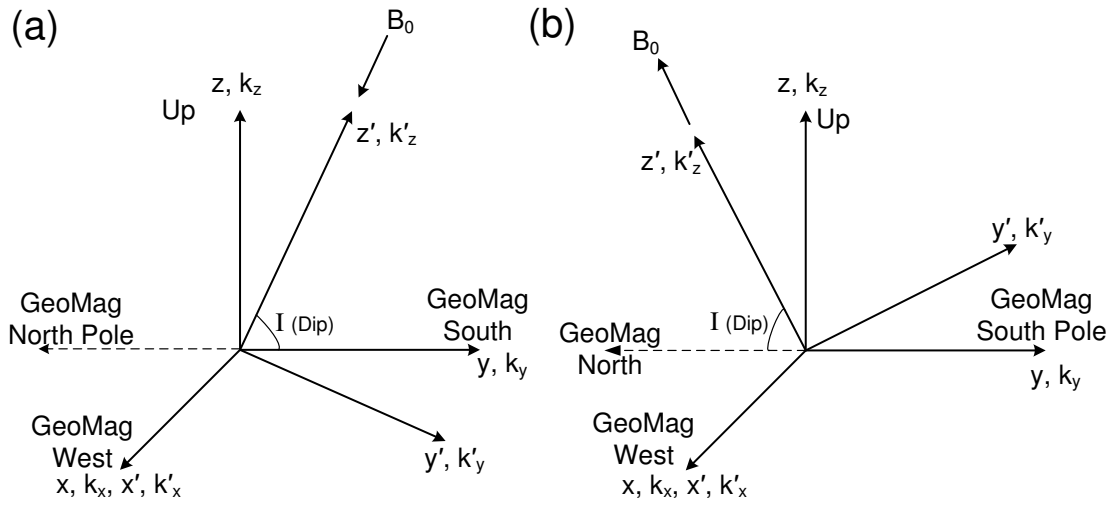

Figure 3.3: Coordinate transformation from magnetic field-aligned irregularity coordinates to local reference coordinates, (a) Northern and (b) Southern hemispheres.

Figure 3.3(b). In Figures 3.3(a) and (b), the vertical direction and B_0 define a plane which is aligned with a magnetic meridional plane. Variables k'_x, k'_y and k'_z are the wavenumber variables in x', y' and z' directions, respectively. Similarly, k_x, k_y, k_z are the wavenumber variables in x, y, z directions, respectively. z' and k'_z are along B_0, while y' and k'_y are in the meridional plane and are in the direction perpendicular to B_0. x' and k'_x along with x and k_x are in the geomagnetic west direction. z and k_z are vertically up at the receiver location, while y and k_y are in the geomagnetic south direction in a horizontal plane perpendicular to z and k_z. The angle I is the magnetic inclination or dip angle.

3.2.2 Wave Field at the Bottom of a Phase Screen

As described earlier, the density fluctuations inside an irregularity layer affect the phase of the incoming signal, whereas its amplitude is assumed to be unperturbed. In the absence of diffraction, the phase perturbation at the bottom of an irregularity layer in a continuously

displaced coordinate system (CDCS) [*Rino*, 2010] can be given as

$$\Phi(\vec{\rho}) = -\lambda r_e \sec\theta \int_{z_s}^{z_e} N_e(\vec{\rho}_d, z) dz, \tag{3.2}$$

where $\vec{\rho}$ is the 2D position vector in the horizontal direction and is given by $\vec{\rho} = x\hat{x} + y\hat{y}$. r_e is the electron radius, and θ is the angle subtended by the LOS vector with the vertical as shown in Figure 3.1. Equation 3.2 is derived in Appendix B. The LOS vector here is defined from the receiver to the GNSS satellite position. $N_e(\vec{\rho_d}, z)$ is a horizontally displaced random realization of the electron number density of the cold plasma and can be derived from the PSD of the irregularity spectra as:

$$N_e(x, y, z) = \Re\left(\mathscr{F}^{-1}\left[\sqrt{P_{NH}}\exp(i2\pi\theta_k)\right]\right), \tag{3.3}$$

where $\mathscr{F}^{-1}$ stands for the Inverse Fourier Transform (3D in this case). θ_k is a statistically independent 3D random number between 0 to 1. $\Re$ depicts the real part of the complex numbers. Taking the real part simply ensures that the random realizations of the electron density are real valued. The PSD P_{NH} is P'_{NH} from Equation 3.1 converted to the local coordinate system.

In Equation 3.2, variable z is in the local coordinate system and has integration limits z_s and z_e. The vector $\vec{\rho}_d$ is in the displaced local coordinate system. The CDCS geometry was introduced by *Rino* [2010] to resolve a problem of significantly increasing support space required to capture the evolution of an obliquely incident field as it propagates through the irregularity. With this, $\vec{\rho}_d = \vec{\rho} + \tan\theta\,\widehat{\mathbf{a}_\perp} z$, where $\widehat{\mathbf{a}_\perp} = [\cos\phi_l, \sin\phi_l]$ is the unit vector of the projection of the LOS vector on the x-y plane as shown in Figure 3.1. θ is the zenith angle (complimentary to the elevation angle) and ϕ_l is the azimuth angle of the LOS vector. With these changes, the spatial phase from Equation 3.2 becomes

$$\Phi(\vec{\rho}) = -\lambda r_e \sec\theta \int_{z_s}^{z_e} N_e(\vec{\rho} + \tan\theta\,\widehat{\mathbf{a}_\perp} z, z) dz. \tag{3.4}$$

For large values of $\tan\theta$ and z, $\vec{\rho}_d$ can get significantly large. In order to have $\vec{\rho}_d$ within the limits, we would have had to make $N_e(\vec{\rho}_d, z)$ large accordingly. But, this would have stretched the computational capacity of SIGMA diminishing its efficiency in generating longer time series. We surpass this computational limitation by imposing periodicity condition on $N_e(\vec{\rho}_d, z)$. This gives us an added advantage of eliminating the edge discontinuity problems, if any.

The wave field propagated through the phase screen will have its phase altered by $\Phi(\vec{\rho})$, and will thus be a different realization of the received electric field. Let $\vec{E}_a(\vec{\rho})$ be an electric field from the satellite or that propagated from the a layer a. If $\vec{E}_a(\vec{\rho})$ is incident on the next layer b, then with $\Phi(\vec{\rho})$ as the perturbed phase at the bottom of layer b, the field at the bottom of the layer b is given by:

$$\vec{E}_b(\vec{\rho}) = \vec{E}_a(\vec{\rho}) \exp(-i\Phi(\vec{\rho})). \tag{3.5}$$

3.2.3 Propagation at an Oblique Angle

A satellite signal exhibits variable angle of incidence based on the motion of the satellite. For this, we need to consider a slant propagation. The expression for propagation at an oblique angle can be obtained by generalizing the propagation expression for vertical incidence given by *Rino and Carrano* [2011]. The vertical propagation expression is given by

$$f(\vec{\rho}, z) = \int \widetilde{E}(\vec{\kappa}) \exp(ikg(\vec{\kappa})(z - z_0)) \exp(i\vec{\kappa}.\vec{\rho})\, d\vec{\kappa}, \tag{3.6}$$

where z is the reference direction along the vertical axis, $z = 0$ is at the top of the irregularity, $z = z_0$ is at the bottom of a layer and $z - z_0$ can be equal to either the distance between two layers or H_{iono}, the height of the ionospheric irregularity. $\vec{\kappa}$ is the 2D horizontal position vector in the Fourier domain and is given by $\vec{\kappa} = k_x\hat{k_x} + k_y\hat{k_y}$. The factor $g(\vec{\kappa})$ is defined as $\sqrt{1 - (k_x^2 + k_y^2)/k^2}$, where $k(= 2\pi/\lambda)$ is the wavenumber or the magnitude of a wavevector and λ is the signal wavelength. Finally, $\widetilde{E}(\vec{\kappa})$ is the electric field in spectral domain at the bottom

of a layer and can be obtained by taking a 2D Fourier transform (FT) of Equation 3.5 as:

$$\widetilde{E}(\vec{\kappa}) = \mathscr{F}[\vec{E}(\vec{\rho})], \tag{3.7}$$

where $\mathscr{F}$ is the 2D forward FT and $\vec{E}(\vec{\rho}) = \vec{E}_b(\vec{\rho})$ from Equation 3.5 at the bottom of the layer b.

In the CDCS, we can obtain the propagation at an oblique angle from the following expression:

$$\begin{aligned} f(\vec{\rho}, z) &= \int \widetilde{E}(\vec{\kappa}) \exp(ikg(\vec{\kappa} + \vec{k_\perp})(z - z_0)) \\ &\quad \exp(i \tan\theta \, \widehat{\mathbf{a}_\perp}.\vec{\kappa}(z - z_0)) \exp(i\vec{\kappa}.\vec{\rho}) \, d\vec{\kappa}, \end{aligned} \tag{3.8}$$

where a spatial variable change of $\vec{\rho}$ and a replacement of $kg(\vec{\kappa})$ was invoked in Equation 3.6 as suggested by *Rino and Carrano* [2011]. The horizontal vector is changed as:

$$\rho \longrightarrow \rho + \tan\theta \, \widehat{\mathbf{a}_\perp}(z - z0). \tag{3.9}$$

$kg(\vec{\kappa})$ is replaced to:

$$kg(\vec{\kappa}) \longrightarrow kg(\vec{\kappa} + \vec{k_\perp}) - \tan\theta \, \widehat{\mathbf{a}_\perp}.\vec{\kappa}, \tag{3.10}$$

where $\vec{k_\perp}$ is the transverse component of $\vec{k_k}$. The wavevector is defined as $\vec{k_k} = k_{kx}\hat{k_x} + k_{ky}\hat{k_y} + k_{kz}\hat{k_z}$, or $\vec{k_k} = k[\sin\theta\cos\phi_l, \sin\theta\sin\phi_l, \cos\theta]$, where k is the magnitude of the wavevector. Here, $\vec{k_k}$ can also be written as $[\vec{k_\perp}, k_{kz} = k \; g(\vec{k_\perp})]$.

If the spatial structure in the irregularity is moving with a velocity $\vec{v_k}$, the 3D irregularity field will move across the LOS field of view. If the field is "frozen-in" and not otherwise evolving in time, we can simulate that motion by simply translating the coordinates of the 3D irregularity

distributions as

$$\vec{\rho} \longrightarrow \vec{\rho} + \vec{v_k}t, \tag{3.11}$$

where $\vec{v_k}$ is made up of a horizontal "drift" component $\vec{v_d}$, as well as a vertical component v_z. Finally, in addition to the irregularities drifting vertically through a fixed layer, we have to consider the entire layer rising or falling vertically. Typically we ignore any vertical motions in the simulation, though they can be included as needed. By allowing the 3D density irregularity field to drift past the LOS as time evolves, and allowing the LOS to move as the satellite (or receiver) moves, we are capable of simulating the full 3D temporal evolution of both motions of the satellite-receiver LOS and drifting of the irregularities. Note, that there is nothing in the physics to stop us from simulating more random velocity fields as well as temporal evolution of the irregularity field. The detailed, step-by-step simulation procedure and setup of SIGMA is described in Appendix A.

3.3 Sensitivity Study

The objective of the sensitivity study of SIGMA is to determine which of the observables are the most sensitive to the input parameters. For the Hybrid spectral model we have selected for this sensitivity study, SIGMA depends on eight different physical and propagation parameters. Physical parameters characterize the ionospheric irregularity. They include the outer scale l_0, RMS electron number density ΔN, spectral index $SpInd$ and anisotropy of the irregularity spectrum defined by the axial ratio. The propagation parameters consist of altitude H_{iono}, thickness of the irregularity L_{Th}, number of layers N_l and drift velocity v_d. Finally, SIGMA also expects some geographical parameters as input. These include the receiver, satellite locations in Earth-centered Earth-fixed (ECEF) coordinates or simply the azimuth and elevation angles of the LOS vector and the dip angle at the receiver location. Currently, SIGMA assumes a constant dip angle, i.e., a curvature in the field lines is ignored. The receiver and satellite locations are converted into the local coordinate system. All these input parameters are summarized in

Table 3.1: SIGMA Input parameters. The parameters we focus our sensitivity study on are shown in blue.

Irregularity	**Parameters**
l_0	Outer scale (2 km)
SpInd	**Spectral index** (3)
$\boldsymbol{\Delta N}$	**RMS electron density** fluctuation (2e11 el/m^3)
AXR	**Axial ratio** (5)
Geographical	**Parameters**
I	Dip angle (73°)
LOS(Elv,Az)	LOS vector **elevation and azimuth** (50°,160°)
Propagation	**Parameters**
H_{iono}	Altitude (120 km)
N_l	Number of layers (1)
$\boldsymbol{L}_{\text{Th}}$	**Thickness** (10 km)
v_d	Drift velocity (500 m/s)

Table 3.1. The inputs we focus our sensitivity study on are highlighted in the same table.

In this study, we choose the spatial resolutions in the x and y directions to be isotropic and equal to 50 m. This is below the anticipated Fresnel scale in the E-region ($\sim$ 110 m at GPS L1 frequency). We compute the resolution dz in the z direction such that it satisfies two conditions: first, it is much smaller than the coherence length in the z direction, and second, the horizontal projection of dz is smaller than the Fresnel scale. The value of dz comes around 40 m. The horizontal extent in the x and y direction is 20 km (L_x and L_y in Figure 3.1). But, this may increase when we change L_{Th}.

Each of the input parameters are adjusted independently of the others to isolate the effects of those adjustments on the model's outputs. The "base" values of input parameters are listed in the brackets in Table 3.1. Currently, we are focusing on five input parameters: the elevation and azimuth angles of the LOS vector, axial ratio, spectral index, thickness of the irregularity and RMS electron density fluctuations. The base values of these selected parameters are highlighted in Table 3.1. For this study, we assume weak scattering, so that we do not need multiple layers.

Thus, we have chosen the base values that result in weak scattering. Also, we chose the base irregularity spectrum parameters such that our assumption of field aligned and rod-shaped irregularities holds. Furthermore, as we will show later, the base value of the LOS vector direction is not in any preferred direction. Additionally, it was obtained from a real satellite position in the skies above the geographic South Pole, which is the receiver location for most of the sensitivity study runs.

The main reason we chose these parameters is that they represent conditions similar to those observed in the high latitude scintillation observations. Furthermore, *Rino* [1979] did not find any evidence of finite outer scale cutoffs. This compelled us to believe that the outer scale is a precarious parameter to investigate. We also emphasize here that a full-blown parametric study of all these parameters is out of the scope of this work. Thus, for each sensitivity study, we vary just one parameter at one time keeping the rest of the inputs to their base values. In the following subsections, we present the sensitivity study and detailed analysis with respect to each of the five selected input parameters.

3.3.1 Effects of the LOS Azimuth and Elevation

The LOS azimuth and elevation angles are the geographical input parameters to SIGMA and can be derived from the satellite and receiver locations. Even in the polar regions, at least 7 GPS satellites are available at any instance. Therefore, we believe it is useful to derive the impact of the orientation of a satellite with respect to a receiver in the presence of the magnetic field, on the GNSS signal scintillations.

We illustrate the modeled variations in the P2P power, P2P phase, S4 and σ_ϕ with respect to the elevation and azimuth angles as skyplots shown in Figure 3.4. The inclination angle θ defined in Figure 3.1 is complimentary to the elevation angle. The skyplots are generated at the geographic South Pole. According to our local coordinate system in Southern hemisphere shown in Figure 3.3(b), +y axis is towards the geomagnetic South Pole, +x axis is towards the

geomagnetic west and it corresponds to an azimuth of 0°. The 2D plane seen in Figure 3.4 is basically a plane obtained by looking down along z-axis in Figure 3.3(b). The magnetic field, B_0 at the geographic South Pole is tilted in −y direction or 270° azimuth with a dip angle of 73°. The dip angle is measured from ground similar to an elevation angle. Thus, in Figure 3.4, B_0 is shown as a square at an azimuth of 270° and an elevation of 73°.

It can be observed from these figures that the power and phase variations peak when the azimuth and elevation angles of the LOS vector is 90° and 73°, respectively. The reason for a higher variation in this direction was deduced from the 2D plots on the ground. The 2D phase plot for this case showed isotropic structures, while for all other cases, the plots displayed anisotropic structures. The 2D phase plots for 2 cases (azimuth, elevation) of (90°, 73°) and (160°, 50°) are displayed in Figure 3.5. We would like to bring to the readers' attention that our base values of the azimuth and elevation angles (160°, 50°) denote a non-preferred LOS direction (illustrated by a triangle in Figure 3.4). This can be seen from Figures 3.4 and 3.5. Another observation from Figure 3.4 is that P2P phase shows some high values at 45° and 135° azimuthal directions, but they are not as strong as those in 90° azimuthal direction.

Furthermore, in Figure 3.6(a) we investigate the sensitivity of the modeled outputs to the elevation angles for an azimuth of 90°. The P2P power shows a stronger dependence on the elevation angles than the P2P phase. σ_ϕ appears to be more strongly dependent on the elevation angle compared to S4, but as we will quantify later in Section 3.4, it is in fact S4 that displays stronger dependence on the elevation angles than σ_ϕ. We will return to this in detail later in the Section 3.4.

3.3.2 Effects of Axial Ratio

The axial ratio defines the anisotropy of the field aligned rod-like irregularities and is basically the length to diameter ratio. *Wernik et al.* [2007] mention that the axial ratio is not a direct observable and one cannot directly find its values from received data. They also

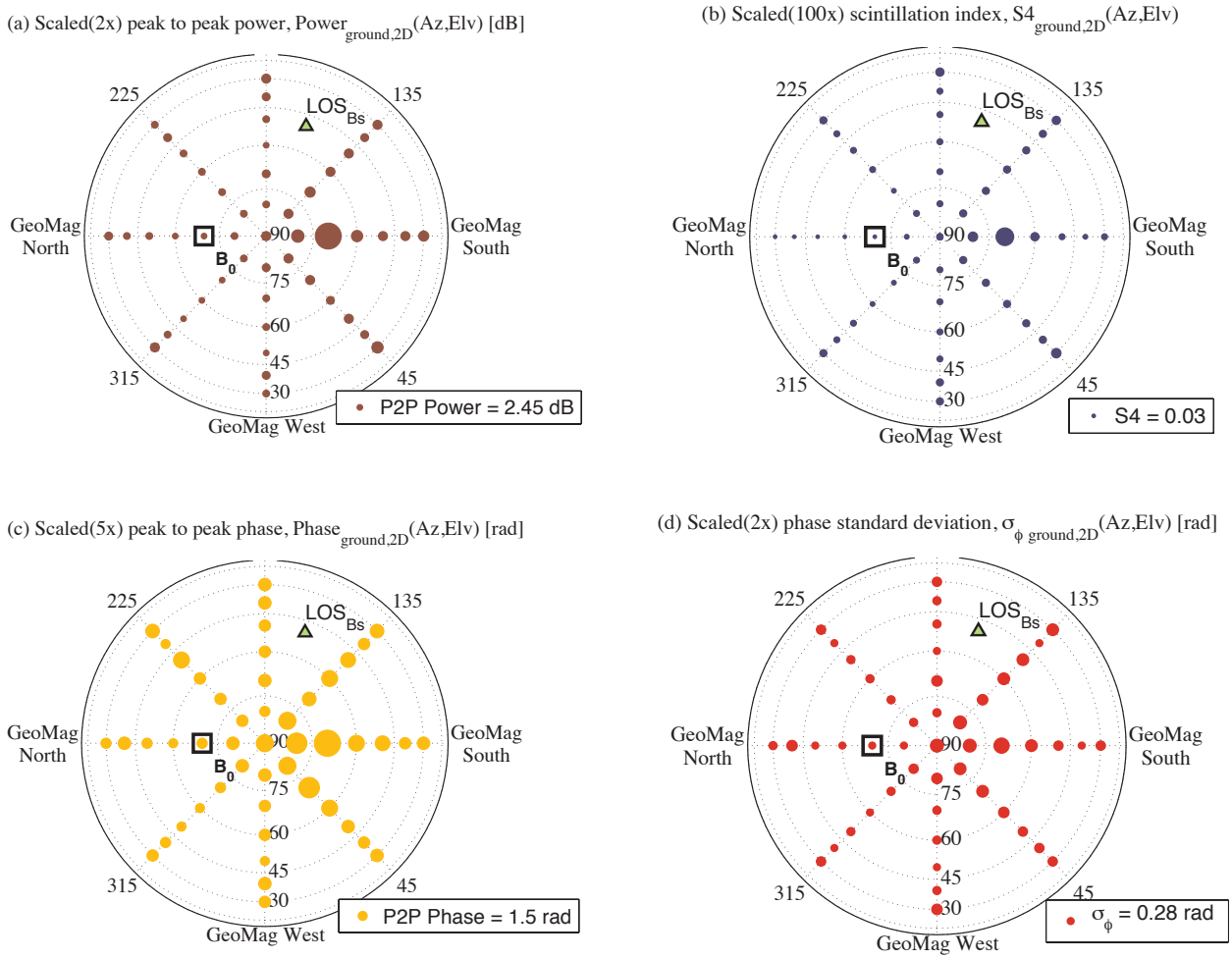

Figure 3.4: Sensitivity study 1: Sky plots of the SIGMA outputs (S4, P2P power, σ_ϕ, P2P phase). Elevation angles range from 90° at the center to 0° at the periphery. The concentric circles are constant elevation circles spaced 15° apart. Azimuths vary from 0° to 360° in anti-clockwise direction starting at Geomagnetic West. The squares indicate the magnetic field (B_0) direction, while the triangle indicates the base value of the LOS vector ($\mathrm{LOS_{Bs}}$).

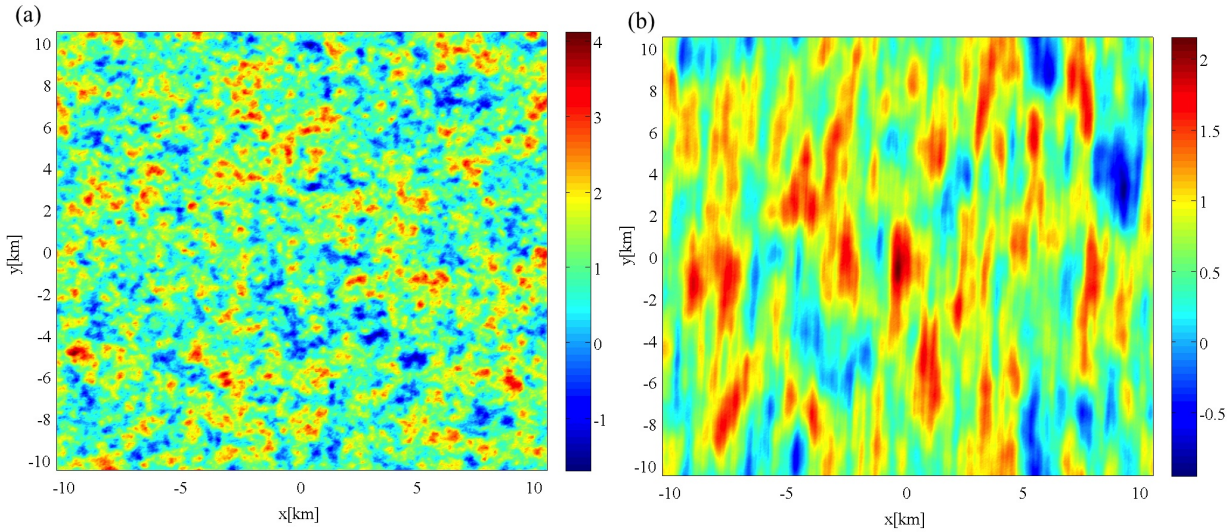

Figure 3.5: Sensitivity study 1: (a) 2D phase plots at (azimuth, elevation) = (90°, 73°) showing isotropic structures and (b) 2D phase plots at (azimuth, elevation) = (160°, 50°) showing anisotropic structures.

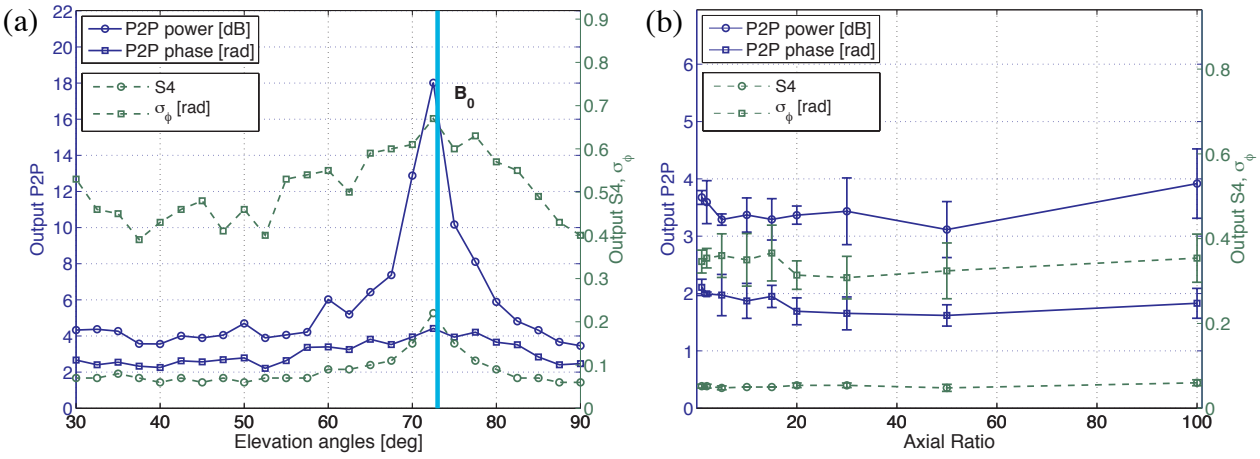

Figure 3.6: (a) Sensitivity study 1: Dependence of modeled outputs on elevation angles at azimuth of 90°. A line showing the dip angle of 73° at the geographic South Pole is displayed with label B_0. The actual direction of B_0 has an azimuth of 270°. (b) Sensitivity study 2: Dependence of the SIGMA outputs on the axial ratio of the field aligned irregularity with errorbars computed over 50 runs. In both the plots, the solid lines represent the P2P variations, while the dashed lines represent S4 and σ_ϕ.

correctly state that not much is known about the anisotropy of the field aligned irregularities. It is hypothesized that at high latitudes, irregularities are rod shaped and they decrease in length as the latitude increases. But, it is hard to prove this with a lack of evidence. Additionally, *Wernik et al.* [1990] have found that anisotropy depends on the scale of the irregularities. In spite of this, all the earlier works by Rino as well as SIGMA assume a constant anisotropy for all scale sizes. In this work, we attempt to investigate the axial ratio of the high latitude irregularities.

Variation of the modeled outputs with respect to the axial ratio is presented in Figure 3.6(b). The error bars in Figure 3.6(b) represent the level of variability in our simulation simply due to variations in the random realization of the density structures. They represent the following approximate limits on the accuracy of our simulation results: 1 dB P2P power, 0.5 radians P2P phase, 0.1 radians σ_ϕ, and 0.02 S4. Variations in any of the sensitivity studies that are less than these limits should be considered due to simulation "noise". It should be remembered that the random realizations are based upon statistically independent random variables generated using a completely different seed at each time. The S4 values do not seem to vary much for different runs. The P2P phase and σ_ϕ have a similar trend. Even though it may appear that the outputs remain mostly unchanged as the axial ratio changes, there are higher variations in the outputs at lower axial ratios. For axial ratios greater than or equal to 30, the outputs appear to stabilize. But, a closer examination of the 2D phase plots for those axial ratios reveals that similar looking long phase structures oriented almost along the y direction start to occur for increasing axial ratios as shown in the set of plots in Figure 3.7. Additionally, the 2D plots implied that for the axial ratios lower than 5, the structures look more isotropic.

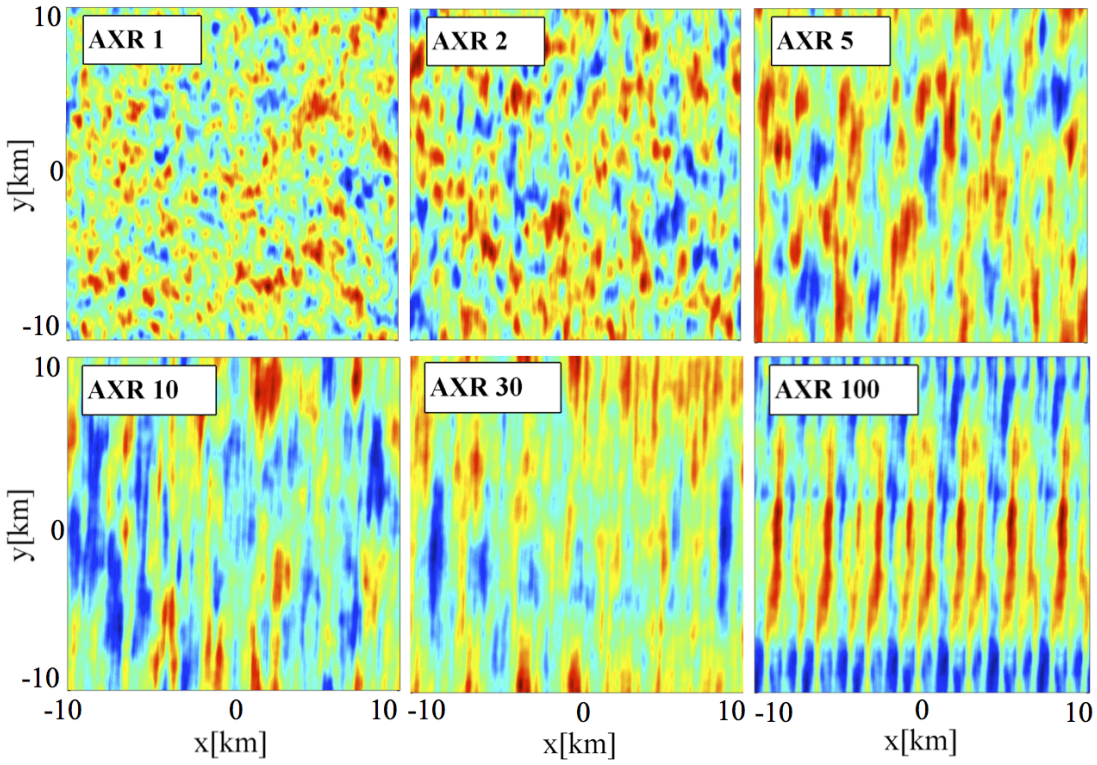

Figure 3.7: Sensitivity study 3: 2D phase plots on ground at different axial ratios. Long structures oriented along y-direction start to appear at high axial ratios.

3.3.3 Effects of Spectral Index

The spectral index of an irregularity spectrum is an important input parameter. A number of studies have attempted to discern this index from rocket, satellite data, and have proposed several spectral models for high latitudes irregularities [*Dyson et al.*, 1974; *Rufenach*, 1975; *Costa and Kelley*, 1977]. Similar to the axial ratio, the spectral index of an irregularity spectrum cannot be directly measured from the GPS data observed on the ground. We believe that with the help of SIGMA, it will be possible to study the spectral index of an irregularity spectrum for a given scintillation observation. We try to estimate its effect on the observables in this section.

Strangeways [2009] and *Strangeways et al.* [2011] derive the ground spectral indices from the observed S4 and σ_ϕ instead of the high rate phase and amplitude time histories. We expect to get the high rate GPS observations to allow us to determine the spectral index on the ground which through the inverse modeling can be related to the irregularity spectral indices.

As seen from Figure 3.8(a), the P2P phase and σ_ϕ increase slowly with the input (irregularity) spectral index, while the P2P power decreases rapidly with increasing input spectral index. Between spectral index of 3 to 3.5, the P2P phase decreases from 2.2 rad to 2 rad, but σ_ϕ increases from 0.32 rad to 0.48 rad. These variations are within the error bar limits derived from Figure 3.6(b), and thus should not be considered as true effects.

In the 2D phase plots, the 2D structures appear to be more striated in one direction at lower input spectral index values, while they get more diffused and spread in all directions as the input spectral index increases. In the 2D power plots, the anisotropy increases as a function of the spectral index. This is the reason for decreasing P2P power with increasing spectral index.

The phase spectrum of the signal received on the ground is generally assumed to have a single slope. The slope of a linear fit to such spectrum can be found between its upper and lower cutoffs on a log-log scale. Examples of the power and phase spatial spectra in the spatial

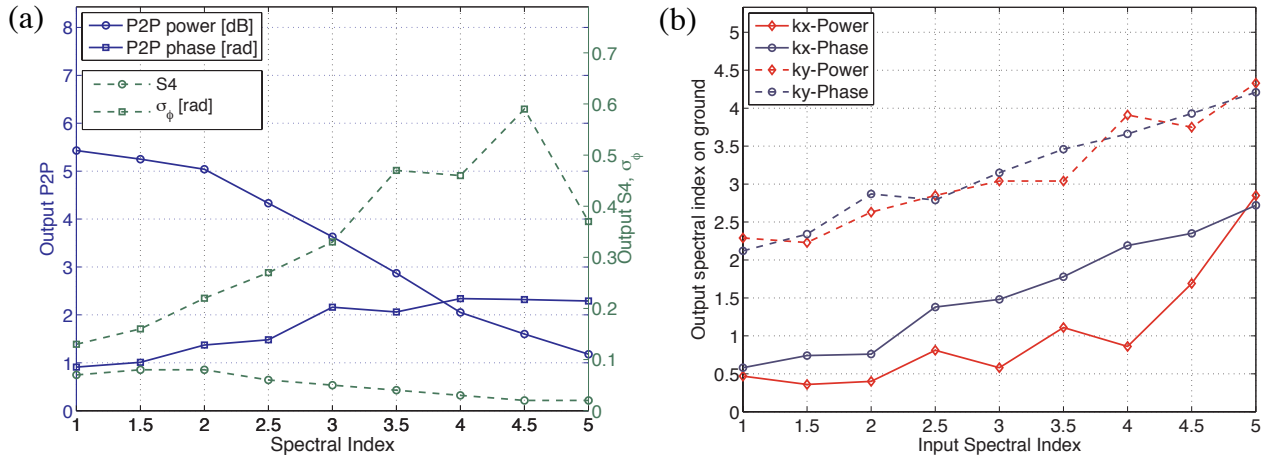

Figure 3.8: (a) Sensitivity study 3: Sensitivity of the SIGMA outputs with respect to the spectral index. The solid lines represent the P2P variations, while the dashed lines represent S4 and σ_ϕ. (b) Sensitivity study 3: Spectral index on ground plotted against spectral index in the irregularity spectrum. kx-Power and ky-Power are the spectral indices on the ground of the spatial spectra of the power in the x and y directions, respectively. kx-Phase and ky-Phase are the spectral indices on the ground of the spatial spectra of the phase in the x and y directions, respectively.

frequency or the wavenumber domain (k-space) on the ground in the x and y directions are displayed in Figure 3.9. The green straight lines depict the linear fits for each spectra. Spectra in the x-direction show more jitter compared to that in the y direction. Also, a part of the power spectra in the y-direction between kf and k0, closer to k0 show reduction in the power as the wavenumber decreases. This could be related to the anisotropy of the irregularity as mentioned by *Strangeways* [2009].

In Figure 3.8(b), we plot the spectral index of the power and phase spectra on the ground in both the x and y directions as a function of the input spectral index (or the spectral index of the irregularity spectrum). The power and phase spectra on the ground display an overall ascending trend. The spectral index on the ground increases with the input spectral index, but the indices in space and on the ground differ from each other.

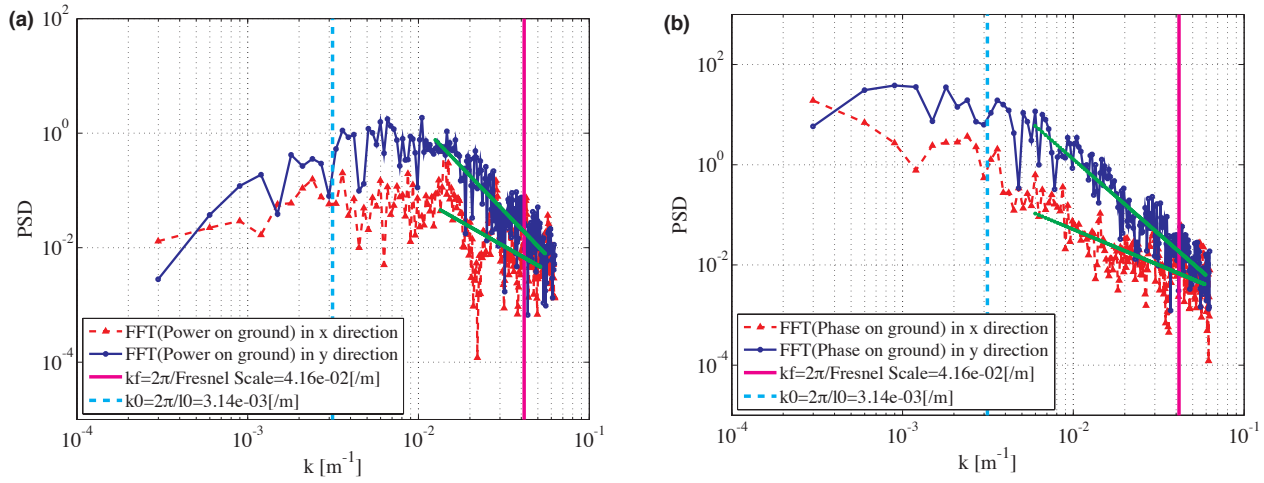

Figure 3.9: Sensitivity study 3: Examples of (a) power and (b) phase spectra on ground in the x and y directions. The input spectral index for these plots was equal to 3.

3.3.4 Effects of Irregularity Thickness

The phase screen theory assumes that the irregularity is represented as a thin slab [*Yeh and Liu*, 1982]. The change in the phase of the incident wave is proportional to the deviation of the TEC through the slab, and thus to the thickness (L_{Th}) of the irregularity as well as the RMS electron density fluctuations (ΔN). Changing the thickness of the layer will reflect in a different irregularity "strength". Thus, a good way to understand the effect of changing the irregularity thickness is to look at the change in the output for a given change in TEC. This can be represented as $L_{Th}\,\Delta N$ in TEC units (TECU), where 1 TECU is equal to 10^{16} electrons/m^2.

In Figure 3.10(a), we present the variations in the SIGMA outputs with respect to L_{Th}. The thickness in kilometers is shown on the lower horizontal axis, while in TECU for the base ΔN is given on the upper horizontal axis. As the thickness of the irregularity increases, the strength of the TEC fluctuations increases and thus, the phase and power variations increase. This can be seen in Figure 3.10(a).

From 0.1 TECU to 0.8 TECU, which corresponds to the thickness of 10 to 40 km, the P2P power increases with a slope of about 5. Above 0.8 TECU it appears to stabilize, but below

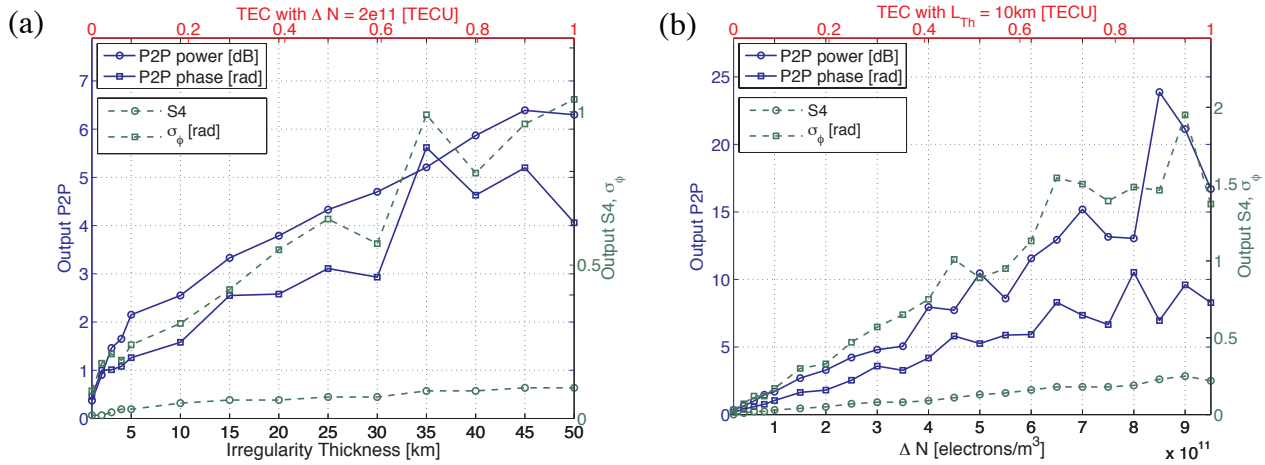

Figure 3.10: (a) Sensitivity study 4: SIGMA output dependence on the irregularity thickness. The thickness values in TECU are given in top X-axis. (b) Sensitivity study 5: SIGMA output dependence on the RMS electron number density (ΔN) in electrons/m^3. The ΔN values in TECU are given in top X-axis. In both the plots, the solid lines represent the P2P variations, while the dashed lines represent S4 and σ_ϕ.

0.1 TECU, the power exhibits a slope of 22. The P2P phase, on the other hand, demonstrates a gradual slope of about 3 between 0.1 TECU to 0.6 TECU. Below 0.1 TECU, it displays a bit higher slope of 7, while above 0.6 TECU, there are sharper variations. An increasing trend similar to P2P power is seen in S4, albeit with very small slopes (< 0.2). Similarly, a trend that looks like that of the P2P phase, although with slope < 1 is seen in σ_ϕ.

The 2D phase structures look like large patches dispersed in all directions for TECU values smaller than or equal to 0.1 TECU ($L_{Th} = 5$ km). On the other hand, above 0.1 TECU, the phase structures appear to get thinner in one direction as L_{Th} increases. The 2D power plots display similar thin structures as the 2D phase plots.

For this part of the sensitivity analysis, we used a spatial resolution of 200 m in the x and y directions. The reason for this change is, to have computationally manageable number of grid points as the size of the simulation box increases with increase in thickness. In the path integrated phase computation given by Equation 3.4, the number density N_e is computed over the displaced coordinate system governed by the thickness of the layer. Hence, the size of the

simulation box increases with thickness.

3.3.5 Effects of RMS Electron Density Fluctuations

Variation in the RMS electron number density or ΔN changes the strength of the irregularity as explained in Section 3.3.4. Similar to the irregularity thickness, with increasing ΔN, the fluctuations in the phase and power on the ground increase. This can be seen in Figure 3.10(b).

The P2P power graph in Figure 3.10(b) can be divided into three parts. The first one upto 0.35 TECU, the second one from 0.35 TECU to 0.7 TECU and the third one above 0.7 TECU. In terms of ΔN, 0.35 TECU corresponds to 3.5×10^{11} electrons/m^3 and 0.7 TECU corresponds to 7×10^{11} electrons/m^3. The first and second parts show somewhat gradual increase with slopes equal to 14 and 29, respectively. Similarly, the P2P phase graph displays slopes equal to 9 and 12 for the first two parts. Although the σ_ϕ plots show similar trend to these two graphs upto 0.7 TECU, a closer examination reveals that the slopes of those first two parts are 2 and 2.5, respectively. S4 appears to have the least dependence on ΔN with very small slopes, close to 0.3. The 2D plots do not display obvious visual variation in the structure shapes.

For this sensitivity analysis part, we retain the spatial resolution in the x and y directions as 50 m. Despite of this high spatial resolution, cases where $\Delta N \geq 1 \times 10^{12}$ electrons/m^3 produce 2D phase plots with rapidly wrapped phases which are difficult to unwrap properly with our existing algorithms.

3.4 Discussion

In the previous sections, we describe the electromagnetic propagation through ionospheric electron density perturbation model, SIGMA. We also present the results of a study, based on the use of SIGMA, of the sensitivity of the GNSS scintillation observations on the ground to various physical parameters that describe the irregularity medium. The model itself is different

from previous numerical propagation models such as [*Gherm et al.*, 2000, 2005a, b; *Maurits et al.*, 2008; *Béniguel*, 2002; *Béniguel and Hamel*, 2011; *Carrano et al.*, 2011, 2012a] in several important and unique respects. To begin with, the MPS hybrid split-step method is, in principle, an exact numerical implementation the propagation equations, up to the standard assumptions of the forward scattering and numerical limitations on the minimum spatial resolution. In fact, by stepping through layers and then propagating, we recover the continuous forward scatter integration through the irregularity layer, including arbitrary strong, multiple scattering. This differentiates our model from more approximate wave representations such as [*Gherm et al.*, 2000, 2005a, b; *Maurits et al.*, 2008; *Béniguel*, 2002]. However, the numerical implementation of *Carrano et al.* [2011] and *Carrano et al.* [2012a] is also an MPS hybrid split-step method based on the derivation by Rino [*Rino*, 2010]. Where we differ from their work is in the exact representation for the arbitrary geometries, including very high latitude geometries. There are several unique features for propagation through the random media at the high latitude regions. First, since the magnetic field is nearly vertical, and typically irregularities extend along the field lines to the large scales, the approximation that the layer thickness L_{Th} is much larger than the correlation length ($l_0\times$ AXR) along the propagation direction is no longer valid. Thus, the calculation of the phase perturbation through an irregularity layer (see Equation 3.4) has to be done by numerical integration through the layer, and separately for each layer in the MPS approximation.

If the approximation that the layer thickness is much larger than the correlation length along the propagation direction holds true, in SIGMA, we can always go back to the traditional MPS method. In that case, the spatial phase can be obtained by taking the two dimensional (2D) inverse Fourier transform of the spectral phase given by the following expression:

$$\Phi(\vec{\kappa}) = \lambda r_e \sec\theta \sqrt{L_{Th}} \sqrt{P_{NH}(k_x, k_y)} \exp(i2\pi\theta_l) \tag{3.12}$$

where the 3D power spectrum P_{NH} given by Equation 3.1 is reduced to a 2D spectrum with a

substitution: $k_z = \tan\theta\ (\widehat{\mathbf{a}_\perp}.\vec{\kappa})$. The exponential part imparts a randomness to the fluctuations in the spectral domain. θ_l is a set of statistically independent 2D random numbers between 0 to 1. In Figure 3.11, we illustrate the difference between the traditional MPS method and the modified MPS method discussed in Section 3.2. The plots included in this figure are at axial ratios of 5 and 20 for both the traditional and modified MPS methods. For these runs, the SIGMA parameters are as follows: $l_0 = 3$ km, $L_{Th} = 40$ km and $\Delta N = 2.5\text{e}11$ (the irregularity strength = 1 TECU). The rest of the parameters with an exception of AXR are the same as the base values given in Table 3.1. For the axial ratio of 5, the correlation length along the direction of propagation is 15 km. This value is smaller than the thickness of the irregularity and thus the plots display similar 2D phase structures for both the methods. But, when the axial ratio is 20, the correlation length is 60 km. For this case, sharp and unrealistic 2D phase structures appear along the y-direction in the 2D phase plot with traditional MPS method in Figure 3.11, as against the structures in the phase plot with the modified MPS method. This illustration explains that the traditional MPS method can be used safely when the correlation length is well below the layer thickness. Additionally, it justifies the application of the modified MPS method in SIGMA for the high latitude regions whenever the assumption for traditional MPS method is invalid.

The second issue related to the propagation at high latitudes is the arbitrary 3D geometry. We have our final, analysis coordinate system as a local geomagnetic coordinate system, with the "z-axis" radially outward, x to the west and y to the south as shown in Figure 3.3. But the natural coordinate system for the irregularities is along and perpendicular to the magnetic field. Thus, we have a coordinate transformation that changes anytime we move to a different magnetic dip latitude. This continuously displaced coordinate system has been implemented by *Rino* [2010] and *Carrano et al.* [2012a] before, but not for the generalized case of 3D number density fluctuations discussed in this paper. Finally, we have to account for the slant path of the signal line-of-sight between the transmitter and receiver on the ground. For very high latitudes the GPS elevation angle is quite low (46 degrees or less at the South Pole). This implies that

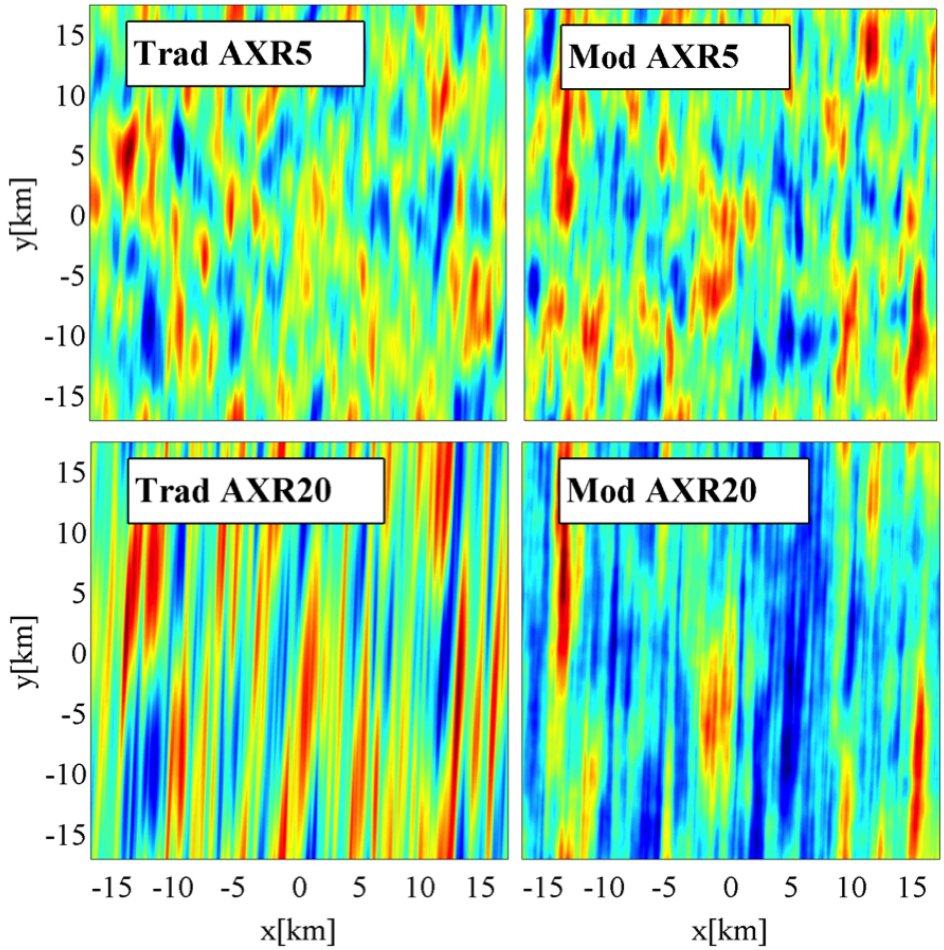

Figure 3.11: 2D phase plots on ground for the traditional MPS method and modified MPS method.

the horizontal extent of the signal trajectory as it passes through the layer is at least as large as the vertical extent of the layer. For the larger layers, especially in the F-region, we have to simulate $\sim$ 100 km or larger horizontal regions, which carries with it its own unique numerical challenges. All of these issues are dealt within SIGMA, while still maintaining generality, high accuracy and fidelity. Thus, SIGMA can be used to study the propagation of the EM waves through the random electron density fluctuations anywhere on the globe, and at any altitude. As far as the authors are aware, this global, arbitrary geometry capability is unique to SIGMA. It should be noted that, although we are mostly dealing with weak scattering for the Hybrid model selected in this study, SIGMA has capability to work with strong scattering cases as well.

One of the numerical limitation of SIGMA is the minimum resolution we can take in the x, y and z directions, retaining an expedient amount of the simulation memory and computation time. As mentioned at the beginning of Section 3.3, we are considering the spatial resolutions in decameters. This works well for our purpose, since we are interested in looking at the intermediate scale structures with scale sizes from 100 m to 100 km. Another numerical limitation of SIGMA is that the computational resources will effectively determine how high an anisotropy ratio we can properly accommodate in a simulation for a given outer scale.

We begin our sensitivity study by examining the statistics of the phase and amplitude variations on the ground with respect to the variations in the signal elevation and azimuth. In section 3.3.1 we show that there is a peak in the observed parameters when the elevation angle of the LOS vector is equal to the dip angle of the magnetic field and the LOS azimuth was 180° from the azimuth of the magnetic field B_0. To determine whether this is a general effect for any magnetic dip angle, we repeated the test for different receiver locations in the Southern (at 40° dip angle) and Northern hemisphere (at 50° dip angle). In each case, we noticed a clear peak when the elevation of the LOS vector was equal to the dip angle and the azimuth was in the direction opposite to B_0. We believe that this enhancement in the

phase and amplitude scintillations at the dip angle elevation is related to the propagation path geometry and the projection of the plane normal to the LOS vector in the presence of the ionospheric irregularities oriented along an inclined magnetic field. When there is a preferred LOS elevation and azimuth relative to B_0, the 2D phase and amplitude fluctuations observed on the ground are approximately isotropic, with smaller scales dominant (Figure 3.5(a)). By preferred direction we mean, the LOS elevation angle equal to the dip angle and the azimuth angle equal to 180° plus the azimuth of the magnetic field B_0. However, for an arbitrary LOS, the observations are non-isotropic, with one direction having elongated structures relative to the other (Figure 3.5(b)). The amount of this elongation will depend on the magnetic dip angle, as well as the aspect ratio of the along-the-field irregularities compared to the irregularities perpendicular to the field. Since, there is more random structure for smaller, isotropic scales there will be higher statistical levels of S4 and P2P for the amplitudes. This analysis is for statistics over a 2D spatial region. For a more typical case of a time-series due to irregularities drifting past the LOS, we would expect higher values of amplitude scintillation when the drift velocity is along the axis with smaller scale irregularities, that is along the magnetic East-West direction. At high latitudes, the structures that cause scintillations (auroral arcs, polar cap patches) are moving in a magnetic North-South direction (towards the pole or away from the pole). This may be one of the reasons for the observed lesser occurrence of strong amplitude scintillations compared to the phase scintillations in those regions [*Aarons*, 1997; *Basu et al.*, 1998; *Mitchell et al.*, 2005; *Kinrade et al.*, 2012; *Deshpande et al.*, 2012; *Kinrade et al.*, 2013], where both the direction and magnitude of the irregularity drift might be the responsible factors.

In sections 3.3.2, 3.3.3, 3.3.4 and 3.3.5 we investigate the sensitivity of the ground observables to the axial ratio, spectral index, layer thickness and overall strength of the irregularities, respectively. The goal is to obtain a better understanding of what the observables can tell us about the underlying irregularity structuring. The most interesting result is how the P2P variations in the phase and amplitude depend upon the spectral index of the irregularity spectrum. In Figure 3.8(a), the P2P power is approximately constant for smaller values of spectral index,

until the spectral index reaches ~ 2. For values greater than ~ 2 to 4, the P2P power falls off quite rapidly. For the P2P phase variation the situation is different. First, the dependence on the spectral index is weaker for the phase. Second, the P2P phase actually increases somewhat with larger spectral index. The case is similar for σ_ϕ and S4, although the dependence of S4 is less pronounced. Another interesting aspect of Figure 3.8(a) is the fact that the σ_ϕ seems to peak at the spectral index of ~ 4.5.

To study the effect of the spectral index in greater detail, we compute the spatial spectra on the ground from the phase and amplitude structuring in both the x and y directions. The spectral indices of the spectra observed on the ground are expected to be different than those in the irregularity spectra. This is because of the non-linear transformations on the signal propagating through the irregularity and space. We compute the ground spectra by determining the region where there is an approximately linear decrease in the power with frequency (the inertial sub-range). We determine this region by visual inspection of the higher cut-off (close to the Fresnel scale) and lower cut-off (before a roll over). Figure 3.9 shows an example of the power and phase spectrum and the linear fit. The spectral indices of the phase spectra on the ground in Figure 3.8(b) appear to increase with the input spectral index in both the x and y directions. Both the phase and power spectral indices in the y-direction increase in a linear fashion, with the ground index p given from the irregularity index p_i by the linear relation $p \approx 1.75 + 0.5 p_i$. This is significantly different from the structure of the observed spectral index on the ground in the x direction. First, while the phase spectral index relation is approximately linear, this is not the case for the power index. The power spectral index (red solid curve with diamond markers in Figure 3.8(b)) increases slowly for the irregularity spectral indices < 4, with the ground power index ~ 0.5 to 1. Then, for irregularity spectral indices ranging from 4 to 5, it rapidly increases to almost 3, which is clearly a non-linear response. The slope of the phase spectral index in the x direction is approximately the same as the slopes for the y-direction, though the zero intercept is closer to 0.

From Figure 3.3(b), we know that the magnetic field is in the -y direction. In other words, the x direction is perpendicular to B_0. Thus, we believe that the dissimilarity we see in the x and y directions in Figure 3.8(b) is because of the presence of B_0 and the anisotropy of the irregularity itself. For 3D isotropic spectra, the relation between the spectral index on the ground in one direction (1D) spectra and the 3D spectral index is found to be $p = p_i - 1$ [*Yeh and Liu*, 1982], which is different from the relation we are getting. However, for the case under study in this paper we have an anisotropic 3D spectra, so we do not expect the same result.

Another interesting feature in the sensitivity analysis is the variation in the ground observables with respect to the changes in the axial ratio, for ratios < 30. For the larger axial ratios, the coherence length along the z-axis becomes larger than the thickness of the layer (10 km) and thus the ratios have no effect on the observations. For the smaller axial ratios there seems to be a definite minimum for an axial ratio of ~ 20. This exact value of the axial ratio is likely modified by other parameters including the LOS of the signal. Still, Figure 3.7 demonstrates that the 2D phase pattern ground observables are sensitive to the axial ratio. Thus, a 2D array of GPS scintillation receivers capable of imaging the ground phase structure could be used, in combination with SIGMA modeling, to study the axial ratio of irregularities at high latitudes.

The final set of parameters are the layer thickness and the strength of the irregularities. Previous studies [*Booker et al.*, 1985] have shown that the total path integrated density fluctuations of the layer, given by the product of the irregularity strength and layer thickness is the relevant parameter for observed scintillations. However, those studies generally assumed the irregularity coherence length along the layer direction (z-axis) to be much less than the layer thickness. For the high latitude case where the magnetic field direction is nearly vertical, the coherence length can be several tens of kilometers and comparable to the layer thickness. Thus, the assumption does not necessarily hold. To investigate whether the TEC is the relevant parameter at high latitudes, we separately varied the thickness and irregularity strength. An extra X-axis in Figures 3.10(a) and 3.10(b) is shown in TECU to facilitate the comparison. The slopes

Table 3.2: SIGMA sensitivity study results in terms of a quantitative parameter: $Q_\beta = (\beta_{max} - \beta_{min})/\beta_{max}$ where β is an observable.

Q_β	Elv-Az (Az=90°)	AXR	$SpInd$	L_{Th}	ΔN
Q_{S4}	0.73	0.17	0.75	0.90	1
Q_{σ_ϕ}	0.42	0.4	0.78	0.91	0.98
$Q_{P2PPower}$	0.81	0.17	0.78	0.94	0.99
$Q_{P2P\phi}$	0.50	0.33	0.61	0.92	0.98

with respect to TECU in Figure 3.10(b) are higher compared to those in Figure 3.10(a). This is an indicator that the RMS density fluctuation has a stronger effect on the SIGMA outputs than the irregularity thickness. However, an interesting result is that for small layer thicknesses ($\sim$ 5 km or less) the P2P phase and power seem to rise quite rapidly with increasing thickness (Figure 3.10(a)), then for larger thicknesses, the P2P values increase linearly with thickness (as expected), until for very thick layers ($>$ 40 km) the P2P power and phase seem to level off or even decrease. A similar, but smaller effect is seen in the σ_ϕ in Figure 3.10(a). Interestingly, no such effect is observed for the irregularity strength in terms of ΔN (Figure 3.10(b)), which indicates that the two parameters have somewhat different effects upon the observables, and a single product parameter such as TEC is insufficient.

The sensitivity plots obtained from Section 3.3, can be interpreted in different ways. We present Table 3.2 to quantitatively list out the sensitivity of the individual output parameters to each of the input parameters. The quantity that is presented here is $Q_\beta = (\beta_{max} - \beta_{min})/\beta_{max}$, where β is an observable. It basically exemplifies the spread in each output variable in a sensitivity study, normalized with its maximum value.

Based on the values we obtained in Table 3.2, our initial question: which of the output parameters gets affected the most in case of varying each of the input parameters individually, can be answered to some extent as follows. From this study, we found that the P2P power gets affected the most for changes in the azimuth and elevation, while changes in axial ratio majorly

affect the P2P phase and σ_ϕ. All the observables except the P2P phase are sensitive to the irregularity spectral index, whereas L_{Th} and ΔN influence all the observables.

3.5 Conclusions and Future Work

In this paper, we have presented a new numerical model for the electromagnetic propagation through the random ionospheric electron density fluctuations. The new model, SIGMA, is a split-step model comprised of multiple phase screens and forward propagation between the screens. The new model is entirely general, is applicable anywhere on the globe, and can be used to study scintillations for a wide variety of frequencies ranging from the low VHF (or high HF) through GHz. The salient new features of the model are how it handles the arbitrary 3D geometries at high latitudes, the extended distribution of irregularities along the field lines and the low elevation angle signal paths through the irregularities. The model can accept any 3D realization of the electron density fluctuations from both first principle numerical simulations as well as empirically based spectral models. Consequently, although in the current work, we have used a spectral model of electron density fluctuations that are assumed to be zero-mean stationary random processes, we intend to couple SIGMA with data assimilation techniques and tomography algorithms, and use their background densities in SIGMA. Examples of such algorithms and techniques include Ionospheric Data Assimilation Three-Dimensional (IDA3D) algorithm proposed by *Bust et al.* [2004] and Multi-Instrument Data Assimilation System (MIDAS) developed by *Spencer and Mitchell* [2007]. Additionally, it is possible to incorporate time variation of the background density, for example, in the presence of particle precipitation. An important advantage of SIGMA over other statistically-based scintillation simulation models is that with density structure realizations, we can achieve propagation simulations with significantly higher fidelity.

The overall long-term research objective is to combine the modeling results from SIGMA with observations of closely-clustered arrays of GNSS scintillation receivers at high latitudes.

The array of ground observations will allow us to completely determine (or at least highly constrain) the unknown parameters in the spectral model of the irregularity, the altitude, thickness and drift velocities of the irregularities. However, such a large parameter space can lead to many possible configurations of the spectrum and layer parameters. Thus, the sensitivity study carried out in this paper is designed to help us understand which parameters are the most sensitive (or have the most visibility) to the ground observations. From such a baseline case, we can then iterate on different model realizations until we achieve the best fit between the observations and model predictions. It should be noted that for as few as four scintillation receivers deployed over a baseline of a few kilometers, there are 6 independent measurements available at each time step (or averaging time). In addition to that, if a measurement of the overall "strength" of the scintillations is available, this is enough information to determine the irregularity spectral parameters, as well as the height and thickness of the layer, with the use of SIGMA.

Our follow-up paper will focus on comparing SIGMA simulations to high latitude GNSS observations, and achieve a better understanding of the underlying dynamics of the intermediate-scale irregularities producing the observations. In summary, we plan to solve an inverse problem by considering scintillation observations and using SIGMA to determine the best suited physical and propagation parameters for the irregularity generating these scintillations. We believe this approach will help us understand the polar and auroral irregularity physics.

Acknowledgments

We would like to thank the National Science Foundation for supporting this research under grants ANT-0839858, ATM-922979, PLR-1243398, ANT-0840650, PLR-1248087 and AGS-1311922. K. B. Deshpande is grateful to Dr. Sunanda Basu for her valuable suggestions on the irregularity sizes at different altitudes.

Chapter 4

Satellite-beacon Ionospheric-scintillation Global Model of the upper Atmosphere (SIGMA) II: Inverse modeling with high latitude observations to deduce irregularity physics

K. B. Deshpande,[1] G. S. Bust,[2] C. R. Clauer,[1] A. T. Weatherwax,[3].
Manuscript in preparation for *Journal of Geophysical Research (Space Physics)*.

[1] Bradley Department of Electrical and Computer Engineering, Virginia Tech, Blacksburg, Virginia, USA
[2]The Johns Hopkins University Applied Physics Laboratory, Laurel, Maryland, USA.
[3]Siena College, Department of Physics, Loudonville, NY, USA.

Abstract

In this paper, we characterize high latitude irregularities observed by Global Navigation Satellite System (GNSS) scintillation measurements during a geomagnetically active duration on 9 March 2012. For this purpose, along with the measurements, we are using the recently proposed three dimensional (3D) electromagnetic (EM) wave propagation model: "Satellite-beacon Ionospheric-scintillation Global Model of the upper Atmosphere" (SIGMA). The model is particularly applicable at high latitudes as it accounts for the complicated geometry of the magnetic field lines in these regions and is presented in an earlier paper. We are using inverse modeling technique to derive irregularity parameters by comparing the high rate (50 Hz) GNSS observations to the modeled outputs. The datasets we consider in this investigation are from

both the Southern and Northern high latitudes. We use auxiliary data in addition to the sensitivity study results from the earlier paper, to deduce some of the input parameters of SIGMA for a given GNSS observation. Finally, we implement an optimization technique to obtain the best-fit values of the rest of the unknowns. The input parameters of SIGMA thus derived represent the physical and propagation parameters related to the physics of the irregularity that produced those GNSS scintillations. Some of our findings from this investigation are: the spectral index for the event under consideration ranges from 2.4 to 4.2 and the background number density ranges from 0.8e12 to 2.5e12 el/m^3. The best fits we obtained from our inverse method mostly agree with the observations, but we also report some ambiguities. We need more auxiliary data in order to facilitate the possibility of accomplishing a unique solution to the inverse problem.

4.1 Introduction and Motivation

Ionospheric scintillations in Global Navigation Satellite System (GNSS) signals are rapid variations in their amplitude and phase resulting from electron density irregularities in the ionosphere. Scintillations are frequently observed in high latitude and equatorial regions [*Aarons*, 1982].

It has been shown that in the dayside auroral region, large-scale phase scintillations are observed more often than amplitude scintillations [*Aarons*, 1997; *Basu et al.*, 1998]. More recent observations reported by *Mitchell et al.* [2005] in the Northern high latitudes and by *Kinrade et al.* [2012] and *Deshpande et al.* [2012] in the Southern high latitudes also indicated a predominance of phase scintillations. Statistical results from the South Pole presented by *Kinrade et al.* [2013] emphasize the occurrence of Global Positioning System (GPS) phase scintillations coexisting with auroral emissions.

Our goal is to characterize the small and intermediate-scale high latitude irregularities

which are more likely the sources of these phase scintillations. We would also like to have a better understanding of the physics of these ionospheric structures. In the long run, this would enable us to understand the underlying mechanisms, magnetospheric-ionospheric coupling effects on the irregularity generation, and perhaps also identify the causes of prevalent phase scintillations at high latitudes. The characterization of irregularities can be achieved using the GNSS scintillation observations and observations from other ancillary instruments coupled with the physical and propagation parameters derived from our recently presented model: Satellite-beacon Ionospheric-scintillation Global Model of the upper Atmosphere (SIGMA) [*Deshpande et al.*, 2014]. The parameters derived from the auxiliary instruments and an inverse method can be used to extract the physics of the irregularity involved in the generation of those scintillations.

A few good examples of the inverse modeling technique can be found in the works of *Keskinen* [2006] and *Carrano et al.* [2012b], where they use the technique to infer turbulence parameters from intensity scintillation data from the low latitude regions. Although, the iterative parameter estimation technique presented by *Carrano et al.* [2012b] is similar to our inverse modeling methodology, the latitudes they consider, their underlying model and the free parameters they fit are different compared to ours. Moreover, we are utilizing at 50 Hz phase scintillation observations, whereas they worked with 10 Hz GPS carrier-to-noise measurements.

Additionally, low rate scintillation indices S4, σ_ϕ data have been used in interhemispheric study [*Prikryl et al.*, 2010, 2011, 2012]. But, according to our knowledge, the morphology and geographical distribution of small and intermediate scale irregularities at high latitudes hasn't been explored with high rate (typically 50 Hz) scintillation data, especially in conjunction with modeling. Therefore, this study is one of its kind.

The organization of this paper is as follows: we list and give details on the observations and the model we are using in this study in Section 4.2. In Section 4.3, we describe our inverse modeling analysis methodology. We present our results from inverse modeling and discuss them

in Section 4.4. Finally, we conclude our findings and discuss our future plans in Section 4.5.

4.2 Datasets and Model

4.2.1 GPS and Auxiliary Datasets

The week of 7 to 17 March 2012 was a duration of very active geomagnetic storms and substorms. We select 9 March 2012 dataset based on geomagnetic activity and also the availability of maximum auxiliary datasets. We are interested in studying the high latitude irregularity physics during storm conditions at different geographical location. For this paper, we focussed on at 6 different locations, 3 from each hemisphere. From Southern hemisphere, we have GPS data from receivers at McMurdo (MCM), South Pole (SPA) and Concordia (DMC0), and from Northern hemisphere, we have data from receivers at Ny-Ålesund (NY0), Tromsø and Resolute Bay (ResBay). The Canadian High Arctic Ionospheric Network (CHAIN) graciously provided the data for Resolute Bay [*Jayachandran et al.*, 2009]. We tried to obtain our observations from close-to-magnetically conjugate stations. We list the geographic and geomagnetic coordinates of these stations in Table 4.1.

A preliminary examination of low rate S4 and σ_ϕ data revealed the possible times and dates during the March 2012 week mentioned above. Results from a detailed search for observations from ancillary instruments such as the Super Dual Auroral Radar Network (SuperDARN), Incoherent Scatter Radar (ISR) compelled us to use 9 March 2012 dataset from 3 to 4 UT. Kp index was 6 during this time, and it was a beginning of a geomagnetic storm. Moreover, this time duration revealed $\geq$ 30 seconds long continuous periods of phase scintillations on most of the receivers. This enabled us to use SIGMA to model 30 second-long time series for the inverse modeling.

In this inverse modeling work, we are using 50 Hz high rate GPS scintillation data. We did

Table 4.1: Geographic and Geomagnetic coordinates of the locations under study.

Location	Symbol	Owner	Geographic (Latitude,Longitude)	Geomagnetic (Latitude,Longitude)
Resolute Bay	ResBay	CHAIN	(74.4°N,94.5°W)	(82.7°N,35°W)
Ny-Ålesund	NYA0	INGV	(78.9°N,11.9°E)	(76.4°N,109.4°E)
Tromsø	Tromsø	BATH	(69.3°N,19.1°E)	(66.7°N,102.1°E)
South Pole	SPA	BATH	(90°S,97.5°W)	(74.3°S,18.7°E)
McMurdo	MCM	BATH	(77.8°S,166.7°E)	(80°S,33.9°W)
Concordia	DMC0	INGV	(75.1°S,123.2°E)	(89°S,59.2°E)

not observe power fluctuation over the noise floor during our time of interest. This is consistent with the prevalence of phase scintillations observed at high latitudes as discussed in Section 4.1. Stacked plots of detrended and filtered GPS high rate phases at different locations from 3 to 4 UT on 9 March 2012 are shown in Figure 4.1. The stations are arranged from higher to lower magnetic latitude. We highlight the scintillation periods from which we have selected the data for inverse modeling with black rectangles. A scale on the hand right side of the plot represents 3 radians of phase. We did not observe any scintillations on Concordia during this period. This is an interesting finding to help put the dynamics of the ionospheric structure in context of the geomagnetic location. Thus, we still show it in this plot.

The auxiliary data for this work were obtained from Tromsø ISRs, the Defense Meteorological Satellite Program (DMSP) and Polar-orbiting Operational Environmental Satellite (POES) satellite data, and SuperDARN radars in both hemisphere. We use auroral oval predictions from Special Sensor Ultraviolet Spectrographic Imager (SSUSI) instrument on the DMSP satellites *http://ssusi.jhuapl.edu/* and OVATION Prime plots which use the POES data [*Newell et al.*, 2009; *Machol et al.*, 2012]. The details of how OVATION Prime plots are produced by the National Oceanic and Atmospheric Administration (NOAA) can be found at the National Geophysical Data Center (NGDC) website *http://www.ngdc.noaa.gov/stp/ovation_prime/*. We will refer to these data during the discussion of the results from individual inverse modeling problem in Section 4.4.

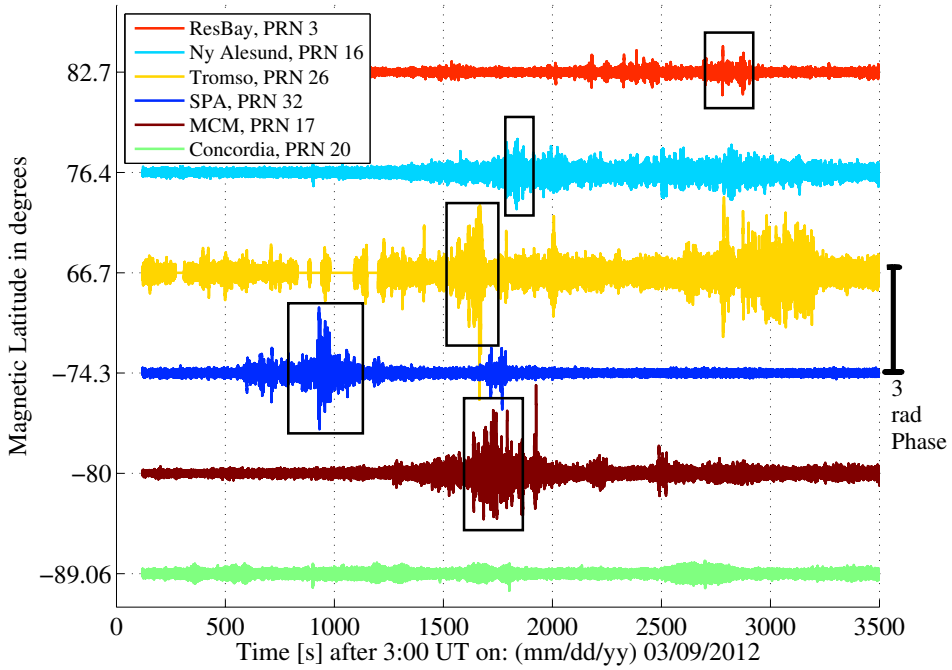

Figure 4.1: Stacked plots of phases in radians at 6 different locations.

4.2.2 SIGMA

SIGMA is a full three dimensional (3D) electromagnetic (EM) wave propagation model which we use to propagate a signal from a moving satellite to the ground through multiple phase screens. The details of SIGMA can be found in the paper by *Deshpande et al.* [2014]. Inside SIGMA, we first obtain a spatial electron number density distribution from a spectral model for high latitude irregularities, and then utilize a hybrid method that combines the multiple phase screen (MPS) technique with a split-step solution to the forward propagation equation (FPE) [*Rino*, 2010; *Rino and Carrano*, 2011], to propagate the signal to the ground.

SIGMA outputs GPS scintillation phase and power time series with 50 Hz sampling frequency. The high rate phase and power from SIGMA as well as the observations are subjected to detrending and filtering to eliminate any low frequency effects including the satellite motion. We are using the modeled phase from SIGMA for the inverse analysis described in the next section. When comparing an observed time series to the modeled time series, one needs to make

sure that the two time series are not out-of-phase to start with. This is difficult to determine. Therefore, we compare the power spectral density (PSD) of the SIGMA phase time series to the PSD of the observed phase time series.

We obtain the temporal PSD of the phase time series using Welch's method presented by *Welch* [1967]. At 50 Hz sampling rate, it takes a few hundred seconds for SIGMA to generate a time series as short as 30 seconds, which itself manifests in several hours of time for an optimization or uniform-grid simulation run. Thus, the length of the time series is taken to be 30 seconds. This short time length selection also worked positively in the search for a continuous scintillation observation of that length on all the receivers. e.g. Scintillations on NYA0 were not strong, so it was hard to find longer than 30 seconds time series. We divide the time series into 10 seconds segments and apply a rectangular window function. With Welch's method, before obtaining the PSD, these segments are averaged with a 50% overlap to reduce the noise in the spectra. Since, the phase time series is originally filtered with a 0.1 Hz high pass filter to eliminate low frequency effects as suggested by *Van Dierendonck et al.* [1993], the minimum frequency in the PSD is 0.1 Hz while the Nyquist frequency is 25 Hz. In this study, we use Hybrid spectral model of irregularities at high latitudes from *Costa and Kelley* [1977], the use of which for SIGMA is described in our earlier paper in this series [*Deshpande et al.*, 2014].

4.3 Method of Inverse Modeling

In this section, we describe the inversion technique we use to fit SIGMA output to the observations and obtain the optimal values of SIGMA input parameters for the best fit. As seen from Table 4.2, there are seven unknown input parameters for a given inverse modeling run, that is, for a given GPS observation dataset. These unknowns are found with two steps in the inverse modeling technique as described below.

Initially, for a given GNSS observation, we use the auxiliary data to find as many input

Table 4.2: SIGMA Input parameters. The respective steps of the inverse modeling which are used to obtain the input parameters are mentioned in brackets.

Irregularity	**Spectrum Parameters**
l_0	Outer scale (15 km)
$SpInd$	Spectral index (Step 2)
ΔN	RMS electron density fluctuation (Step 1 or 2)
AXR	Axial ratio (10)
Geographical	**Parameters**
I	Dip angle (Receiver Location)
LOS(Elv,Az)	LOS vector elevation and azimuth (Receiver & Satellite Location)
Propagation	**Parameters**
H_{iono}	Altitude (Step 1 or 2)
N_l	Number of layers (1)
L_{Th}	Thickness (10 km)
v_d	Drift velocity (Step 1 or 2)

parameters for SIGMA as we can. This is discussed in Section 4.3.1. To reduce the dimension of the design space further, we assume certain values for some of the input parameters, namely, the outer scale, axial ration, and thickness. Using a simulation over a uniform four-dimensional (4-D) grid presented in Section 4.3.2, we retrieve the remaining input parameters for the best fit of the modeled PSD to the observed PSD.

The turbulent strength defined by root mean square (RMS) of the electron number density fluctuations ΔN in el/m^3 and the thickness of the irregularity L_{Th} together may affect the overall shift of the PSD. The effective drift velocity v_d is expected to change the phase power content as a function of frequency. Finally, we expect $SpInd$ to change the shape of the PSD. Therefore, we try to optimize the SIGMA PSD to match the observed PSD, with ΔN (maintaining a constant L_{Th}), $SpInd$, and drift velocity magnitude and direction as the four free parameters.

For each observation, the geographical parameters, namely, dip angle and azimuth elevation can be obtained from the receiver and satellite locations. For this investigation, we assume weak

scattering, so that we do not need multiple layers.

4.3.1 Step 1: Use of Auxiliary Data

The background density ΔN, approximate drift velocity of the ionospheric structures and height H_{iono} of the irregularities can be estimated from ISRs. SuperDARN fitted velocity maps can be used to get a fairly good estimate of the drift velocities. The magnitude of the velocity can also be approximated from the PSD of the observed intensity. If the PSD of intensity shows a roll over at a frequency f_{roll}, an approximate magnitude of the drift velocity at altitude H_{iono} would be $f_{roll}\sqrt{\lambda H_{iono}}$, where λ is the wavelength of the GPS signal. The availability of DMSP and POES satellite passes over the regions of interest can confirm the possibility of energetic particle precipitation and can help with auroral oval boundary prediction. If there is precipitation, the ionospheric scintillations are more likely be from E region or 120 km. If the GPS scintillation events are more likely F region events such as polar cap patches from 350 km height and SuperDARN or ISR data are not available, tomography algorithms such as Ionospheric Data Assimilation Four-Dimensional (IDA4D) [*Bust et al.*, 2004] can be used to confirm the same. Although background densities from data assimilation techniques and tomography algorithms such as IDA4D and Multi-Instrument Data Assimilation System (MIDAS) [*Spencer and Mitchell*, 2007] can also be integrated in SIGMA, this will be left for future work.

If ΔN and v_d cannot be obtained from auxiliary data, we proceed to Step 2 of the method. However, due to absence of auxiliary observations, if we cannot estimate the height H_{iono} of the ionosphere with positive assurance, we implement the inverse modeling technique at both E and F region altitude.

Axial ratio is a parameter that defines the anisotropy of the rod-shaped irregularities. From the sensitivity study by *Deshpande et al.* [2014], we deduced that for axial ratios lower than 5, the two-dimensional (2-D) phase structures on ground look more isotropic, while for

values above 30, the coherence length along the z-axis becomes larger than the thickness of the layer (10 km). Thus, assuming we have rod shaped irregularities, we consider an axial ratio of 10 and irregularity thickness of 10 km for our simulation. We choose a higher value of outer scale l_0 of 15 km based on the findings of *Rino* [1979], where he found no evidences of a finite l_0 cutoff.

4.3.2 Step 2: Uniform-grid SIGMA Simulation or DIRECT Optimization

From step 1, we obtain an estimate of three of the seven unknown SIGMA input parameters, namely, H_{iono}, v_d ($|v_d|$, $\angle v_d$) and ΔN. As mentioned earlier, if H_{iono} is not known, the following analysis is simply run at two different heights of 120 km and 350 km. In this section, we describe the method to obtain the best-fit values for the four design variables stated earlier. In case of 3 or more design variables, the inverse modeling problem is a huge multidimensional problem and will require more sophisticated computation resources if the problem is to be solved using optimization algorithms. In this paper, we solve the problem with 4 design variables using a simulation performed over a uniformly sampled 4-D grid. However, we also present an optimization algorithm that can be used effectively for a multidimensional problem.

We incorporate a least-squares or Chi-square fitting test [*Chernoff and Lehmann*, 1954; *Press et al.*, 1992] to obtain χ^2. We minimize this metric using a uniform-grid SIGMA simulation. We fit the PSD of the model to the data in the log-log domain. χ^2 is the least-squared fit value and is given by

$$\chi^2 = \frac{1}{\sigma_y^2} \sum_{i=1}^{N} (\log_{10} Y_i - \log_{10} X_i)^2 \tag{4.1}$$

where Y_is are N number of points on the PSD of the observed phase, X_is are the points on PSD of the SIGMA phase and σ_y^2 is the variance on the observed PSD after removal of any trend in the PSD. It represents a constant measurement error on the data. We consider a constant error in the χ^2 minimization since the variance on each Y_i point and thus the uncertainties associated

with the set of GPS measurements is not known in advance.

For a good fit, $\chi^2 \approx (N - M)$, where $N - M$ is the number of degrees of freedom. M are the total number of design variables to be fitted. Furthermore, the PSD values to fit are between f_{min} and f_{max}, where $f_{min} = 0.2$ Hz is the minimum frequency after the filtering of the phase time series and finding the PSD using the Welch's method. We purposefully consider a higher frequency than the filter frequency of 0.1 Hz to avoid fitting any filter artifacts. f_{max} is the maximum frequency before the noise floor starts. We found it to be around 8.5 Hz. In the current study, N is equal to 83 and M is equal to 4. We added another constraint while minimizing this χ^2 value. For all the cases, phase scintillations were predominant. Thus, while fitting the phase SIGMA PSD to the observed phase PSD, we selected only those cases for which the peak to peak value of the intensity time series was within 3 times of that of the observed value.

We run SIGMA over uniformly sampled grid in the 4-D parametric space. This we refer to as "uniform-grid SIGMA simulation". The range of $SpInd$ is from 0.6 to 6, while that of ΔN is 1.0e11 to 2.5e12 el/m^3. The discretization used in the simulation results in a resolution of $\delta SpInd = 0.6$ for $SpInd$ and $\delta\Delta N \approx$ 2e11 el/m^3 for ΔN. We do not expect to see any sharp gradients in the parametric space, but since the function is non-linear there always will be an uncertainly associated with it. We find the global minimum value χ^2_{min}. Drift velocity magnitude and direction ranges are chosen to vary $\pm$400 m/s and $\pm30^\circ$ of those obtained from SuperDARN mapped velocities.

With an assumption that the measurement errors in the χ^2 minimization are normally distributed, we quantify the errors in the parameter estimation as described by *Press et al.* [1992]. The global minimum χ^2_{min} is presented in the contour plots along with the confidence limits of 68.3% and 90% for that particular value. The confidence limits of 68.3% and 90% represent 1 and 2 standard deviation spread, respectively. We also specify the median value inside the 68.3% confidence contour.

The multidimensional optimization method we intend to use for problems with 3 or more design variables is called DIRECT optimization method [*Jones et al.*, 1993; *Gablonsky and Kelley*, 2001]. This method, unlike other optimization methods such as the simplex method by *Nelder and Mead* [1965], is designed to completely explore the parametric space, even after more than one local minima have been identified. This method has been proven to be a useful method to find a global minimum for cases, such as the present one, where the function is non-linear, function gradients are difficult to calculate, and there could be several minima in the multi-dimensional parametric space. In this work, the choice of uniform-grid SIGMA simulation over DIRECT optimization is motivated by computational expediency with a simple use of code parallelization. However, we again stress that using DIRECT optimization would be more suitable and efficient for inverse problems with higher dimensional design space.

4.4 Results and Discussion

In this section, we describe the results of inverse modeling for one location in detail and briefly discuss the results at the rest of the locations.

4.4.1 McMurdo Results

The predictions of auroral oval boundaries from OVATION prime for both the hemispheres are shown in Figure 4.2. The station positions are highlighted on the plots. From an inspection of the auroral oval boundaries in the Southern hemisphere, it is apparent that McMurdo was not inside the auroral oval. In order to determine the altitude we used IDA4D algorithm. The result of an IDA4D run for the case of McMurdo is represented as a polar plot in Figure 4.3. The plot does not show any indication of F region patches or F region precipitation. This suggests that the scintillation could most likely be from irregularities at 120 km height. In any case, we solve the inverse problem at both E region and F region heights with H_{iono} equal to 120 km and 350 km, respectively.

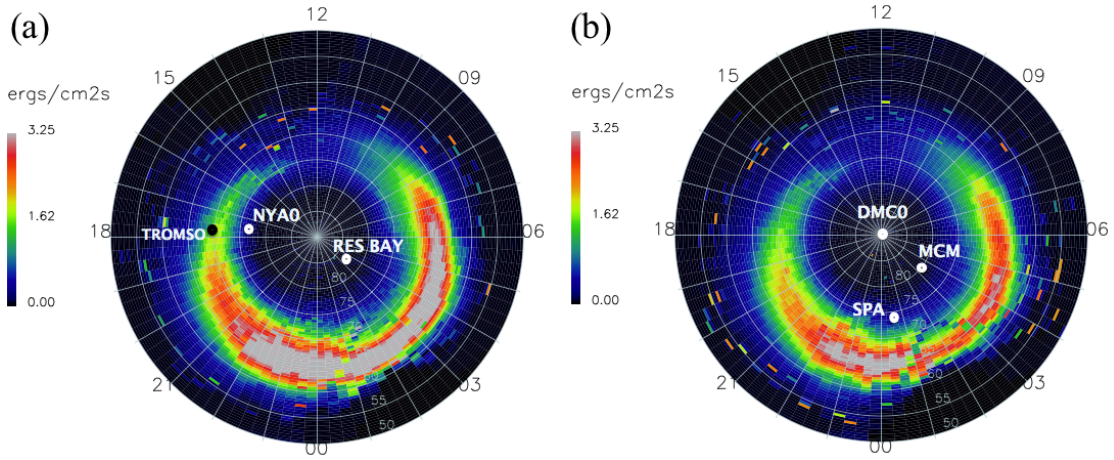

Figure 4.2: Forecast of (a) Northern auroral oval at 3:30 UT and (b) Southern auroral oval at 3:15 UT on 9 March 2012 (obtained from the National Geophysical Data Center).

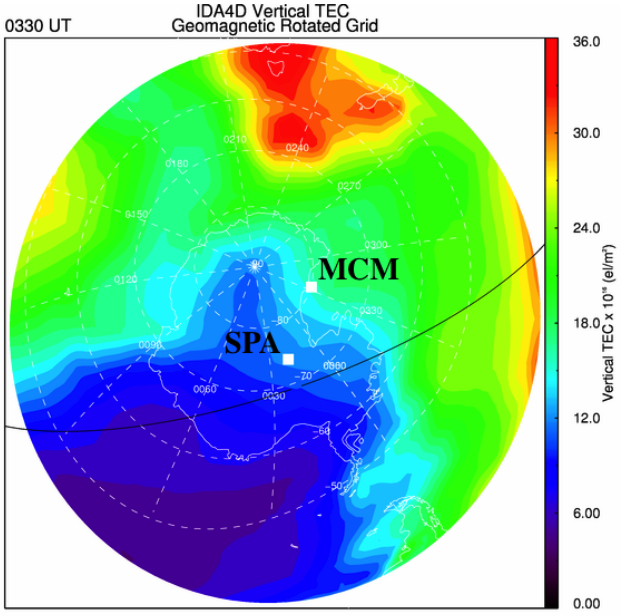

Figure 4.3: IDA4D polar plot result over McMurdo at 3:30 UT on 9 March 2012.

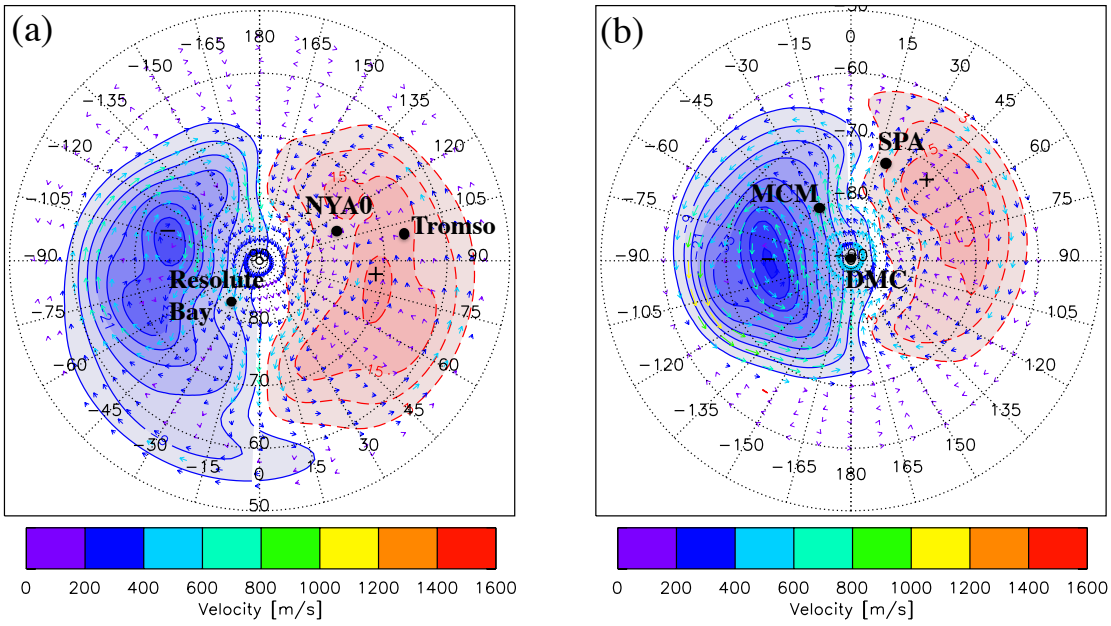

Figure 4.4: Convection velocity maps derived from SuperDARN data in (a) Northern high latitude region at 3:30 UT and (b) Southern high latitude region at 3:15 UT on 9 March 2012.

Figure 4.4 shows the SuperDARN convection velocity maps found using the technique described by *Ruohoniemi and Baker* [1998]. As seen in Figure 4.5, the velocities at McMurdo are around 600 m/s at an azimuth of -110°. The azimuth is found from the geomagnetic west direction. We note that these are predictions from the sparse E × B measurements from just two Southern SuperDARN radars. However, as explained in Section 4.3.1, the velocity magnitude can be estimated from the observed intensity PSD at MCM. At 350 km it is 800 m/s, while at 120 km it is 470 m/s.

In Figure 4.6, we present the contours of χ^2 with respect to ΔN and $SpInd$ at 120 km and 350 km heights and at the optimum velocity value. In other words, we obtain a 2-D slice of χ^2 at the optimum values of the magnitude and direction of v_d. In all the contour plots, we show the positions of χ^2_{min}, the median in the unit standard deviation spread. The two confidence levels are explained in Section 4.3.2 and are indicated by dashed lines in this figure. For the 120 km case, we state that there is a 68.3% chance that the true values of ΔN and $SpInd$ will fall within the region highlighted by 68.3% confidence level contour. It can also been seen

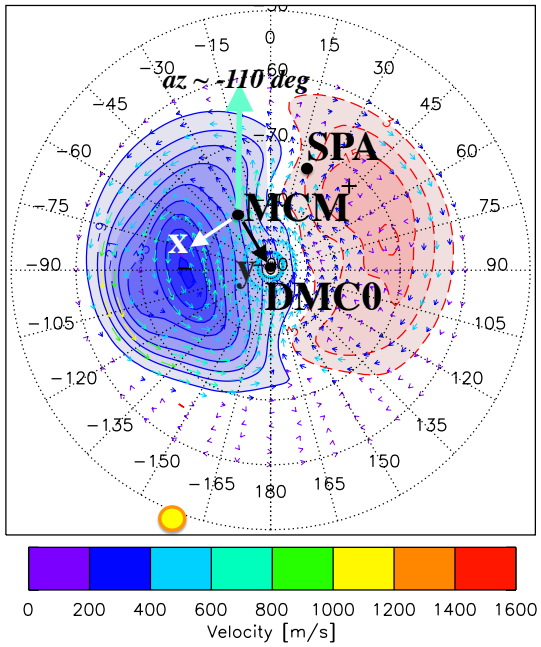

Figure 4.5: Figure 4.4(b) replotted at 3:28 UT in the topocentric coordinate system at McMurdo. The yellow circle between -150° to -165° depict the location of the Sun or the magnetic local noon in Corrected Geomagnetic (CGM) coordinates.

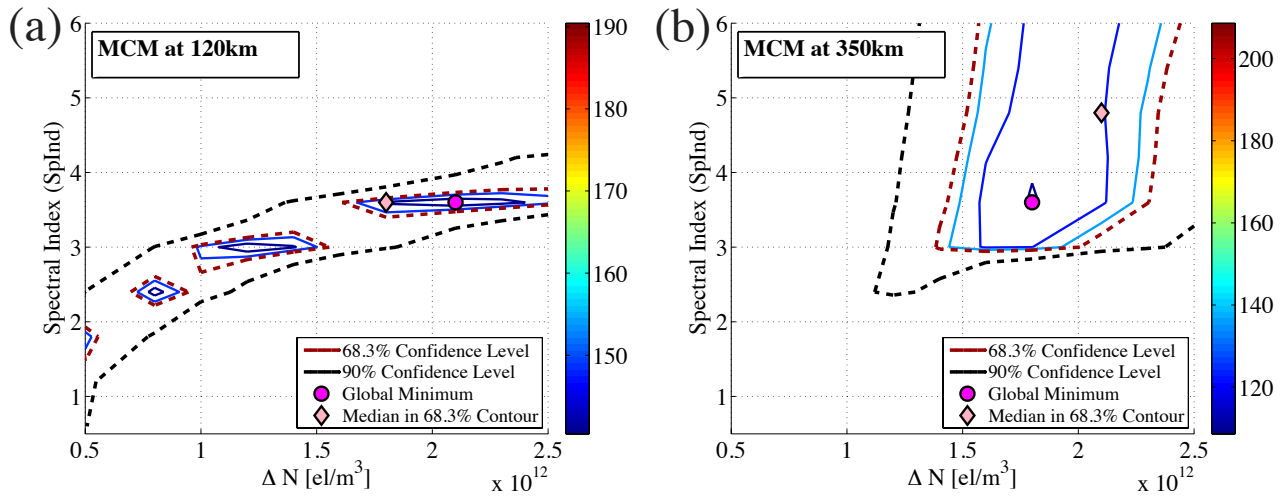

Figure 4.6: McMurdo case χ^2 contour plots showing different confidence levels at (a) 120 km and (b) 350 km.

that the 90% confidence level covers almost $1/3^{\text{rd}}$ region of the parametric space. Similarly, for 350 km case, the 90% confidence level covers almost the whole region. It should be noted that this solution is valid for a set of $_0$, L_{Th} and AXR values. If we had close-to-real values of these parameters from other sources, it would have been possible to obtain a better estimate of the free parameters. However, we definitely understand that, for example, for the case of 120 km height, the region $\Delta N > 1e12$ el/m^3 and $SpInd < 1.5$ does not have the optimum solution.

We obtain the free parameter values at the global minimum and plot the model fit to the data in both the frequency and time domains. These are shown in Figure 4.7, where we compare the best fit SIGMA PSD against the data PSD, and the best fit SIGMA time series against the data time series at 120 km and 350 km, respectively. The optimum parameter values for the best fit for all the cases are given in Table 4.3. The best fit model PSDs for 120 km and 350 km indeed appear to follow the data PSD plot. A closer examination of the PSDs and the χ^2 values reveals that the modeled PSD at 120 km is a better fit to the data compared with the 350 km case.

In order to test whether the statistical distributions of the best fit PSD values at 120 km match the PSD values of MCM observation, we looked at the probability density functions (PDFs) as shown in the histograms in Figure 4.8. The densities in the bar graph are computed such that the area under the curve for each bar graph is unity. In other words, if the frequency or the number of occurrences of PSD values of MCM data for i$^{\text{th}}$ bin with width w_i dB is F_i, then the density is F_i/A, where $A = \sum_i w_i F_i$. The bin sizes are computed using Scott's rule [*Scott*, 1979]. As seen from the comparison, the observed and modeled data have a comparable distribution.

Thus, with the available auxiliary data and these modeling results, we conclude that the source GPS scintillations observed at McMurdo is an irregularity at 120 km altitude. It should be noted that if we try to fit the modeled time series to the observations instead of the PSD, we would need to consider an extra free parameter or unknown, that is, the time offset between

the modeled and observed time series.

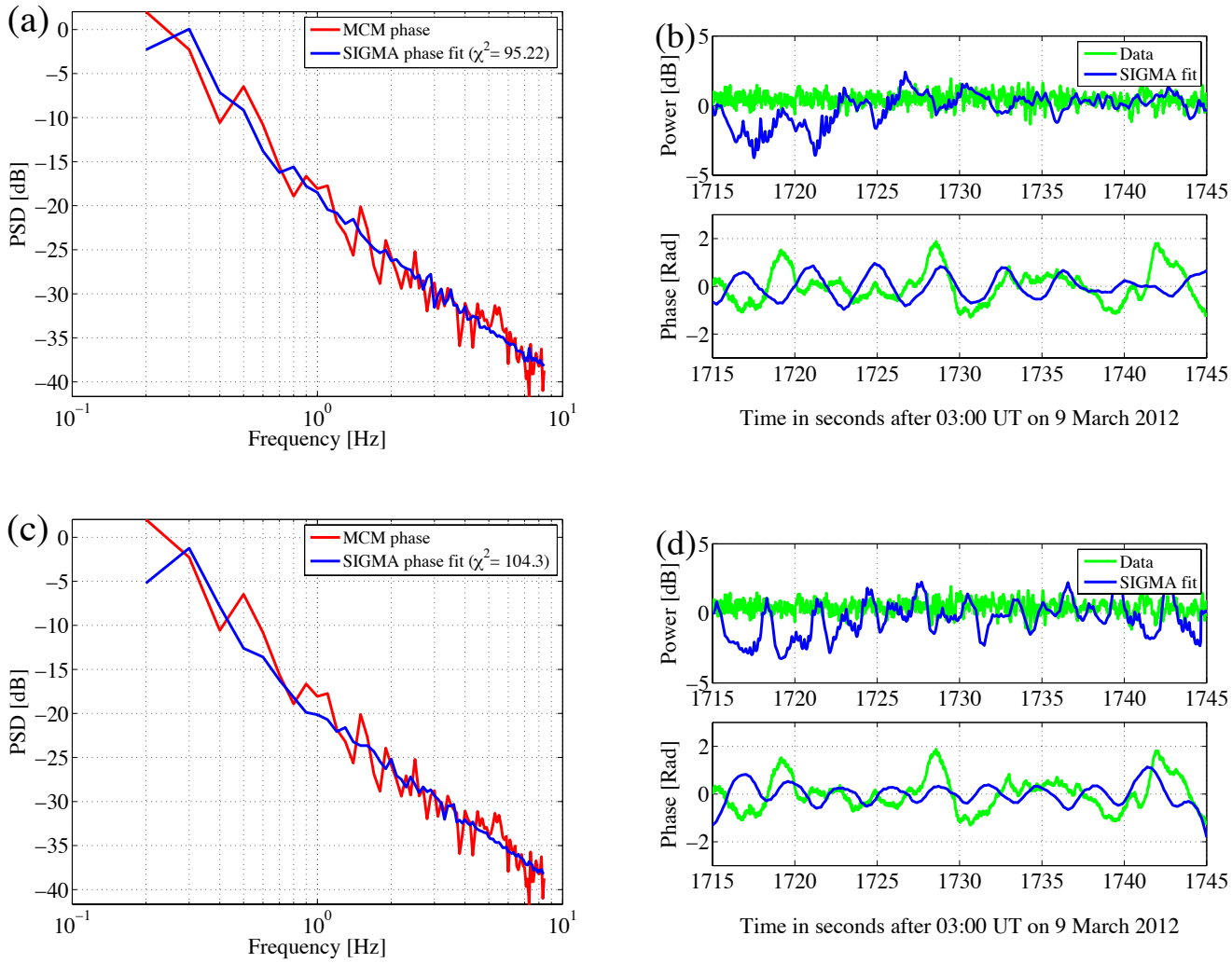

Figure 4.7: (a) and (c): PSD, and (b) and (d): time series of the best fits for 120 km (upper panel) and 350 km (lower panel) heights at McMurdo.

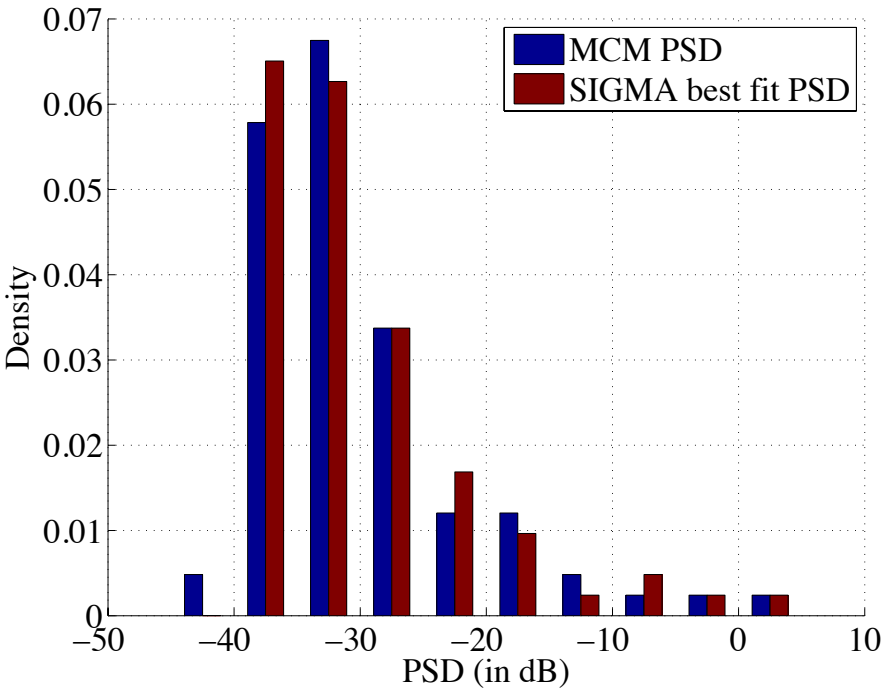

Figure 4.8: Comparisons of histograms depicting the PDFs of the MCM PSD and the best fits at 120 km. The density on the y-axis is normalized such that the area under the curve of each bar graph is unity.

Table 4.3: SIGMA parameter values for each inverse modeling case.

SIGMA Parameters	l_0 (km)	$SpInd$	ΔN (el/m^3)	AXR	L_{Th} (km)	$\|v_d\|$ (m/s)	$\angle v_d$ (degree)	χ^2
ResBay (at 120 km)	15	2.4	0.9e12	10	10	300	165	187
ResBay (at 350 km)	15	3.6	0.8e12	10	10	700	165	140
NYA0 (at 120 km)	15	3.0	1.0e12	10	10	450	-50	130
NYA0 (at 350 km)	15	2.4	1.0e12	10	10	400	-50	190
Tromsø (at 120 km)	15	4.2	2.3e12	10	10	500	150	144
Tromsø (at 350 km)	15	4.2	2.3e12	10	10	500	150	147
SPA (at 120 km)	15	2.4	1.0e12	10	10	400	-130	115
SPA (at 350 km)	15	3.6	2.5e12	10	10	700	-110	104
MCM (at 120 km)	15	3.6	2.1e12	10	10	600	-110	95
MCM (at 350 km)	15	3.6	1.8e12	10	10	600	-100	104

4.4.2 Interpretation of Auxiliary Data for Remaining Stations

In deciding the height of the ionosphere for inverse modeling with South Pole data, we wanted to assess whether it is under the auroral oval during the time of interest. Figure 4.2 (b) shows that South Pole is just inside the polar cap region. We also refer to the energetic particle precipitation data measured from the instrument SSUSI onboard the DMSP F 18 satellite during the time 3:15 to 3:30 UT plotted on the Antarctic map in Figure 4.9 (a). Although, South Pole is not on the DMSP satellite path, it certainly is within $\approx 5^\circ$ latitude from the path, and there appears to be high precipitation close to South Pole. Moreover, the keogram of imaging riometer at South Pole in Figure 4.9 (b) shows a definite absorption around 3:10 to 3:20 UT. These evidences indicate that South Pole was inside the auroral oval or on its boundary which leads us to consider $H_{iono} = 120$ km. The drift velocity at South Pole was estimated to be 400 m/s at an azimuth of -110° from the plot in Figure 4.4 (b).

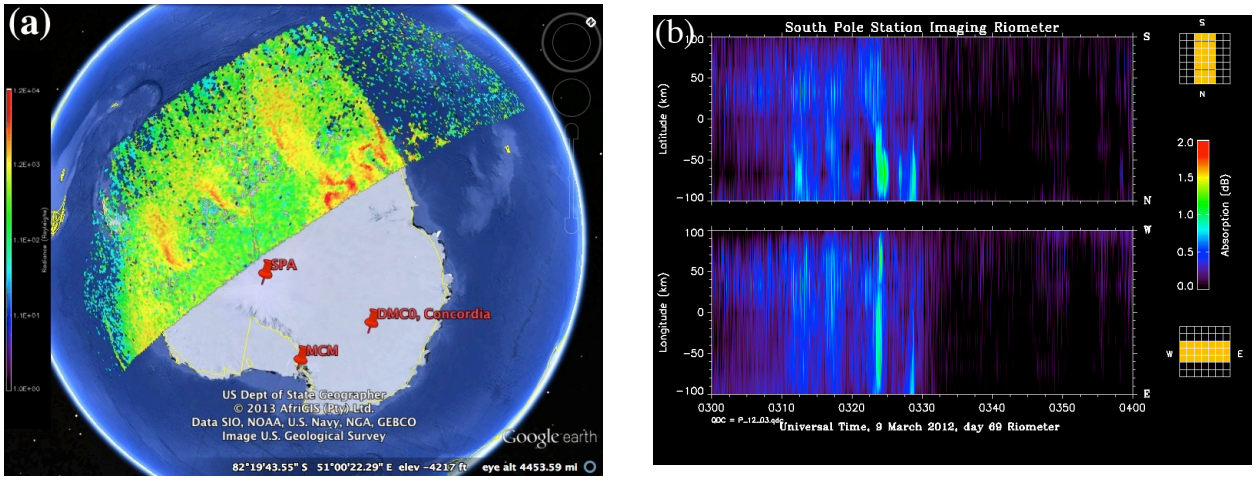

Figure 4.9: (a) Energetic particle precipitation over Antarctica from SSUSI instrument on the DMSP satellites and (b) Imaging riometer data at the South Pole displaying absorption around 3:15 UT, which most likely is due to precipitation.

From Figure 4.2 (a), Tromsø clearly seems to be under the auroral oval. Consequently, we consider the ionospheric height of 120 km. The minimum background density variation over Tromsø was found to be 1e12 from ISR data. For both SPA and Tromsø, however, we perform

the SIGMA inverse modeling at both E region and F region heights. Similar to South Pole, the velocity at Tromsø was deduced to $\approx$ 400 m/s at an azimuth of 180°.

From Figure 4.2 (a) Resolute Bay and Ny-Ålesund appear under the polar cap region. Thus, similar to McMurdo, we run the simulation at two different heights. The estimated velocities at these two regions from SuperDARN plot in Figure 4.4 (a) are close to 500 m/s and 200 m/s, respectively. The azimuths are 135° and -30°, respectively.

4.4.3 Discussion of Inverse Modeling Results

We found that the PSD of the best fit agreed with the observed PSD well in case of Resolute Bay at 350 km and Ny-Ålesund at 120 km as shown in Figures 4.10(a) and (c). Disregarding the time offset, the features of the best fit time series in Figures 4.10(b) and (d) appear to be more consistent with the observations in case of Resolute Bay as compared to Ny-Ålesund. The best results obtained for Tromsø (Figures 4.10(e) and (f)) and SPA (Figures 4.10(g) and (h)) were at 120 km.

From this work, our principal findings are as follows:

- At all the considered high latitude stations, we observed phase scintillations predominantly. The power shows some variations but it was below the noise level of ±3 dB.
- We report large ambiguity surfaces in the parametric space of ΔN and $SpInd$. This is mainly due to the uncertainty in the rest of the input parameters. We need more auxiliary data to eliminate these ambiguities.
- The spectral index of the phase scintillations derived from inverse modeling varies between 2.4 to 4.2 for different receivers and heights.
- ΔN for the irregularities ranges from 0.8e12 to 2.5e12 el/m^3. Thus, with 10 km thickness, the turbulence strength in TEC ranges from 0.8 TECU to 2.5 TECU.

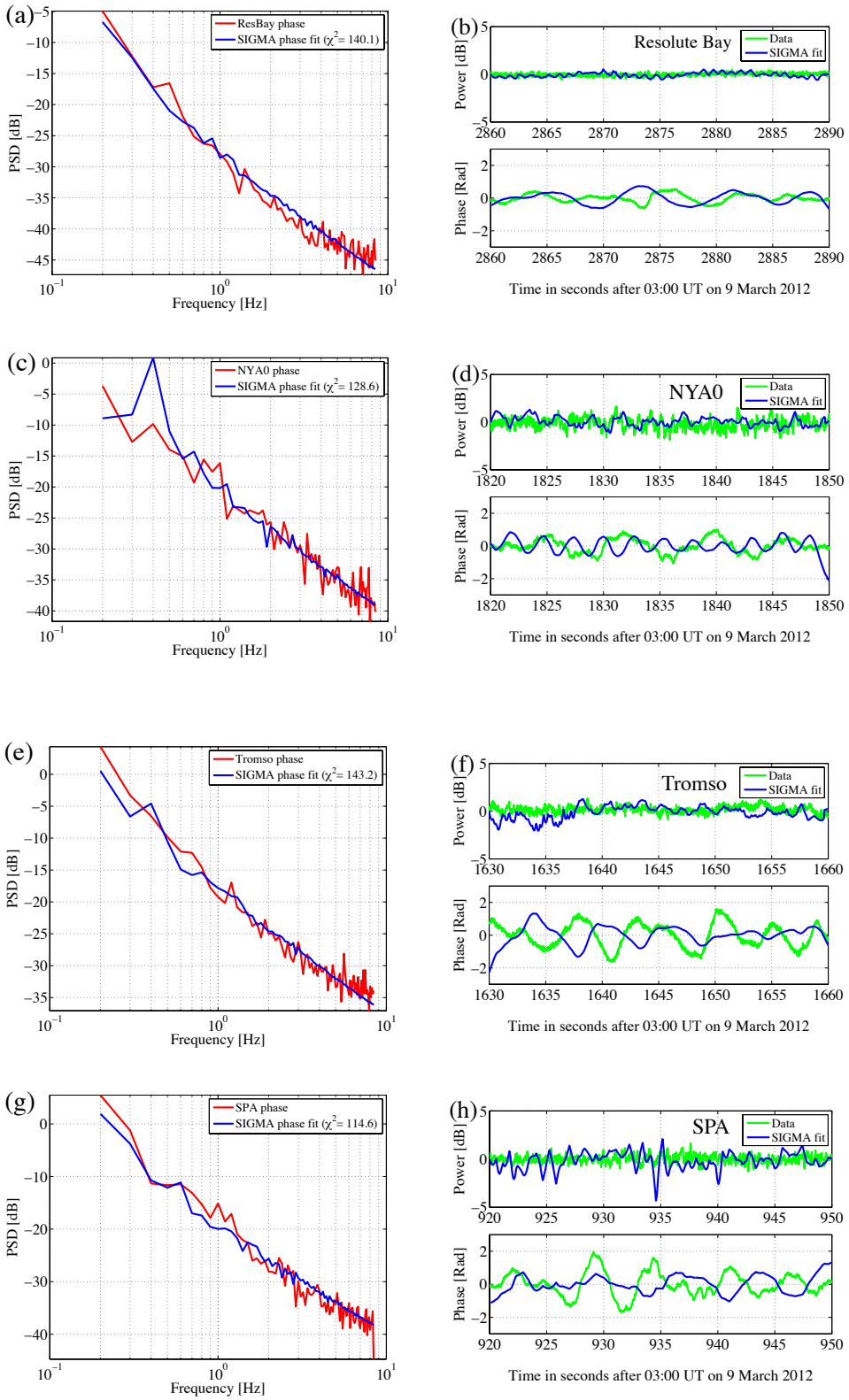

Figure 4.10: PSD (a,c,e,g) and time series (b,d,f,h) of the best fits for Resolute Bay (350 km), Ny-Ålesund (120 km), Tromsø (120 km), and SPA (120 km).

- Velocity estimates by SuperDARN are insufficient for the study of intermediate scale irregularities. Spaced receivers can provide accurate measurements of the drifts.
- The SIGMA PSDs for the best fit found by the inverse method agree well with the observed PSDs except for some cases.

As predicted by *Keskinen et al.* [1988], a Kelvin-Helmholtz instability at high latitudes may result in a spectral index of 1.8 ± 0.3 to 5.4 ± 0.4 depending on whether there are collisions. The spectral index values we found from the inverse modeling lie between this range. A few discrepancies in finding the best fit may be arising because of lack of information about the measurement errors. For higher fidelity, we require better estimate of measurement errors. The disagreement between the best fit SIGMA PSD and observed PSD could occur because of the following two possibilities. First, there is insufficient information to find close-to-real values of some inputs from auxiliary data. Second, the underlying spectral model with a single slope power law is inadequate to describe the physics of the irregularities involved in those observations.

4.5 Conclusion and Future Work

For the first time, we are using an inverse modeling technique to derive irregularity parameters by comparing the high rate GPS interhemispheric observations to the modeled SIGMA outputs. According to our knowledge, high rate GPS data have never been involved in high latitude interhemispheric studies, especially along with a model comparison. In this work, we used the available auxiliary data to deduce some of the input parameters of SIGMA for a given GNSS observation. Finally, for each observation, we obtained the optimal values of the remaining unknowns. The SIGMA input parameters thus derived represent the physical and propagation parameters related to the physics of the irregularity that produced those GNSS scintillations.

The technique we are using for inverse modeling is still under experimental consideration. For this study, we are simply optimizing four parameters out of the seven unknown parameters. From the current investigation, we deduced that the spectral index is between 2.4 to 4.2. With 10 km irregularity thickness, the turbulence strength in TEC ranges from 0.8 TECU to 2.5 TECU. The best fits we obtained from our inverse method mostly agree with the observations, but we also report some ambiguities. We need more auxiliary data in order to facilitate the possibility of accomplishing a unique solution to the inverse problem. For higher accuracy, we also need to obtain better estimates of measurement errors. This technique can be refined by implementing our recommendations from this study. We believe that such an upgraded inverse modeling technique will be very instrumental in routinely deriving the physics of the ionospheric irregularities from GNSS observations.

Acknowledgments

We would like to thank the National Science Foundation for supporting this research under grants ANT-0839858, ATM-922979, PLR-1243398, ANT-0840650, PLR-1248087 and AGS-1311922. We are grateful to Dr. Cathryn Mitchell and Dr. Joe Kinrade of University of Bath, UK for sharing the South Pole, McMurdo and Tromsø GPS data with us. We are also thankful to Dr. Luca Spogli of Upper Atmosphere Physics Istituto Nazionale di Geofisica e Vulcanologia (INGV) for sharing the Ny-Ålesund and Concordia GPS data with us. Kshitija would like to thank Dr. Charles Carrano for his valuable suggestions. Infrastructure funding for CHAIN is provided by the Canada Foundation for Innovation and the New Brunswick Innovation Foundation. CHAIN operation is conducted in collaboration with the Canadian Space Agency. Authors thank the SuperDARN team for the data, online tools to plot the data and answering some of our questions. Kshitija would like to thank Nathaniel Frissell of SuperDARN for helping with interpretation of data.

Chapter 5

Autonomous Adaptive Low-Power Instrument Platform (AAL-PIP)

5.1 AAL-PIP Project Description

The Magnetophere - Ionosphere Science Team (MIST) at Space@VT is leading a project of deployment of Autonomous Adaptive Low-Power Instrument Platform (AAL-PIP) in Antarctica. Each system has three instruments: a fluxgate magnetometer, a search coil magnetometer and a custom made dual frequency Global Positioning System (GPS) receiver. A magnetometer measures Earth's magnetic field which changes in strength and / or direction because of the disturbances on the Sun such as a solar flare, a coronal mass ejection, solar storm, solar wind or simply varying solar magnetic field. A GPS receiver records scintillation measurements: the GPS signal fades and scintillates because of the free electrons and ions in the ionosphere, the same way a star's light twinkles due to the Earth's atmosphere. This project is funded by the National Science Foundation (NSF) and has a number of groups, scientists, engineers and students involved from many institutes namely, Virginia Tech, Atmospheric and Space Technology Research Associates (ASTRA) at Boulder, University of Texas at Austin, University of Michigan at Ann Arbor, University of New Hampshire, Miami University at Oxford and Coherent Navigation.

The goal of this project is to understand the interaction of space plasma with the Earth's magnetosphere and ionosphere and thus to predict the properties of the complex solar-terrestrial

environment (space weather) by establishing a chain of six of these autonomous platforms along the 40 degree magnetic meridian in the southern polar region. This chain will be conjugate to the chain of magnetometers on the west coast of Greenland along the 40 degree magnetic meridian. This will enable inter hemispheric conjugate measurements. The deployment is performed by a PENGUIn (Polar Experiment Network for Geospace Upper-atmosphere Investigations) team. This array of Antarctic stations will boast a handful of cutting-edge technological advances designed to optimize data collection and power management for a year-round sustained operation. As described by *Musko et al.* [2009], the main part of the original system development was to build a low-power magnetometer (LPM) platform specifically designed to operate unattended for at least three years in remote Antarctic regions. The platform is now upgraded to collect search-coil and GPS data along with LPM, provide unattended operation for at least three years and operate at any location of the Antarctic plateau (at temperatures down to -80° Celsius). The systems are also designed to support near real-time data retrieval via satellite communications. An AAL-PIP utilizes solar power as its only energy source and stores power in sealed lead-acid batteries for winter operation. In a super-insulated electronics box, the temperature is maintained at -28° Celsius throughout the winter. Heating comes from the electronics of GPS receiver and Iridium radio receivers etc. *Clauer et al.* [2014] describe the AAL-PIP instrumentation in greater detail.

Each AAL-PIP consists of a solar power based power system with six 40 W solar panels. A set of 16 lead-acid batteries is used to store the power from solar panels for the low-power winter operation. The electronics box houses electronics for fluxgate magnetometer sensor, search coil magnetometer sensor, High Frequency (HF) radio and a single board controller along with Connected Autonomous Space Environment Sensor (CASES) receiver. The components of each AAL-PIP system are illustrated in Figure 5.1.

As a part of this project, a total of six AAL-PIP systems will be deployed on the Eastern Antarctic plateau along the 40 degree magnetic meridian, out of which, by 2014, four systems

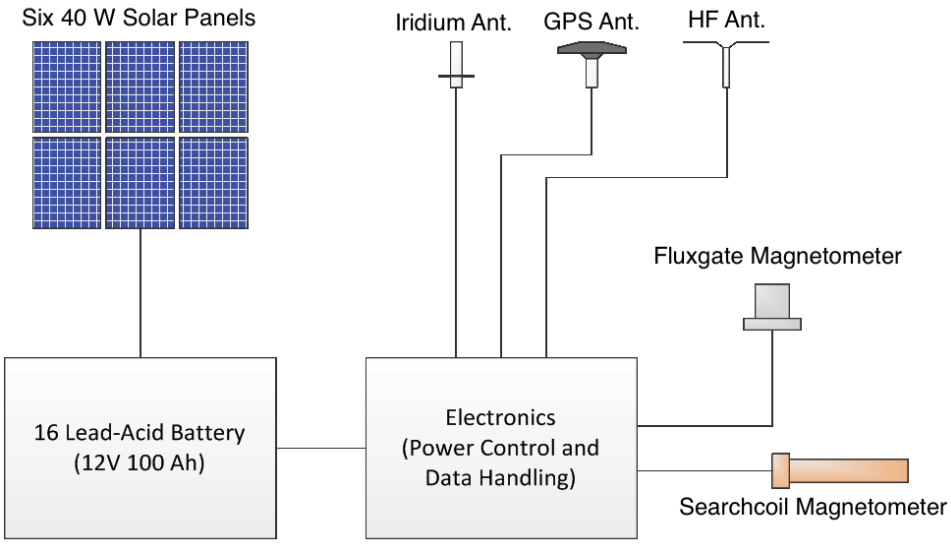

Figure 5.1: Block diagram representing an AAL-PIP.

have been installed. The locations of the AAL-PIP (PG) systems along with the locations of other stations in Antarctica as well as the conjugate Greenland stations are illustrated in Figure 5.2. PG1 has an older generation AAL-PIP (System 1) without search coil, GPS and HF. It was deployed in 2008. The latest generation AAL-PIP Systems 4 and 5 are installed at PG2 and PG3 in December 2012 and January 2013, respectively. System 6 is deployed at PG4 in January 2014. Operation status of AAL-PIP from 2008 to 2014 is illustrated in Figure 5.3. The author was a part of the field team that deployed System 4 at South Pole in December 2010 for a year for testing purposes.

5.2 Antarctica Expedition 2010

I was a part of an expedition team deployed to Antarctica in December 2010 for installation of AAL-PIP systems. It was an exciting experience and a wonderful field learning opportunity. The snippets of a daily installation activity log book during this trip are described below. The field team consisted of Dr. Bob Clauer, Dr. Hyomin Kim, Joseph Macon and Kshitija Deshpande.

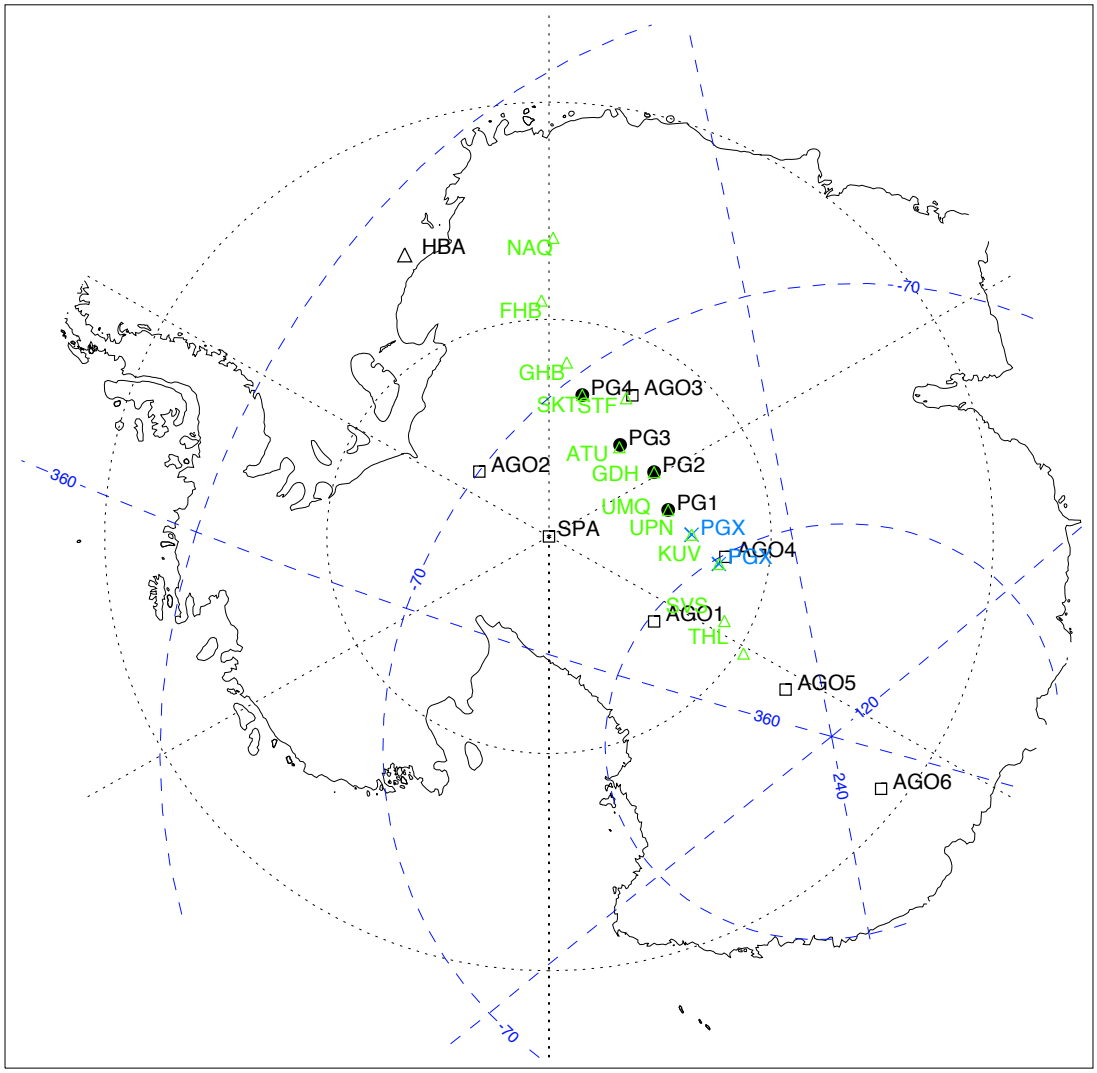

Figure 5.2: Map of AAL-PIP stations (PG) along with AGO stations and locations of conjugate Greenland stations (colored green). (Courtsey: Dr. Hyomin Kim)

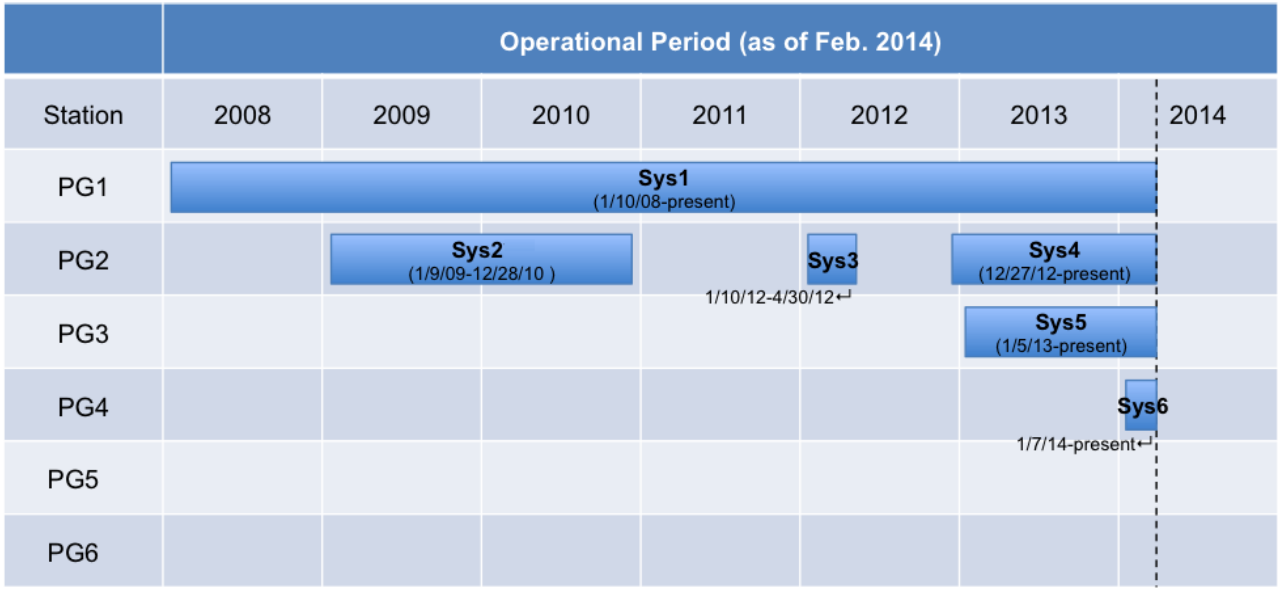

Figure 5.3: Operation status of AAL-PIP from 2008 to 2014 (Courtsey: Dr. Hyomin Kim).

Day 0: December 27, 2010. Today, we got the System 4 Cargo moved to a site in the Cusp Antenna field near the ARO building closer to the South Pole station.

Day 1: December 28, 2010. We started at around 8.45 am and got the tower ready by 11:30 am. From 1.00 pm to 4.00 pm, we received help from two General Assistants (GAs). We got the tower up with the solar panels attached at the bottom of the tower, electronics box and battery box installed (with batteries and battery connections done) in the pit. We then had to stop the work as the battery for the drill was drained out and our snowmobile quit without any warning.

Day 2: December 29, 2010. We started to work on the system around 9.30 am. The wiring of cables took a little extra time. The solar panels were not yet at the top of the tower and we needed to be cautious of not entangling the cables. By 3.30 pm, we had all the connections done including the Iridium, GPS antennas and the fluxgate. We got the solar panels wrenched up (Figure 5.4). Search coil was still to be installed.

Day 3: December 30, 2010. The first thing we did in the morning was to reconnect the

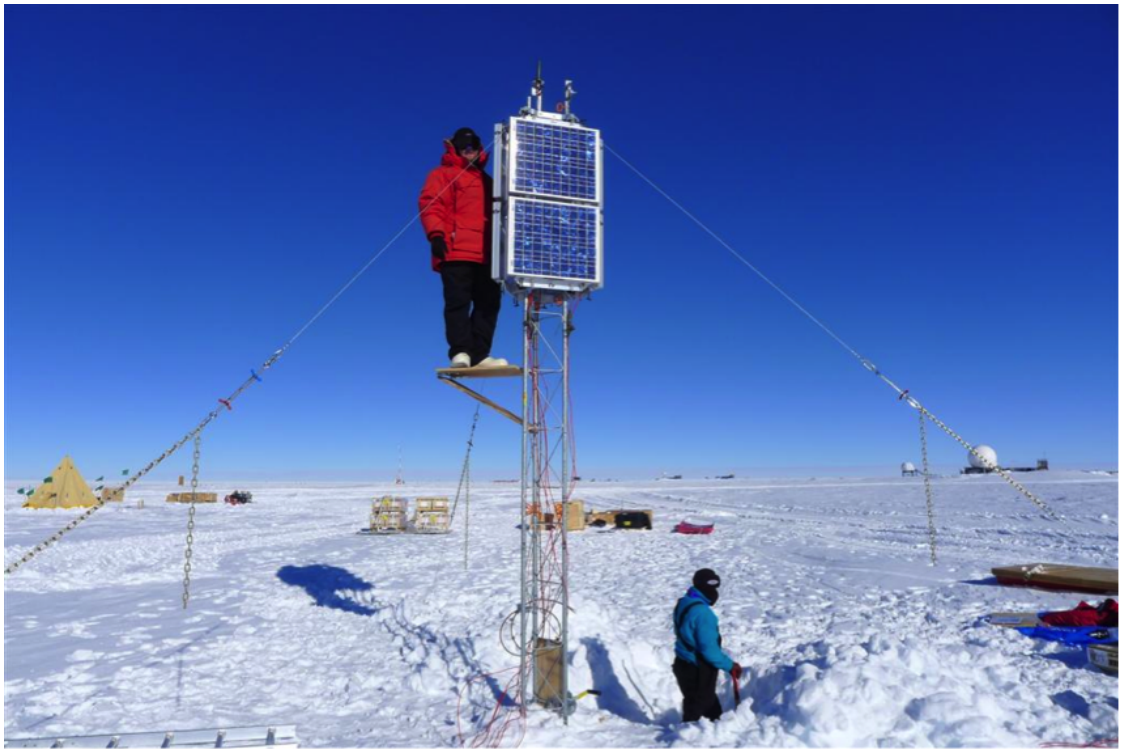

Figure 5.4: AAL-PIP solar panel tower. Joseph is securing the panels at the top of the tower and Dr. Bob Clauer is working in the electronics box pit.

System 3 fluxgate cable at the instrument and electronics box. For this, the system was shut down at 9.05 am. We also lowered the GPS antenna height to about 3 ft. It is still about 100 ft away. We turned the system back on at 9.50 am.

Challenges: The GPS connector is too tight at the antenna. We had to give up undoing the cable before we could twist the tower and reduce the length of the antenna. Fortunately, there was a lot of slack at the GPS cable. For the cable not to get twisted when we turn the GPS antenna tower section, we had to first twist the cable in the other direction.

Suggestion: It will be nice to have a small tool box with essential tools such as a wrench to loosen this cable, in the battery and electronics box pit.

After lunch, we set up the search coil magnetometer and finished the trench for GPS cable. Pictures of the fluxgate and search coil magnetometers are shown in Figure 5.5. We took 2 hours for this. The weather was quite windy.

Current status: The fluxgate magnetometer is working fine at both systems, trouble with GPS interfering with Iridium at both places (at System 4 even with lowered height of GPS antenna), interference at the System 3 search coil magnetometer (we are yet to find out about the System 4 search coil). Tomorrow, we plan to take down System 4 Iridium antenna, tilt it by about 5 deg (need to know exactly which direction) and create a ground plane for it.

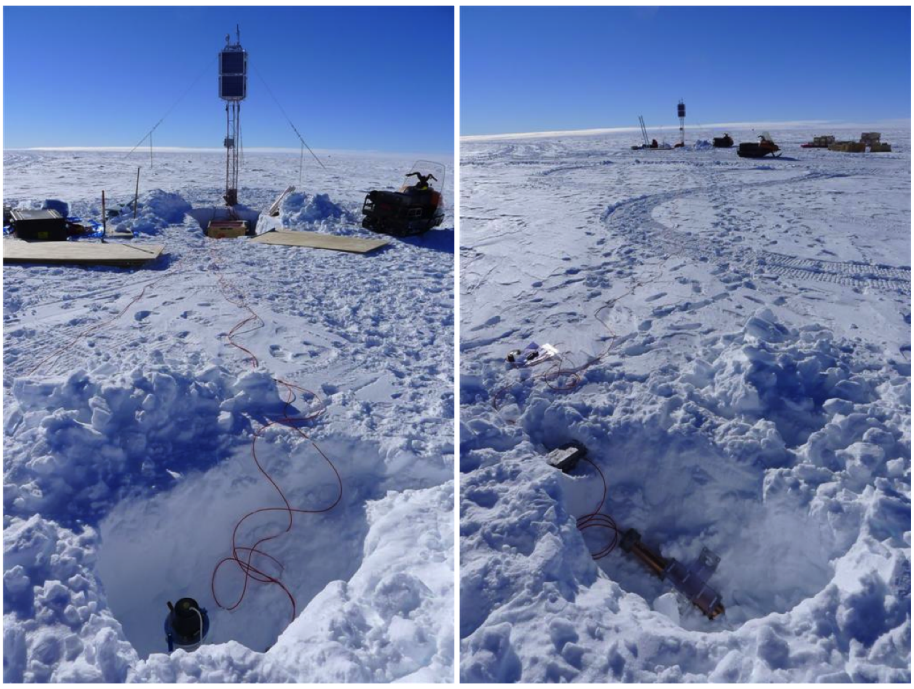

Figure 5.5: Fluxgate and search coil magnetometers installed.

Day 4: December 31, 2010. We retrieved the Iridium antenna from the system, got an aluminum plate from a junkyard in the South Pole station's science lab. With the help of Bob Melville, we got that plate attached to the Iridium antenna as its ground plane. At 11.00 am, we got the tilted Iridium antenna (away from GPS antenna) with ground plane up (Figure 5.6). We tried calling Steve for fluxgate alignment but the iridium battery died. In all this exercise, the TNC connector at the Iridium antenna was a trouble to handle with gloves/ liners.

Day 5: Jan 1, 2011. The news was with the extra tilt (10-15deg) Iridium was losing its

Figure 5.6: Iridium antenna with a ground plate.

connectivity too often. So, we decided to straighten the Iridium but leave the ground plane on. If not, we can leave the antenna tilted and take out the ground plane. Today, we finished the tower, cabling in the pit, organizing the cables as much as we can, HF antenna cabling and getting the shipping boxes ready to go to the storage place in about 4 hours. We also had to redo the GPS connection while organizing the GPS cable. The system was shut down from 1:15 pm to 2:45 pm. For System 3, we changed the GPS antenna to Antcom antenna.

Challenges and suggestion: The biggest challenge was to organize the cables. Most of the cables are manageable but not the solar panel ones. Especially, since they come in as a pair for each set of two solar panels and then are joined together to give out only one connector near the battery box. So we have 6 connectors at the tower end and 3 close to the battery box. It was a challenge handling those long cables separately for each set of solar panels especially since we got the panels at the top almost at the end of the whole installation. We could have actually tied the two cables together from one set of solar panels almost till the very end. This would have made the cables much more manageable. Remember, it is hard to coil these cables when they are cold and stiff. We need more zip ties in organizing the cables.

Day 6: Jan 2, 2011. Today morning, we removed the ground plane for Iridium antenna because, even when it is not tilted, the ground plane was still hampering its connectivity. Although, this time, with the solar panels at the top, this task was more strenuous. Windy environment and tight TNC connector at the Iridium cable made it all the more difficult. All TNC connectors have so far been a huge problem. From System 3, the GPS pole was retrieved. But, since we could not find the System 3 shipping boxes in the berm, we decided to keep this pole in the System 4 shipping boxes (It is placed in the instrument box).

A photograph of a contented team after a successful installation of an AAL-PIP system during the 2010 expedition is shown in Figure 5.7.

Figure 5.7: The team with completely assembled AAL-PIP system. From left to right: Dr. Bob Clauer, Kshitija Deshpande, Joseph Macon and Dr. Hyomin Kim.

5.3 AAL-PIP Remote Operations

As mentioned earlier, each AAL-PIP system can be accessed via an Iridium channel. Since 2012 Antarctic season, I have been involved in maintaining the remote operations using the Iridium link. These operations include data downloading, periodic examination of the system health, maintaining CASES, and managing the remote installations of AAL-PIP systems.

The AAL-PIP systems are completely autonomous and provide no real-time feedback directly to the field team. After completing the hardware installation in the field, the team calls the remote operator through a separate Iridium line. The operator accesses the system remotely to check the overall health of the system and the status of each instrument separately. This section briefly describes the procedures followed during the system installation and the afore-mentioned tasks.

An Iridium data service known as Router-Based Unrestricted Digital Internetworking Connectivity Solutions (RUDICS) is used during the telemetry operations. RUDICS server allows a connection to more than one remote systems. A "console" program and Python based software developed by Steve Musko in University of Michigan, Ann Arbor is utilized in remote operations.

5.3.1 AAL-PIP Installation

Open a secure shell (SSH) in the RUDICS server and follow the procedure listed below.

```
$ con_<sys>   --------- to enter a remote system. <sys> = remote system #
tincan[field]1\# console --------- to enter the console environment
console> con <subsystems>
where <subsystems> = super (supervisor)/ cases (CASES)
/ sc (real time search coil data)
/ fg (real time fluxgate data)
/ hf (HF)/ hw (hardware status etc.)

console> help --------- to see available commands
```

```
console> dis --------- to disconnect from the subsystem
console> exit --------- to disconnect from the console
```

Caution: System looses connection if the console/ ssh window is inactive for 5 minutes. So keep pressing "enter" now and then. If the connection is lost, wait for the next half an hour when system pings to see if the server is trying to make a connection. If the connection is lost accidentally due to handover etc., the remote system tries to reconnect to the host again sooner.

For more than one system, carefully open terminals if you have to. There is no other way than looking at the initial $con_<sys> command to know which terminal has which system. You can have only one copy of console at one time (even considering many different computers). For one system, you can have one console and another terminal window showing current log files (e.g. tail -f client_proxy.log) from RUDICS server.

Inside the hardware subsystem, "status" command prints the hardware status.

```
Heater: generally off = 0
Ethernet:  off field
Garmin GPS: ON every hour
USB, RS232, PC104: always ON = 1
Batt1: battery box 1 temperature
Router board temperature (not CPU board temperature):
should be < 40 deg C, real electronics box temperature
FG sensor temperature: shows ambient temperature
Raw volts: only used for calibration
Battery voltage: Should be > 12V typically; if > 13.2 V then charging,
< 12.6V indicates discharging.
I/P power: 13-14 W when CASES is ON
Overcurrent: = 0 generally, when everything is fine
    = 1 overcurrent detected, short circuit, not normal
*****The way to recover from overcurrent is:
Go to hw> reset_overcurrent ------ to reset router board over current condition
Time and position:
System time: should be proper, if not, there is some problem
System time error: should be close to zero
(can go to 100 ms sometimes, worse)
UTC sync age: should be close to 3600 seconds,
```

```
if huge number-> GPS is not syncing well.
OS:
Uptime: Shows cumulative total time the system has been running after the last reset.
Should be able to explain uptime.
Load average: any number <1 is good
```

In January (peak Austral summer), the voltage keeps fluctuating from 13 to 14 V; 11.2 V indicates that the system has gone into hibernation.

The command "super" stands for supervisor which is the highest level command set. The supervisor masks all operation schedules, e.g. if CASES is turned OFF, CASES will have to complete the current data collection cycle and quit until it is turned back ON by the supervisor. One needs to switch CASES and HF ON manually after every system restart or when the system comes back to life after the winter. AAL-PIP CASES receiver operates in three different modes which can be accessed via "super". The Update mode is used to keep the receiver ON continuously, and is generally used while performing remote installations/ maintenance of CASES. The Storm mode keeps the receiver ON and OFF every alternate hour. During geomagnetic storms or any other specific campaigns, CASES is manually switched to Storm mode. Keeping the receiver OFF every other hour restricts the electronics box temperature from increasing beyond 40° C. CASES is generally operated in the Normal mode in which CASES is turned ON four times a day (e.g. at 1, 7, 13, 19 UT) for an hour, or until a hard daily data collection limit of ∼13 MB is reached. The following commands are included in super:

```
super> help
super> cases on/off
super> hf on/off
super> cases update_mode/storm_mode/normal_mode
```

Console checklist for new system installation when the system is just turned ON:

1. Check if SC, FG, Iridium, GPS are ON from hw.

2. Battery box1 voltage is close to 13-14 V and the rest (box2, box3) are lesser (as they are

not connected).

3. Make sure GPS UT synch age is close to 3600 s.

4. Router board temperature close to 40° C and FG sensor temperature close to ambient -20° C in summer.

5. USB, PC104, RS232 = 1, overcurrent = 0.

6. Uptime should be explainable (<24 hr).

7. Turn on CASES and HF from super. Verify the correctness of the commands from /var/log/-console.log file.

Fluxgate Alignment:

```
console> con fg ------- to show real time FG data
```

Shows 5 columns, occasionally 6 [X, Y, Z, Sensor_Temperature , Electronics_Temperature] 'Calibrating' flag appears when there is a huge sudden change and the instrument needs to recalibrate itself.

1. X Y Z ≡ H E Z axes of Geomagnetic field.

Y=E should be close to zero. At the same time, X=H should be a huge positive number (confirm with a working system output).

2. Wait until the 'Calibrating' flag disappears. This may take a couple of minutes (∼ 160 seconds if the magnitude of field changes by as much as 40000 nT at 256 nT/s rate).

3. Inform the field team of the real time Y and X axes values as they change. To avoid confusion, it is recommended to simply mention the values, not an expected direction of rotating the fluxgate.

4. Make sure the total field from the FG display is consistent with the IGRF field at the station location.

Search coil shovel test:

The search coil real time values appear in two columns, X and Y. The values appear in bits and are displayed with 10 Hz sampling frequency. One way to validate the search coil operation is to make sure the values saturate when a large metallic object (shovel) is moved in its vicinity.

```
console> con sc ------- to show real time SC data
```

The following is a checklist for the search coil shovel test:

1. 10 numbers are displayed every second.
2. Stable if no one is around.
3. See if noise appears in each block and across the block by moving a shovel close by at a rate of about 1 Hz.
4. The response on SC dampens slowly within 10 seconds or so after the shovel is taken away.
5. Check if the saturation levels are reached with shovel test at its peak.
6. Saturation levels in X Y bits are ± 2048.

Checklist to confirm the working of remote system:

The following is a checklist before the field team is cleared to head back.

a) System is turned ON.

b) HW status OK - It is updated every 15 seconds.

c) FG alignment and SC shovel test successful.

d) To save time, start downloader manually for that day (after 2-3 hours of data collection on the system's single board computer is completed). Otherwise, the downloader will turn ON only at midnight UT. Files can also be extracted individually using ssh-get or scp. Note that scp creates new ssh while ssh-get uses the same ssh you have logged in with.

e) Keep checking the log files, data directory on the server for downloaded files.

f) Keep monitoring the electronics box temperature. If high, turn OFF HF and CASES.

g) Validate the downloaded data for each instrument by generating preliminary plots.

Checking the recent log files:

1. Go to aal-pip/field/reboot_logs in the remote system's file directory (not the RUDICS server's).

2. super.log and hw_mgr.log files show logs that were saved before the last system reset.

3. Go to /var/log/ on the remote system. These show live logs. console.log shows command history in console super.log, cases_mgr.log, fg_mgr.log, sc_mgr.log. These log files track the status of each subsystem (instrument) in real time.

4. $ cat *.log |grep ERROR —– shows all log files with error message

e.g. sc_mgr.log would show when data packets were missing. This could correspond to a time SC was turned off. SC and FG should not show any gaps or errors.

5. gps_mgr.log should show values close to zeros and close to 1 hour different time stamps.

6. svr_proxy.log — server proxy log on remote system is equivalent to client_proxy.log on RUDICS server.

5.3.2 Data Downloading

Following are some important notes useful to check the log files and data files on both the remote system and the RUDICS server.

We have noticed that some probable hardware or software issues lead to time stamping errors in the systems as they age. These errors are responsible for producing large number of FG and SC files, followed by turning OFF the data collection from FG and SC. The system needs to be rebooted on the occurrence of these errors. Thus, a constant daily check on the number of files and missing files is required. Python codes written for this purpose are listed in Appendix C. These codes send a daily alert email about the status of number of files along with some house keeping data which is useful in monitoring the health of the system.

```
To check log files on the remote system:
tincan[field]1# cd /var/log/
  # cat gps_mgr.log------ to check of health of GPS system
```

```
To see most recent log file on RUDICS server:
$ ops ----- takes you to log folder
$ car client_proxy.log
Downloaded copies of files are stored in:
/mnt/usbflash/data/hskp       (for house keeping files)
/mnt/usbflash/data/fg
/mnt/usbflash/data/sc
/mnt/usbflash/data/cases
/mnt/usbflash/data/hf

Directory structure in Michigan server:
/home/musko/ops/aal-pip/bin/
/home/musko/ops/aal-pip/log/
/home/musko/ops/aal-pip/data/
The above data/ folder has all the data files ordered properly.
But, another copy of the data files that are directly dumped from
Iridium into RUDICS server in folder:
/usr/share/aal-pip/data/
```

From a remote system, only one Iridium link of 2.4 kbits/s exists. More than one SSH log in for downloading and console may slow down the connection by a lot. Therefore, close the downloader for that system. Find the PID of the current downloader process and kill it. Sometimes it takes a while for the downloader to stop. It systematically completes its current task and quits. Double check using grep, that no downloader is running for that system. Restart downloader for that day (to use up the rest of the hours for downloading), if not, it will start automatically at midnight.

```
$ ps - Af | grep downloader --- to find downloader programs
To restart downloader:
$ cd /home/musko/ops/aal-pip/bin -----directory with all executables
$ download.py sys_{x} & ---------start download for system_{x}
```

Do not close the terminal window if the downloader is called as described above. Else, simply start a screen. Run the downloader.py and detach the screen.

```
$screen  ------to start a new screen
screen0$ downloader.py sys_{x}
```

```
control a+d ------ to detach the screen
$screen -r ----reattach the screen
```

AAL-PIP data upload/ download rate is 240 bytes/sec + overhead ⇒ 230 bytes/sec. Thus, the daily data transfer is restricted to 230 bytes/sec * 86400 sec = 19,872,000 bytes = 19.8 MB. This is the maximum data that can be downloaded in 24 hours if the Iridium connection is continuous without any drop-offs.

In order to change the download configurations for different cases, the following procedure is recommended. In RUDICS server's bin folder, /home/musko/ops/aal-pip/bin/ download configuration files: dl_config.ini (sys_<x>_dl_config.ini) can be found. Edit that for different purposes. Two fields that can be turned ON and OFF by using true/false, with priority as their order of appearance in the .ini file are:

1. Yesterday: To download the most recent files from previous day, as the downloader starts every day at 00:15 UT till 23:45 UT. Priority of data downloading for each instrument is in the order of appearance of their names.

2. Catch up: For downloading older data. Example: If we want to download data for 6 storm time days/ missed data for 6 days, the following are the steps.
   a) Turn off yesterday's data download.
   b) Catch up data from all subsystems except CASES with first day and last day of those 6 days and run the downloader (for number of days that can be computed at the rate of 3 MB/day for all the subsystems minus CASES).
   c) Check download_sys<x>.log1 download_sys<x>.log2 (2 is older than 1) to make sure the data for all other systems (hskp, sc, fg, hf) has been downloaded first.
   d) Catch up part of downloader: change to just CASES and those 6 days and catch up with it.
   e) Download log files and check everyday if downloading is occurring properly.

f) For the last part, we will have to forgo the daily data download of CASES or all instruments. To prioritize CASES over daily download, turn OFF "Yesterday" completely. In catch up, just mention CASES for downloading the data over the required 6 days.

g) Remember we cannot download more than 16 MB per day.

The following are the data storage frequency for each instrument:

1. CASES: every 10 minutes or when file size is 75 kb.

So, if the file time is 10 minutes $\sim$ 75 kb, CASES collected low rate data only. If the file time is very small $\sim$ 1 minute which means that corresponds to 75 kb and the data packet also has high rate data.

2. Fluxgate: every 1 hour.

If the system is turned off accidentally or for any reason, say 4:30 hours after it was turned ON, FG data for the last half an hour would be lost since FG data is written to the usbflash every hour.

3. Search coil: every 15 minutes.

If SC is turned on at 14:05 minutes, the first file will be 10 minutes long instead of 15 minutes.

4. HF: every 2 hours (HF turns ON for 10 minutes).

5.3.3 Procedures for Specific Operations

Step by step procedures for certain operations are given below.

I. Procedure of uploading CASES config files:

The following is a procedure to upload new CASES configuration files (sbconfig and dspconfig) in System Y flash memory (CASES is not ON).

1. Rename your test config files to sbc.config.tX where X is the test number. Renaming of the files is recommended for two reasons: first the console program cannot handle file names with upper case letters, and second shorter names are easier to deal with.

2. Copy the config files to the /home/aal-pip/ops/aal-pip/bin directory on the AAL-PIP server using any SFTP client such as Filezilla.

3. Log in to the AAL-PIP server as the user aal-pip.

4. Wait until System Y is connected:

$ tail -f ∼/ops/aal-pip/log/client_proxy.log

This will show you all the updates to the log file. The file should be pretty self-explanatory. You can use a separate SSH connection just to view the client_proxy log.

5. Send the test config file to the /aal-pip/field directory of System Y:

$ send_Y sbc.config.tX /aal-pip/field

This will use scp to copy the file to System Y. Repeat the above for all the test config files and for the dsp config file.

$ send_Y dsp.config /aal-pip/field

The files on the remote System can be verified using "cat <filename>" or "less <filename>". If scp terminates with a zero exit code, the file was transferred error-free. The exit code is displayed when the "send_Y" command exits.

II. Procedure to upload configuration files on CASES remotely:

1. Open one ssh terminal on the RUDICS aal-pip server.

2. Open another window: $tail -f ∼/ops/aal-pip/log/client_proxy.log.

3. Put CASES in update mode:

```
$ keep_alive 4 (step 10, do this on a separate ssh terminal)
$ con_4
$ start console
$ con super
$ cases update_mode
$ cases on
```

4. Make sure CASES is on:

```
$ con hw
```

```
$ status
```

5. Enter the CASES console menu and upload the dspconfig and sbcconfig file:

```
$ con cases
$ upload_sbc_config /aal-pip/field/sbc.config.off
----- to stop enormous data collection first.
$ upload_dsp_config /aal-pip/field/dsp.config
$ upload_sbc_config /aal-pip/field/sbc.config.t8
```

6. Check $cat console.log in (/var/log/ directory) to make sure if you typed the correct commands.

7. Look at the CASES log file (in /var/log/ directory) for any errors. $ tail -f cases_mgr.log. CASES manager does the update sbconfig, sends the packets, updates log file and shows what CASES is doing (e.g. how many missing packets are there/ how many packets CASES is producing). Check in /mnt/usbflash/data/cases/<date folder> if the correct number of files are saved.

8. A well kept log file (just noting down the timings manually and write in simple words what was done) would help to keep a history of commands and your work. e.g. Steve's log file:

```
14:09:02 CASES powered up and in update mode
14:12:35 sbcconfig_Test1_LRTime10s.data uploaded
16:16:40 sbc.config.off uploaded
16:18:04 sbcconfig_Test2_LRTime20s.data uploaded
18:22:35 sbc.config.off uploaded
18:24:00 sbcconfig_Test3_LRTime2s.data uploaded
20:27:42 sbc.config.off uploaded
20:28:30 CASES powered down
```

9. Open different terminal windows as follows:

a) One for the console on System Y.

b) Second, connected to System Y (con_Y) to check cases_mgr.log or console.log or any other log files from /var/log folder on the remote System Y.

c) Third, on the RUDICS aal-pip server for client_proxy.log to see the status of connection

(tail -f ∼/ops/aal-pip/log/client_proxy.log).

d) Final terminal with a screen running keep_alive program as below.

10. Run keep alive program in a screen until the remote operation is completed.

```
$ screen
[aal-pip@localhost ~]$ keep_alive 4
Tue Nov 20 14:31:06 UTC 2012: System 4 is connected
Tue Nov 20 14:32:42 UTC 2012: System 4 is connected
```

This keep_alive program is similar to having another user logged in and keeping the Iridium connection to the system alive by sending a null file every 1.5 minutes.

11. To upload any other sbcconfig file, simply repeat steps 5, 6 and 7.

12. After all the experiments with CASES are done, upload a known sbcconfig file (sbc.config.off), to make sure that you won't accidentally collect tons of data. Also turn OFF CASES from "super".

Apart from Steps 5, 11 and 12, the same procedure above can be used to validate the working of CASES in the field. Make sure to power OFF the CASES from update mode to stop collecting a whole bunch of data, unless required for special observation campaigns. Switch it to normal mode in general case.

III. Procedure for data downloading:

1. Navigate to /home/aal-pip/ops/aal-pip/bin on the aal-pip server. The .ini files are all downloading related for each system.

2. In sys_Y_dl_config.ini, only modify the last 2 sections according to the requirement.

3. To find out which section to change, look at the total data collected on the remote system (in MBs etc. from /mnt/usbflash/data/cases/<date>, du -h), estimate how many days it would take to download these data (with 16 MB daily limit for CASES) and plan accordingly.

4. e.g. to obtain CASES data for Nov 20, 2012 change the catchup part. One could turn OFF yesterday's data collection for the magnetometers (to save first a few hours, but should not

turn OFF yesterday's data for housekeeping for example).

```
[CatchUp]
# Options for downloading catch up data
enabled = False  -> True
first_date = 2012-11-12 -> 2012-11-20
last_date = 2012-11-12 -> 2012-11-20
subsystems = cases

[Yesterday]
# Options for downloading yesterday's data
enabled = True
subsystems = hskp hf fg sc
```

5. At the start of the next day's 00 UT, in first 2 hours, yesterday's data for listed subsystems (hskp hf fg sc) are downloaded and then CASES (or other subsystem's) catch up data are downloaded. Downloader program downloads the data files and erases from the remote system.
6. Downloader needs a lot of bandwidth. Thus, slows down any uploading operations. Therefore, remember to turn OFF downloader program before opening a console for any remote operation.

IV. Procedure for handling the downloader program:

1. The downloaded files are stored at /home/aal-pip/ops/aal-pip/data. To figure out which data to download, delete unnecessary files on that day so that only that much data will be downloaded, go to: /mnt/usbflash/data/ and a particular instrument and date on the remote system.
2. There is a separate downloader process for each system. Before starting any other remote operation on any one system, find and stop the downloader for that system as given below.
List all the processes that are involved in downloading and which contain the word "download":
> ps -Af | grep download
Identify the process ID (pid) that is executing the download for a system of interest, e.g. "download.py sys_5". Kill that process: > kill <pid>

Check to make sure the process is dead: > ps -Af | grep download

3. To restart the downloader at any time for System Y: >./download.py sys_Y & (& is to let run it in background)

4. To change the downloading priorities in .ini file:

a) Stop the downloader for that system.

b) Change the ini file in ops/aal-pip/bin/ e.g. sys_5_dl_config.ini.

c) Restart the downloader for that system.

5. To download just a few days' data, Keep Yesterday = False, Catch up = True. List necessary instruments in order of requirement. List the start and end date.

6. At 00:15 UT a crontab script automatically executes a downloader for each system. The downloaders stop themselves at about 23:45 UT or when the daily Iridium limit is over or when it finishes downloading the current assigned task. If working with a separate downloader (e.g. before the field team is cleared of leaving the location), it is recommended to disable the crontab script (use "crontab -e") to prevent automatic execution of the downloaders at 00:15. It should be made sure not to have more than one downloader running for each system.

Chapter 6

Investigating the Ionospheric Irregularities during a Substorm Observed by the AAL-PIP Stations

K. B. Deshpande,[1] C. R. Clauer,[1] G. S. Bust,[2] H. Kim,[1] D. Weimer,[1].
Manuscript in preparation

[1] Bradley Department of Electrical and Computer Engineering, Virginia Tech, Blacksburg, Virginia, USA
[2]The Johns Hopkins University Applied Physics Laboratory, Laurel, Maryland, USA.

6.1 Introduction

A substorm is a disturbance in the Earth's magnetosphere caused by the loading of solar wind energy on the dayside and unloading it to the inner magnetosphere and ionosphere [*Russell and McPherron*, 1973; *Hones*, 1984]. Substorms are transient phenomena occurring close to the local midnight section of the Earth lasting for 1-3 hours. They transfer significant energy to the auroral ionosphere in the form of particle precipitation thus causing the aurora to expand poleward and equatorward.

Geomagnetic activities such as storms and substorms are known to generate disturbances in the ionosphere that can be observed as predominantly phase variations in the Global Positioning System (GPS) signals [*Coker et al.*, 1995; *Prikryl et al.*, 2010, 2011; *Kinrade et al.*, 2012; *Deshpande et al.*, 2012]. *Prikryl et al.* [2013] have reported very intense phase scintillations dur-

ing the auroral break-up and substorms with the highest percentage occurrence of moderate scintillations in the cusp. Using investigation of interhemispheric comparisons of bipolar scintillation maps, they have also reported that the scintillation occurrence is significantly higher in the southern cusp and polar cap. A GPS scintillation climatology study by *Spogli et al.* [2013] suggests presence of enhanced phase scintillations along the boundaries of the auroral oval, at the cusp (due to precipitation) and in the polar cap (due to patches). *Smith et al.* [2008] presented evidences correlating the auroral arc brightening and substorm intensification with GPS phase scintillation and cycle slips. *Skone and Cannon* [1999] and *Skone and De Jong* [2000] studied the impact of substorms on GPS receiver performance and demonstrated that significant variations in total electron content (TEC) are observed during auroral substorm events. The spatial characteristics of such disturbances suggest scale sizes of ionospheric irregularities less than 50 km.

In this chapter, we are trying to explore the possibility of substorms generating the GPS scintillations over Antarctica using Autonomous Adaptive Low-Power Instrument Platform (AAL-PIP) instruments, namely, the fluxgate and induction magnetometers and Connected Autonomous Space Environment Sensor (CASES) GPS receivers. Recently, *Kim et al.* [2014a] have reported a possible connection of ionospheric irregularities to a substorm event using simultaneous observations of ultra low frequency (ULF) waves and GPS scintillations. In this study, we attempt to follow a similar approach, but with an additional use of a scintillation model described by *Deshpande et al.* [2014] to investigate whether the source of ionospheric irregularities was indeed a substorm. The model is called Satellite-beacon Ionospheric-scintillation Global Model of the upper Atmosphere (SIGMA). This will be used along with an inverse method to derive the physics of the irregularities that caused GPS scintillations. We focus on an event of 9 January 2014, which was a fairly minor substorm, but showed simultaneous phase scintillations on both PG2 and PG3 AAL-PIP stations. This event was chosen based on the duration (longer than 30 seconds) of GPS scintillations. Scintillation events with longer lengths are preferred while implementing the inverse modeling technique.

6.2 AAL-PIP Observations

On 9 January 2014, three remote AAL-PIP stations PG2, PG3 and PG4, each with fluxgate and search coil magnetometers and a CASES GPS receiver were collecting data. An earlier generation AAL-PIP, PG1, with just a fluxgate magnetometer was also operating on this date. It should be noted, however, that CASES receivers were operating in normal mode which is described in Section 5.3.1. Thus, CASES receivers were ON from 1:00 UT to 2:00 UT. PG4 CASES receiver did not record any scintillations, while PG2 and PG3 recorded longer than 40 seconds phase scintillations.

The multi-instrument observations from PG1 to PG4 are illustrated in Figure 6.1. The fluxgate magnetometer readings from all four stations are displayed for the H component while the induction magnetometer readings from PG2, PG3 and PG4 are displayed for X component, both of which are aligned along the local magnetic field line. The search coil spectrograms represent power as a function of frequency and time. The onset of the substorm expansion occurred around 00:40 UT and the substorm signatures (growth, expansion and recovery phases) are clearer in fluxgate data from PG3 and PG4. PG2 and PG3 recorded GPS scintillations at 1:10 UT and 1:06 UT, respectively. During this time the substorm was in its recovery phase. This may be one reason to believe that the substorm could be the source of ionospheric disturbances which may lead to scintillations.

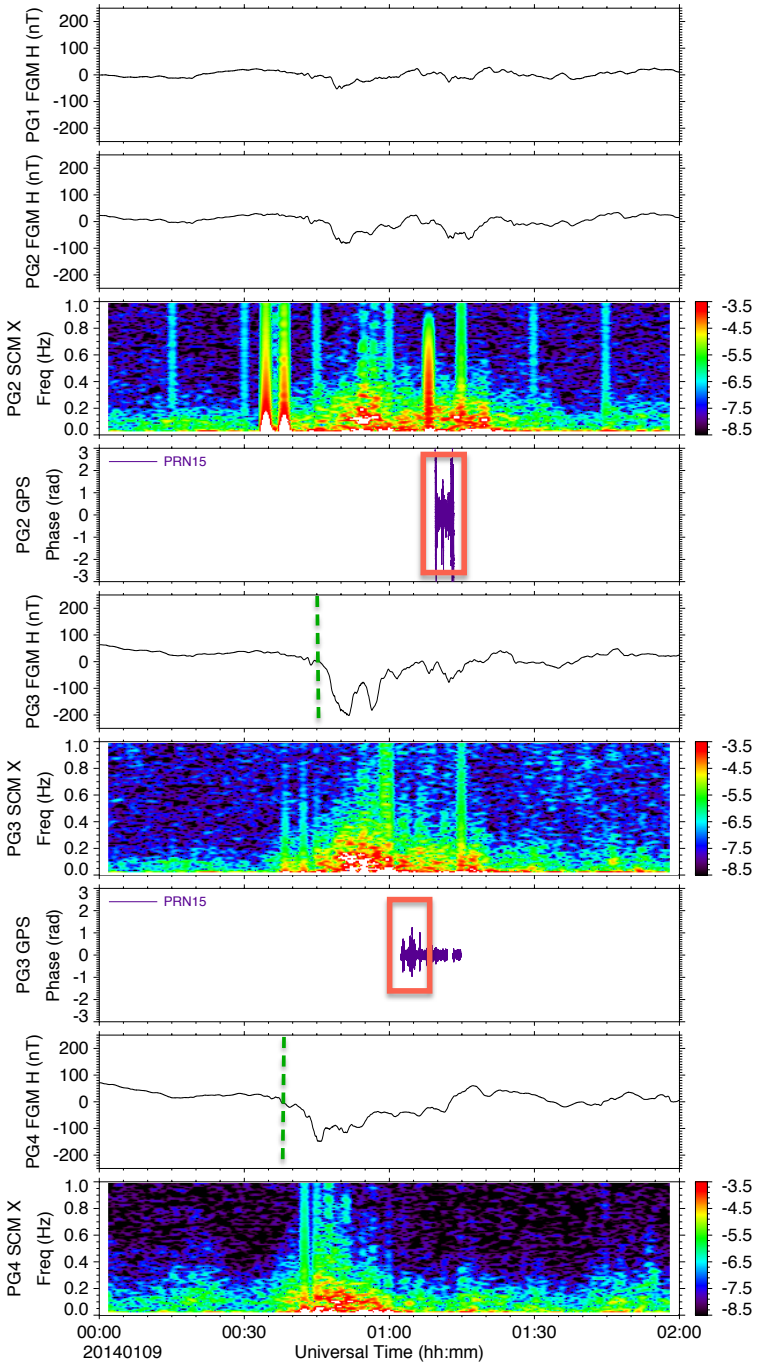

Figure 6.1: Multi-instrument observations from PG1, PG2, PG3 and PG4 on 9 January 2014. Observations from top: PG1 fluxgate, PG2 fluxgate, PG2 search coil, PG2 GPS phase, PG3 fluxgate, PG3 search coil, PG3 GPS phase, PG4 fluxgate and PG4 search coil. The components aligned along the horizontal local magnetic field line: H for fluxgate and X for search coil are displayed here. The red boxes highlight the GPS scintillations, while dashed green lines represent the onset of substorm observed at PG3 and PG4. PG2 fluxgate data shows a very weak substorm signature.

6.3 Auxiliary Observations

A magnetospheric substorm is typically accompanied with an enhancement of westward electrojet. This enhancement could be identified from large decrease in the lower auroral electrojet (AE) indices. Among the four AE indices, AL represents the magnetic disturbance due to enhancement of westward electrojet. The four AE indices on 9 January 2014 are displayed in Figure 6.2. The small dip around 00:30 UT may point to a minor substorm, but it is not a clearer signature. The AE indices are determined by averaging over magnetometer data from several northern high latitude stations. Thus, a minor substorm may not be clearly visible in these indices. Furtheremore, Advanced Composition Explorer (ACE) interplanetary magnetic field (IMF) data without the delay correction from 20:00 UT on 8 January 2014 to 20:00 UT on 9 January 2014 are shown in Figure 6.3. IMF B_z component is less than -5 nT from 22:00 UT on 8 January 2014 until 02:00 UT on 9 January 2014. This southward turning of the IMF B_z at dayside magnetopause is a possible source of energy for a substorm. In order to confirm that this event is indeed a substorm we utilize the interhemispheric conjugacy. We present the fluxgate magnetometer observations from Greenland coastal stations conjugate to the AAL-PIP PG1 to PG4 locations in Figure 6.4. A substorm signature is clearly visible in the H component of these data with an onset of substorm occurring around 00:35 UT. The Geographic and Corrected Geomagnetic (CGM) coordinates of these locations are listed in Table 6.1.

Table 6.1: Geographic and CGM coordinates in degrees of the locations of AAL-PIP stations and their northern hemispheric conjugate stations in Greenland.

AAL-PIP sites	Geog lat (N)	Geog lon (E)	Conjugate CGM lat (N)	Conjugate CGM lon (E)	Conjugate geog lat (N)	Conjugate geog lon (E)	Greenland Conjugate sites
PG1	-84.5°	77.2°	75.99°	41.22°	70.68°	307.87°	Uunmannaq (UMQ)
PG2	-84.42°	57.96°	74.82°	38.15°	69.25°	306.47°	Qeqertarsuaq (GDH)
PG3	-84.81°	37.63°	73.54°	37.09°	67.93°	306.43°	Attu (ATU)
PG4	-83.32°	12.97°	70.93°	36.43°	65.42°	307.1°	Maniitsoq (SKT)

OVATION Prime plot [*Newell et al.*, 2009; *Machol et al.*, 2012] with the forecast of the

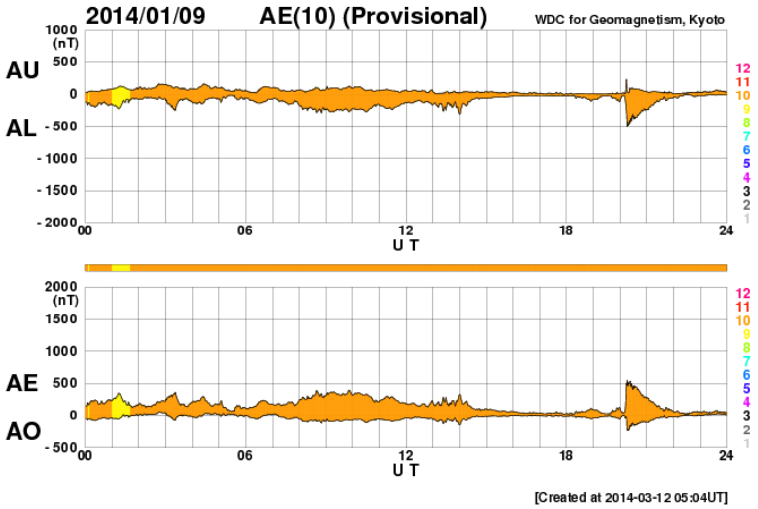

Figure 6.2: AE index on 9 January 2014 (obtained from Kyoto World Data Center).

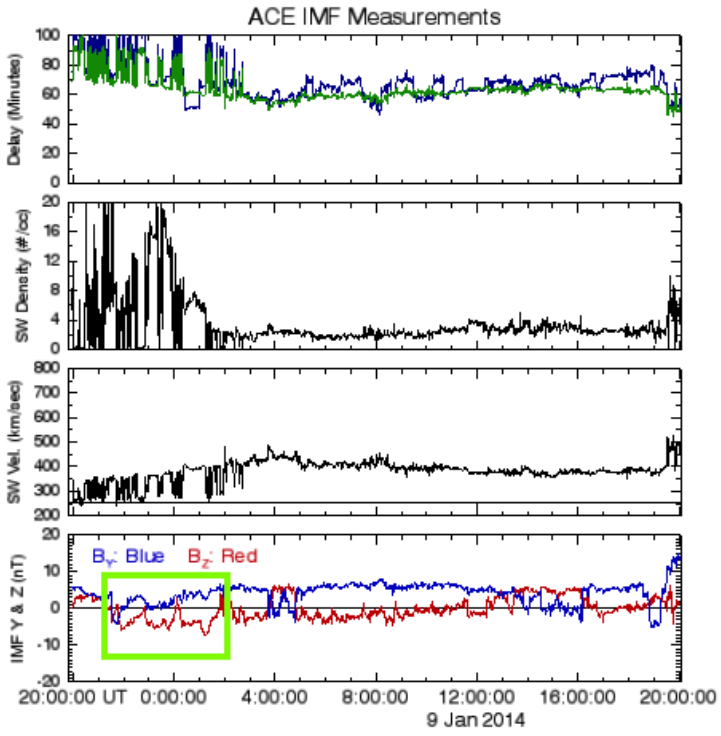

Figure 6.3: ACE IMF data from 20:00 UT on 8 January 2014. Southward turning of IMF B_z is highlighted with a green box in the last panel.

Auroral oval, which uses the ACE data, at 1:00 UT on 9 January 2014 over Southern polar region is shown in Figure 6.5. Compared to another time (00:00 UT), this Auroral oval prediction

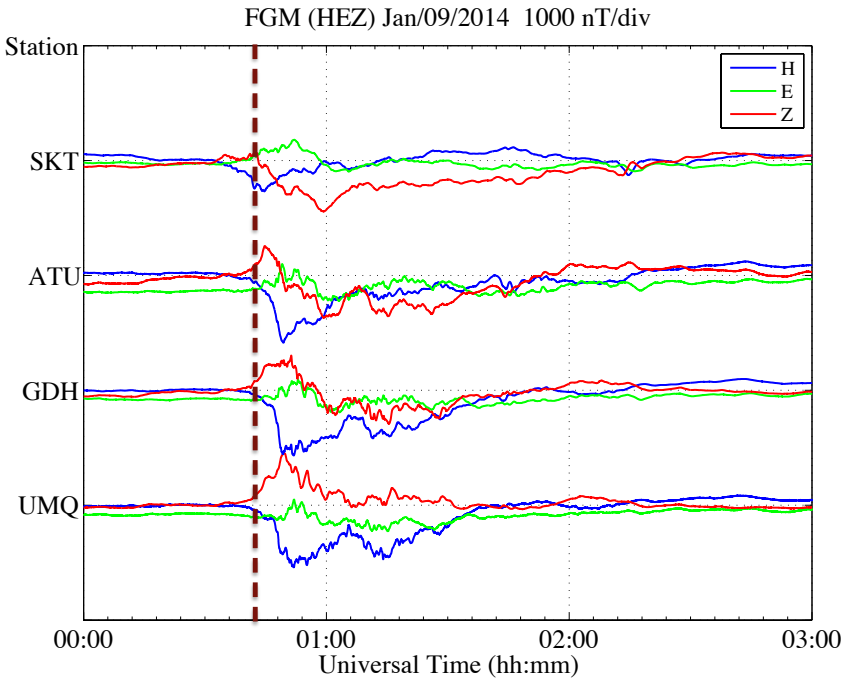

Figure 6.4: Stacked plot of fluxgate HEZ components from Greenland stations conjugate to the AAL-PIP stations. The dotted brown vertical line indicates approximate time of onset of the substorm.

appeared to be bigger, indicating increased particle precipitation. This is an additional evidence of an occurrence of a substorm. Furthermore, the particle precipitation data from Special Sensor Ultraviolet Spectrographic Imager (SSUSI) instrument on the Defense Meteorological Satellite Program (DMSP) satellite F18 over-plotted on the Antarctic map from Google Earth is shown in Figure 6.6. The prediction of poleward boundary of the Auroral oval is highlighted in red. The locations of PG2, PG3, PG4 and South Pole (SPA) are displayed. PG3, which is located at the typical latitude of the dayside cusp, appears to be inside the auroral oval as would be expected for the night-side oval. While PG4 is inside the auroral oval, PG2 appears to be on the poleward boundary of the oval.

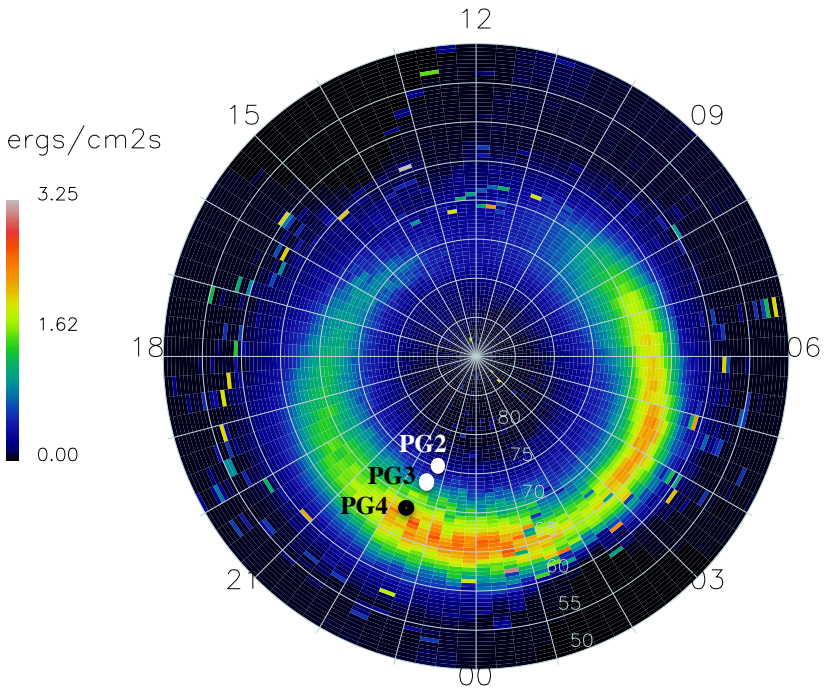

Figure 6.5: Forecast of the Auroral oval over Antarctica in magnetic and MLT coordinates with the locations of AAL-PIP sites PG2 and PG3 (obtained from the National Geophysical Data Center) at 00:45 UT on 9 January 2014.

6.4 Inverse Modeling and Discussion

SIGMA is a GPS scintillation model that can be used with an inverse method to derive the physical parameters of an irregularity generating phase scintillations. Along with the auxiliary observations described in Section 6.3 and AAL-PIP observations described in Section 6.2, we use SIGMA to determine the physical parameters pertaining to the ionospheric irregularities during this event. Unknown parameters such as spectral index $SpInd$ of the irregularity power spectrum, the background number density ΔN, altitude of the irregularity H_{iono} and the drift velocity $\vec{v_d}$ of the structure can be estimated from the best fit of the modeled data to the observations.

AAL-PIP fluxgate observations (HEZ axes) for PG2 and PG3 are plotted for a 3 hour period in Figure 6.7. The onset of the substorm can be seen at 00:40 UT. Equivalent magnetic

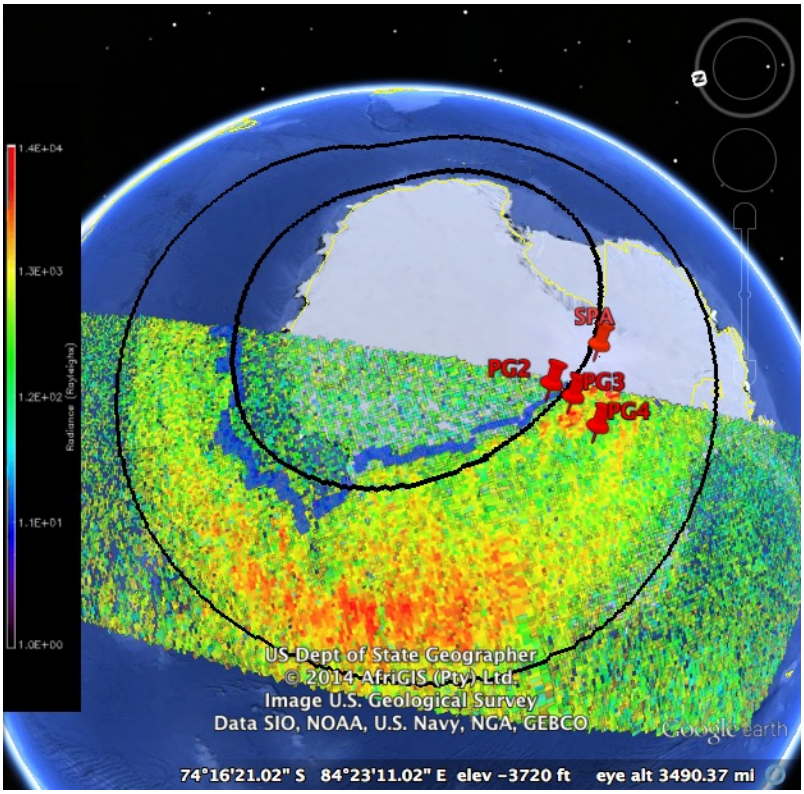

Figure 6.6: Energetic particle precipitation over Antarctica from SSUSI instrument on the DMSP satellites at 00:45 UT on 9 January 2014. Auroral boundaries (poleward and equatorward) derived from the Global Ultraviolet Imager (GUVI) model are shown in black ovals. The poleward boundary of the auroral oval from the SSUSI data is shown in dark blue color.

convection vectors as ionospheric convection flow patterns derived from H and E components are plotted in Figure 6.8. The patterns represent $\mathbf{E} \times \mathbf{B}$ convection, and illustrate temporal changes over the latitudinal extent. *Kim et al.* [2014b] describe more about this method in detail. We utilize the equivalent convection of the ionospheric structures at the time of the GPS scintillations observed on both PG2 and PG3, to estimate an approximate direction of the drift velocity vector in each case. These directions are also shown in the figure as red lines. When fitting the modeled data to the observed data using SIGMA, we set a range of drift velocity directions centered around the direction angles thus derived. Note that data coverage from SuperDARN in the southern hemisphere on this date was extremely sparse. This encouraged us to explore the above-mentioned option for obtaining information about the structure drift

directions.

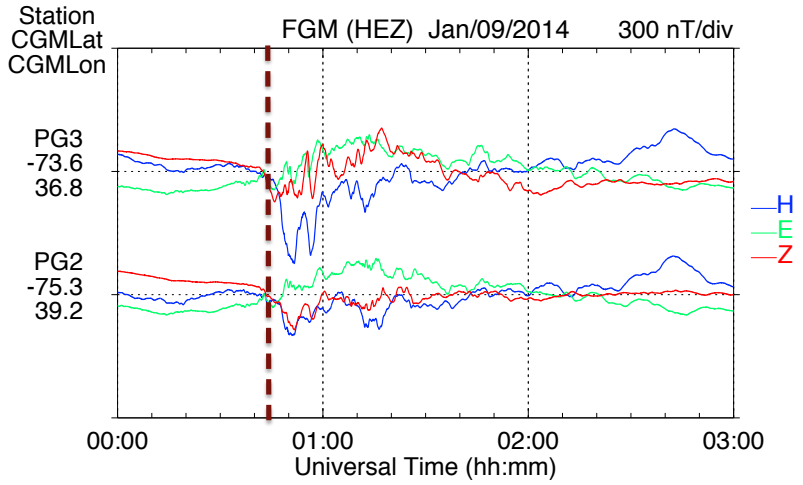

Figure 6.7: Fluxgate HEZ components for AAL-PIP PG2 and PG3 stations during midnight to 3:00 UT. The dotted brown vertical line indicates approximate time of onset of the substorm.

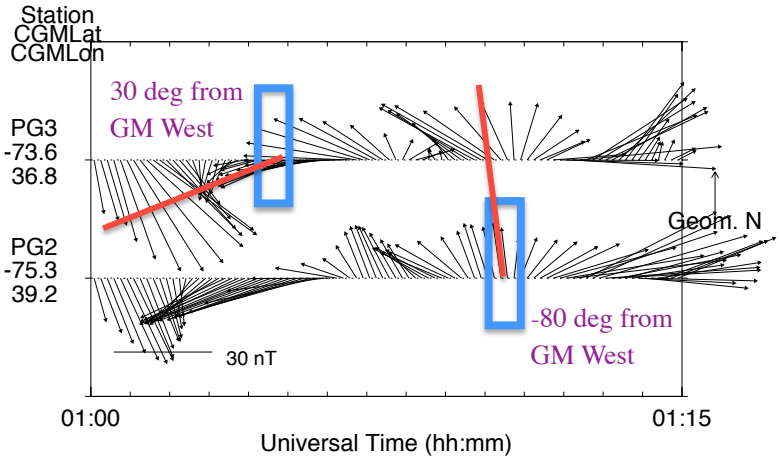

Figure 6.8: Zoomed in Figure 6.7(b) during the 15 minutes when phase scintillations were observed on PG2 and PG3 CASES receivers. The blue squares represent the GPS scintillation periods and the red lines illustrate equivalent convection vectors at those times.

We performed inverse modeling using SIGMA with the following input parameters:

1. Outer scale, $l_0 = 15$ km
2. Thickness of the irregularity, $L_{Th} = 10$ km

3. Axial ratio, AXR = 10

The axial ratio denotes the anisotropy of rod shaped irregularities. The outer scale depicts the diameter of these rods and its value is taken to be consistent with the typical scale sizes of irregularities during substorms as suggested by *Skone and De Jong* [2000].

The azimuth and elevation angles of GPS satellites during PG2 and PG3 scintillations were (-50°, 57°) and (-30°, 53°), respectively. The observed GPS phase data were filtered using a high-pass Butterworth filter with 0.1 Hz cutoff frequency to eliminate low frequency effects such as the satellite motion and tropospheric effects. A chi-square fit is found from the power spectral density (PSD) of GPS phase from SIGMA and the observations. The frequency range in which the PSDs are compared is from 0.2 Hz (after the cut off frequency to avoid filter effects) to 8.5 Hz (where the roll off to noise floor ensues).

The best fits for PG2 and PG3 observations were found after running SIGMA simulations over a 4-dimensional (4D) grid of about 3500 points with ΔN ranging from 1e11 to 1e12, $SpInd$ from 0.6 to 6, magnitude of $\vec{v_d}$ from 200 m/s to 1000 m/s and direction of $\vec{v_d}$ from -50° to -110° for PG2, and 0° to 60° for PG3. These angles are ±30° of the directions denoted in Figure 6.8. The simulations were performed at two different heights, 120 km and 350 km.

Figures 6.9 and 6.10 illustrate the time domain and frequency domain comparisons of the best modeled fits and observations for PG2 and PG3, respectively. From Section 6.3, PG3 appeared to be inside the Auroral oval, which means the height of the irregularity was 120 km. Indeed the best fit appears to be at 120 km compared to 350 km. The best fit for PG2 was also found at 120 km, which is a probable result of particle precipitation at higher latitude. $SpInd$, ΔN, v_d (magnitude) and $\angle v_d$ for PG2 and PG3 are 3, 9e11, 850 m/s, -50°, and 2.4, 1e12, 100 m/s, 40°, respectively.

In Sections 6.2 and 6.3, we establish that the event under study is a minor substorm. *Prikryl et al.* [2013] reported occurrence of significant scintillations at South Pole during a

substorm, but they could not establish a clear relationship between the scintillations and an ionospheric irregularity generated by the substorm. The missing link here is inverse modeling. For the event under consideration, the modeling results in this section indeed imply to similar physical parameters of the irregularities. However, the magnitudes of the drift velocities found at PG2 and PG3 are significantly different. It should be noted that PSD of phase scintillations at PG3 displays three different parts with different slopes, making it difficult to find a single slope fit. Also, the spectral power of amplitude scintillations appeared to be very low (less than -35 dB). This low power may indicate predominant presence of noise. Thus, at least for PG3 case, the scintillation power is too low to unequivocally determine the best fits from SIGMA. Therefore, for this event, it is difficult to utilize the inverse modeling to understand the source of the GPS scintillations at PG2 and PG3, and investigate whether it is the substorm. Knowledge of drift velocities from SuperDARN, all sky images or absorption from riometers (which depict the presence of aurora) over each station would prove beneficial in such an analysis.

In summary, there are limited auxiliary data to support our hypothesis that the irregularities are from the same source and are triggered by the substorm. A deeper statistical study with more evidences of such events with ample auxiliary data are required for the verification of the above-mentioned proposition.

6.5 Conclusions

This chapter presents the preliminary findings of GPS scintillations coexisting with a substorm event on 9 January 2014. We postulated that if simultaneous observations of GPS ionospheric scintillations and a geomagnetic substorm are correlated, we can relate the two observations to the same source of ionospheric irregularity, i.e., substorm. We carried out inverse modeling using SIGMA for the two cases with the help of available auxiliary data and derived H_{iono}, $SpInd$, ΔN, v_d (magnitude) and $\angle v_d$ values. Of these physical parameters, the number densities and spectral indices for PG2 and PG3 along with the altitudes may indicate that the

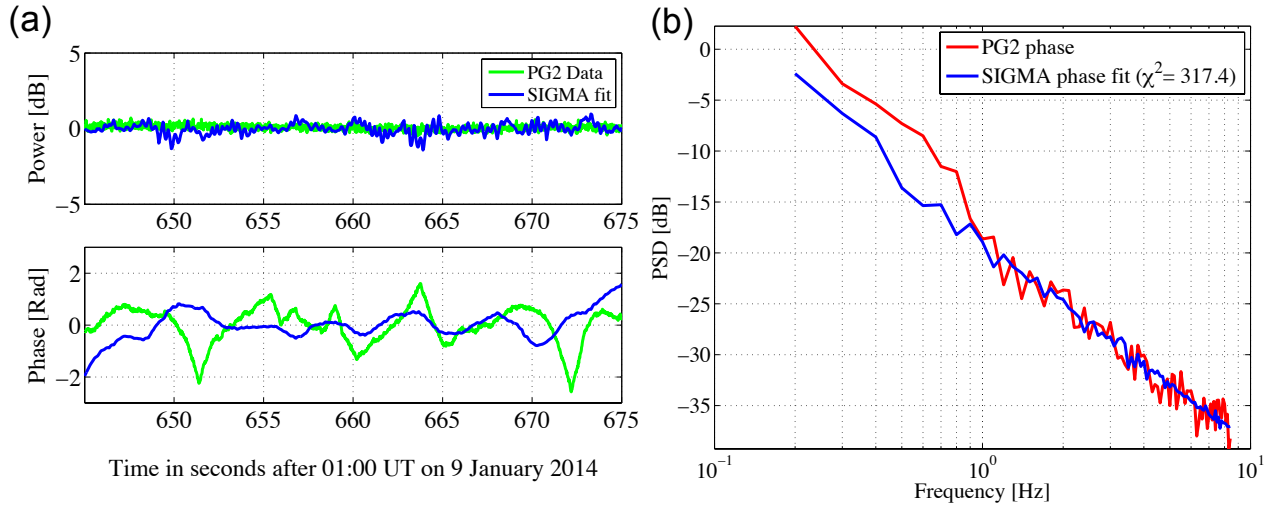

Figure 6.9: Best fit GPS scintillation results from SIGMA for PG2: (a) Time series of power in dB and phase in radians, (b) PSD of phase scintillations.

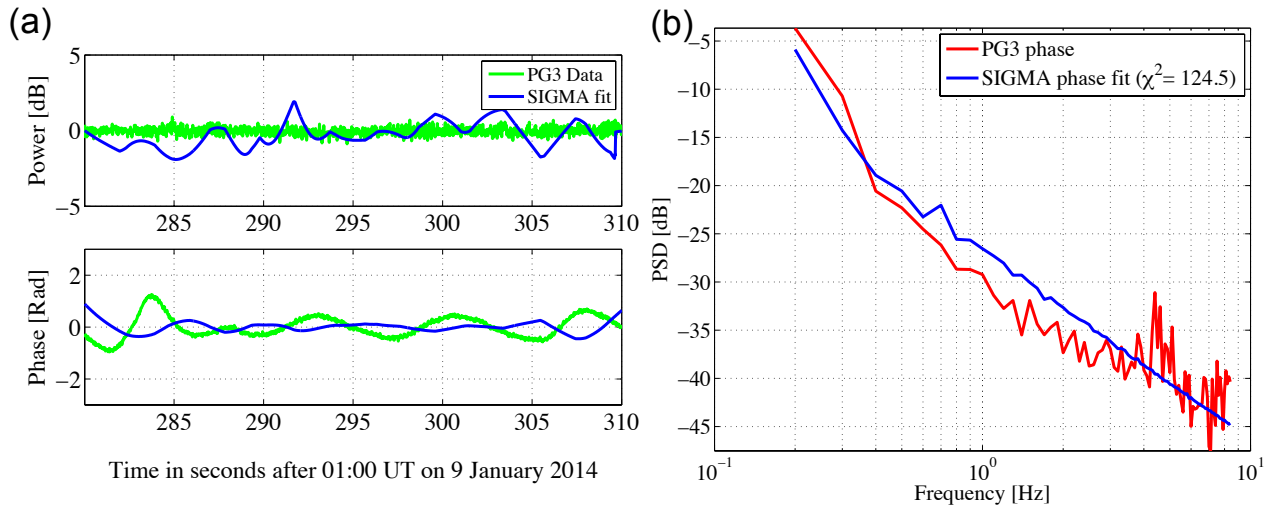

Figure 6.10: Best fit GPS scintillation results from SIGMA for PG3: (a) Time series of power in dB and phase in radians, (b) PSD of phase scintillations.

two scintillations have the same source. However, the magnitudes of drift velocities are significantly different contesting the hypothesis that the substorm is the source of the irregularities. More simultaneous observations along with sufficient auxiliary data are required to investigate this further.

Acknowledgments

The author would like to thank the Johns Hopkins University Applied Physics Laboratory (JHUAPL) for providing the SSUSI DMSP data. The author also thanks Jürgen Matzka from Technical University of Denmark for providing Greenland fluxgate magnetometer data. Finally, the author is grateful to Dr. Xia Cai and Dr. Hyomin Kim for their valuable comments on this work and Dr. Kim and Dr. Weimer for providing useful figures.

Chapter 7

Conclusions and Future Work

7.1 Conclusions

The three proposed research objectives of this Ph.D. work were:

1. Build scintillation data analysis tools for CASES GPS receivers.
2. Develop a full 3D propagation model to simulate GPS scintillations on ground at high latitudes.
3. Solve an inverse problem to extract physics of the irregularities from high latitude regions.

These goals have been accomplished as described in detail in Chapters 2, 3 and 4, respectively. Apart from that, the AAL-PIP project which boasts some of the state-of-art space science instrumentation is described in Chapter 5. Finally, SIGMA is implemented for the case of a substorm observed by AAL-PIP, the preliminary results of which are exhibited in Chapter 6.

Initial results from a CASES GPS receiver deployed in Antarctica have been presented. We have developed and applied specialized post-processing techniques to analyze CASES high-rate data. Using CASES, we observed GPS phase scintillations during the solar storm of 24 January 2012. We then compared the CASES processed data with data from a Novatel GSV4004 GPS scintillation receiver at the South Pole, and we determined that there is a good match in phase scintillations between the two. This test proved the expediency of CASES as a scintillation monitor at high latitudes.

A new numerical model, SIGMA for the electromagnetic propagation through the random ionospheric electron density fluctuations is presented. It is a split-step model with multiple phase screens and forward propagation between the screens. SIGMA is entirely general and is applicable anywhere on the globe. The salient new features of the model are that: it handles the intricate 3D geometries at high latitudes, the extended distribution of irregularities along the field lines and the low elevation angle signal paths through the irregularities. An important advantage of SIGMA over other statistically-based scintillation simulation models is that with density structure realizations, we can achieve propagation simulations with significantly more fidelity. The sensitivity study of SIGMA helps us understand which parameters are the most sensitive (or have the most visibility) to the ground observations.

We have deduced from our sensitivity study that the peak to peak (P2P) power gets most affected by the spectral index and line of sight (LOS) direction, while the P2P phase and standard deviation of the phase (σ_ϕ) are more sensitive to the anisotropy of the irregularity. This study also revealed that the scintillation index (S4) does not show any significant dependence on any inputs at high latitudes. The sensitivity study narrows the parametric space to investigate while comparing the modeled results to the observations.

According to our knowledge, high rate GPS data have never been employed in high latitude interhemispheric studies, especially along with a model comparison. For the first time, we have used an inverse modeling technique to derive irregularity physics. The SIGMA input parameters thus derived represent the physical and propagation parameters related to the physics of the irregularity that produced those GNSS scintillations.

From our investigation of the geomagnetic storm on 9 March 2012, we found that for cases at 350 km height, the spectral index is between 2.8 to 3.6 and the outer scale is greater than 3.3 km. With 10 km irregularity thickness, the turbulence strength ranges from 0.8 TECU to 2.5 TECU. The best fits we obtained from our inverse method mostly agree with the observations, but we also report some ambiguities. We need more auxiliary data in order to facilitate

the possibility of accomplishing a unique solution to the inverse problem. We observed simultaneous scintillations occurring in conjugate auroral regions, but without sufficient auxiliary data, it is challenging to relate the irregularity physics between the two hemispheres. The technique we are using for inverse modeling is still under experimental consideration since we considered only 2 free parameters in our optimization instead of seven.

A substorm on 9 January 2014 was observed by more than one AAL-PIP station and was chosen to study the relationship between the substorm and coexisting GPS scintillations. Although, some sparse evidences and part of the results from inverse modeling indicate the possibility that the substorm is the source of the irregularities, more simultaneous observations along with sufficient auxiliary data are required to investigate this further.

We believe that an inverse modeling technique with a high fidelity propagation model such as SIGMA will be very instrumental in routinely deriving the physics of the ionospheric irregularities from GNSS observations.

7.2 Publications and Presentations

Results from this research and related topics have been presented at the CEDAR workshop [2011,2012,2013], GEM workshop [2011,2012] and AGU Fall meetings [2011,2012,2013]. The results of this work were also presented at a seminar in Indian Institute of Geomagnetism (IIG) in 2013. Of the three manuscripts included in this dissertation, one has been published in *Radio Science* [*Deshpande et al.*, 2012], another in *Journal of Geophysical Research (Space Physics)* and the last one is under preparation to be submitted to *Journal of Geophysical Research (Space Physics)*. One co-authored manuscript on a related topic [*Kim et al.*, 2014a] has been published in *Journal of Atmospheric and Solar-Terrestrial Physics (JASTP)* and the other one [*Clauer et al.*, 2014] is accepted for publication in *Geoscientific Instrumentation, Methods, and Data Systems*. Finally, one co-authored paper that utilizes the CASES post processing software [*Bust*

et al., 2013] has been published in *The Institute of Navigation (ION) proceedings*.

7.3 Recommendations for Future Work

One of the lessons learnt from our inverse modeling investigation was that we need more auxiliary data in order to obtain a realistic solution to the inverse problem. We are trying to solve a non-linear problem which has more unknowns than equations. A cluster of GPS receivers, good coverage from ISR and SuperDARN are the crucial factors to solve this kind of a problem. Additionally, we need to have a better computational power so that we can run a multi-dimensional optimization and obtain a unique solution over higher dimensional parametric space.

Some of my specific recommendations for future work are as follows:

1. Combine the modeling results from SIGMA with observations of closely-clustered arrays of GNSS scintillation receivers at high latitudes. An example of such arrays is one at Poker Flat, Alaska [*Bust et al.*, 2013].

2. Compare the irregularity physics during a storm time with that during a quiet time.

3. Utilize observations from higher number of ancillary instruments before performing an inverse modeling analysis.

4. Design a Monte Carlo simulation, that can work on a parallel cluster, to efficiently optimize more than 2 free parameters in SIGMA.

5. Obtain background number densities for SIGMA from either tomography and data assimilation algorithms such as IDA4D and MIDAS or plasma physics simulations for different instabilities.

References

Aarons, J. (1982), Global morphology of ionospheric scintillations, *IEEE Proceedings*, *70*, 360–378.

Aarons, J. (1997), Global positioning system phase fluctuations at auroral latitudes, *Journal of Geophysical Research*, *102*, 17,219–17,232, doi:10.1029/97JA01118.

Akos, D. M., P.-L. Normark, P. Enge, A. Hansson, and A. Rosenlind (2001), Real-time gps software radio receivers, in *Proceedings of the 2001 National Technical Meeting of The Institute of Navigation*, pp. 809–816, Long Beach, CA, January 2001.

Aveiro, H. C., and D. L. Hysell (2010), Three-dimensional numerical simulation of equatorial F region plasma irregularities with bottomside shear flow, *Journal of Geophysical Research (Space Physics)*, *115*, A11321, doi:10.1029/2010JA015602.

Basu, S., E. J. Weber, T. W. Bullett, M. J. Keskinen, E. MacKenzie, P. Doherty, R. Sheehan, H. Kuenzler, P. Ning, and J. Bongiolatti (1998), Characteristics of plasma structuring in the cusp/cleft region at Svalbard, *Radio Science*, *33*, 1885–1900, doi:10.1029/98RS01597.

Basu, S., K. M. Groves, S. Basu, and P. J. Sultan (2002), Specification and forecasting of scintillations in communication/navigation links: current status and future plans, *Journal of Atmospheric and Solar-Terrestrial Physics*, *64*, 1745–1754, doi:10.1016/S1364-6826(02)00124-4.

Beach, T. L. (1998), Global Positioning System studies of equatorial scintillations, Ph.D. thesis, CORNELL UNIVERSITY.

Béniguel, Y. (2002), Global Ionospheric Propagation Model (GIM): A propagation model for scintillations of transmitted signals, *Radio Science*, *37*(3), 1032, doi:10.1029/2000RS002393.

Béniguel, Y., and P. Hamel (2011), A global ionosphere scintillation propagation model for equatorial regions, *Journal of Space Weather and Space Climate*, *1*(26), A04, doi:10.1051/swsc/2011004.

Booker, H. G., J. A. Ferguson, and H. O. Vats (1985), Comparison between the extended-medium and the phase-screen scintillation theories, *Journal of Atmospheric and Terrestrial Physics*, *47*, 381–399.

Bust, G., S. Datta-Barua, K. Deshpande, S. Bourand, S. Skone, and Y. Su (2013), Correlation properties of a 2-d array of high latitude scintillation receivers, in *Proceedings of the 26th International Technical Meeting of The Satellite Division of the Institute of Navigation (ION GNSS 2013)*, pp. 2470–2479, Nashville, TN, September 2013.

Bust, G. S., T. W. Garner, and T. L. Gaussiran (2004), Ionospheric Data Assimilation Three-Dimensional (IDA3D): A global, multisensor, electron density specification algorithm, *Journal of Geophysical Research (Space Physics)*, *109*, A11312, doi:10.1029/2003JA010234.

Carrano, C. S., K. M. Groves, R. G. Caton, C. L. Rino, and P. R. Straus (2011), Multiple phase screen modeling of ionospheric scintillation along radio occultation raypaths, *Radio Science*, *46*, RS0D07, doi:10.1029/2010RS004591.

Carrano, C. S., K. M. Groves, and R. G. Caton (2012a), Simulating the impacts of ionospheric scintillation on L band SAR image formation, *Radio Science*, *47*, 0, doi:10.1029/2011RS004956.

Carrano, C. S., C. E. Valladares, and K. M. Groves (2012b), Latitudinal and local time variation of ionospheric turbulence parameters during the conjugate point equatorial experiment in brazil, *International Journal of Geophysics*, *2012*(Article ID 103963), 16 pages, doi:10.1155/2012/103963.

Chernoff, H., and E. L. Lehmann (1954), The use of maximum likelihood estimates in ÏĞ2 tests for goodness of fit, *The Annals of Mathematical Statistics*, *25(3)*, 579–586, doi:10.1214/aoms/1177728726.

Clauer, C. R., H. Kim, K. B. Deshpande, Z. Xu, D. Weimer, S. B. Musko, G. Crowley, F. Chad, R. Nealy, T. E. Humphreys, and J. A. Bhatti (2014), Autonomous Adaptive Low-Power Instrument Platform (AAL-PIP) for remote high latitude geospace data collection, *Geosci. Instrum. Method. Data Syst. Discuss.*, *4*, 271–317, doi:10.5194/gid-4-271-2014.

Coker, C., R. Hunsucker, and G. Lott (1995), Detection of auroral activity using GPS satellites, *Geophysical Research Letters*, *22*, 3259–3262, doi:10.1029/95GL03091.

Costa, E., and S. Basu (2002), A radio wave scattering algorithm and irregularity model for scintillation predictions, *Radio Science*, *37*(3), 1046, doi:10.1029/2001RS002498.

Costa, E., and M. C. Kelley (1977), Ionospheric scintillation calculations based on in situ irregularity spectra, *Radio Science*, *12*, 797–809, doi:10.1029/RS012i005p00797.

Coster, A., S. Skone, C. Mitchell, G. De Franceschi, L. Alfonso, and V. Romano (2005), Global studies of gps scintillation, in *Proceedings of the 2005 National Technical Meeting of The Institute of Navigation*, pp. 1130–1139, San Diego, CA, January 2005.

Crowley, G., G. Bust, A. Reynolds, I. Azeem, R. Wilder, B. W. O'Hanlon, M. L. Psiaki, S. Powell, T. E. Humphreyes, and J. A. Bhatti (2011), Cases: A novel low-cost ground-based dual-frequency gps software receiver and space weather monitor, in *Proceedings of the 24th International Technical Meeting of The Satellite Division of the Institute of Navigation (ION GNSS 2011)*, pp. 1437–1446, Portland, OR, September 2011.

Deshpande, K. B., G. S. Bust, C. R. Clauer, H. Kim, J. E. Macon, T. E. Humphreys, J. A. Bhatti, S. B. Musko, G. Crowley, and A. T. Weatherwax (2012), Initial GPS Scintillation results from CASES receiver at South Pole, Antarctica, *Radio Science*, *47*, RS5009, doi:10.1029/2012RS005061.

Deshpande, K. B., G. S. Bust, C. R. Clauer, C. L. Rino, and C. S. Carrano (2014), Satellite-beacon Ionospheric-scintillation Global Model of the upper Atmosphere (SIGMA) I: High latitude sensitivity study of the model parameters, *Journal of Geophysical Research (Space Physics)*, *119*, 4026–4043, doi:10.1002/2013JA019699.

Dyson, P. L., J. P. McClure, and W. B. Hanson (1974), In situ measurements of the spectral characteristics of F region ionospheric irregularities, *Journal of Geophysical Research*, *79*, 1497, doi:10.1029/JA079i010p01497.

Forte, B., and S. M. Radicella (2002), Problems in data treatment for ionospheric scintillation measurements, *Radio Science*, *37*, 1096, doi:10.1029/2001RS002508.

Fremouw, E. J., and J. A. Secan (1984), Modeling and scientific application of scintillation results, *Radio Science*, *19*, 687–694, doi:10.1029/RS019i003p00687.

Gablonsky, J., and C. Kelley (2001), A locally-biased form of the direct algorithm, *Journal of Global Optimization*, *21*(1), 27–37, doi:10.1023/A:1017930332101.

Ganguly, S., A. Jovancevic, A. Brown, M. Kirchner, S. Zigic, T. Beach, and K. M. Groves (2004), Ionospheric scintillation monitoring and mitigation using a software GPS receiver, *Radio Science*, *39*, RS1S21, doi:10.1029/2002RS002812.

Ghafoori, F. (2012), Modeling the impact of equatorial ionospheric irregularities on gps receiver performance, Ph.D. thesis, Dept. of Geomatics Engineering, Univ. of Calgary, Calgary, Alberta, Canada.

Gherm, V. E., N. N. Zernov, S. M. Radicella, and H. J. Strangeways (2000), Propagation model for signal fluctuations on transionospheric radio links, *Radio Science*, *35*, 1221–1232, doi:10.1029/1999RS002301.

Gherm, V. E., N. N. Zernov, and H. J. Strangeways (2005a), Propagation model for transionospheric fluctuating paths of propagation: Simulator of the transionospheric channel, *Radio Science*, *40*, RS1003, doi:10.1029/2004RS003097.

Gherm, V. E., N. N. Zernov, and H. J. Strangeways (2005b), HF propagation in a wideband ionospheric fluctuating reflection channel: Physically based software simulator of the channel, *Radio Science*, *40*, RS1001, doi:10.1029/2004RS003093.

Gola, M., A. W. Wernik, S. J. Franke, C. H. Liu, and K. C. Yeh (1992), Behaviour of HILAT scintillation over Spitsbergen, *Journal of Atmospheric and Terrestrial Physics*, *54*, 1207–1213.

Gondarenko, N. A., and P. N. Guzdar (2001), Three-dimensional structuring characteristics of high-latitude plasma patches, *Journal of Geophysical Research*, *106*, 24,611–24,620, doi:10.1029/2000JA000440.

Gondarenko, N. A., and P. N. Guzdar (2003), Structure of Turbulent Irregularities in High-Latitude Plasma Patches-3D Nonlinear Simulations, in *Disturbances in Geospace: The Storm-substorm Relationship*, *Washington DC American Geophysical Union Geophysical Monograph*

Series, vol. 142, edited by A. Surjalal Sharma, Y. Kamide, and G. S. Lakhina, p. 205, doi:10.1029/142GM17.

Gondarenko, N. A., and P. N. Guzdar (2006), Nonlinear three-dimensional simulations of mesoscale structuring by multiple drives in high-latitude plasma patches, *Journal of Geophysical Research (Space Physics)*, *111*, A08302, doi:10.1029/2006JA011701.

Grimault, C. (1998), A multiple phase screen technique for electromagnetic wave propagation through random ionospheric irregularities, *Radio Science*, *33*, 595–606, doi:10.1029/97RS03552.

Hones, E. W., Jr. (1984), Plasma sheet behavior during substorms, *Washington DC American Geophysical Union Geophysical Monograph Series*, *30*, 178–184, doi:10.1029/GM030p0178.

Humphreys, T. E., M. L. Psiaki, and P. M. Kintner (2010), Modeling the Effects of Ionospheric Scintillation on GPS Carrier Phase Tracking, *IEEE Transactions on Aerospace Electronic Systems*, *46*, 1624–1637, doi:10.1109/TAES.2010.5595583.

Jayachandran, P. T., R. B. Langley, J. W. MacDougall, S. C. Mushini, D. Pokhotelov, A. M. Hamza, I. R. Mann, D. K. Milling, Z. C. Kale, R. Chadwick, T. Kelly, D. W. Danskin, and C. S. Carrano (2009), Canadian High Arctic Ionospheric Network (CHAIN), *Radio Science*, *44*, RS0A03, doi:10.1029/2008RS004046.

Jones, D. R., C. D. Perttunen, and B. E. Stuckman (1993), Lipschitzian optimization without the lipschitz constant, *J. Optim. Theory Appl.*, *79*(1), 157–181, doi:10.1007/BF00941892.

Keskinen, M. J. (2006), GPS scintillation channel model for the disturbed low-latitude ionosphere, *Radio Science*, *41*, RS4003, doi:10.1029/2005RS003442.

Keskinen, M. J., H. G. Mitchell, J. A. Fedder, P. Satyanarayana, and S. T. Zalesak (1988), Nonlinear evolution of the Kelvin-Helmholtz instability in the high-latitude ionosphere, *Journal of Geophysical Research*, *93*, 137–152, doi:10.1029/JA093iA01p00137.

Keskinen, M. J., S. L. Ossakow, and B. G. Fejer (2003), Three-dimensional nonlinear evolution of equatorial ionospheric spread-F bubbles, *Geophysical Research Letters*, *30*, 1855, doi:10.1029/2003GL017418.

Keskinen, M. J., S. L. Ossakow, B. G. Fejer, and J. Emmert (2006), Evolution of equatorial ionospheric bubbles during a large auroral electrojet index increase in the recovery phase of a magnetic storm, *Journal of Geophysical Research (Space Physics)*, *111*, A02303, doi:10.1029/2005JA011352.

Kim, H., C. Clauer, K. Deshpande, M. Lessard, A. Weatherwax, G. Bust, G. Crowley, and T. Humphreys (2014a), Ionospheric irregularities during a substorm event: Observations of ULF pulsations and GPS scintillations, *Journal of Atmospheric and Solar-Terrestrial Physics*, *114*(0), 1 – 8, doi:http://dx.doi.org/10.1016/j.jastp.2014.03.006.

Kim, H., C. Clauer, M. Engebreton, J. Matzka, D. Sibeck, H. Singer, C. Stolle, D. Weimer, and Z. Xu (2014b), Conjugate observations of traveling convection vortices associated with transient events at the magnetopause, *Journal of Geophysical Research*, *Manuscript under preparation*.

Kinrade, J., C. N. Mitchell, P. Yin, N. Smith, M. J. Jarvis, D. J. Maxfield, M. C. Rose, G. S. Bust, and A. T. Weatherwax (2012), Ionospheric scintillation over Antarctica during the storm of 5-6 April 2010, *Journal of Geophysical Research (Space Physics)*, *117*, A05304, doi:10.1029/2011JA017073.

Kinrade, J., C. N. Mitchell, N. D. Smith, Y. Ebihara, A. T. Weatherwax, and G. S. Bust (2013), GPS phase scintillation associated with optical auroral emissions: First statistical results from the geographic South Pole, *Journal of Geophysical Research (Space Physics)*, *118*, 2490–2502, doi:10.1002/jgra.50214.

Kintner, P. M., B. M. Ledvina, E. R. de Paula, and I. J. Kantor (2004), Size, shape, orientation, speed, and duration of GPS equatorial anomaly scintillations, *Radio Science*, *39*, RS2012, doi:10.1029/2003RS002878.

Kintner, P. M., B. M. Ledvina, and E. R. de Paula (2007), GPS and ionospheric scintillations, *Space Weather*, *5*, S09003, doi:10.1029/2006SW000260.

Knepp, D. L. (1983), Multiple phase-screen calculation of the temporal behavior of stochastic waves, *IEEE Proceedings*, *71*, 722–737.

Knepp, D. L., and L. J. Nickisch (2009), Multiple phase screen calculation of wide bandwidth propagation, *Radio Science*, *44*, RS0A09, doi:10.1029/2008RS004054.

Machol, J. L., J. C. Green, R. J. Redmon, R. A. Viereck, and P. T. Newell (2012), Evaluation of ovation prime as a forecast model for visible aurorae, *Space Weather*, *10*, S03005, doi: 10.1029/2011SW000746.

Maurits, S. A., V. E. Gherm, N. N. Zernov, and H. J. Strangeways (2008), Modeling of scintillation effects on high-latitude transionospheric paths using ionospheric model (UAF EPPIM) for background electron density specifications, *Radio Science*, *43*, RS4001, doi: 10.1029/2006RS003539.

Mitchell, C. N., L. Alfonsi, G. De Franceschi, M. Lester, V. Romano, and A. W. Wernik (2005), GPS TEC and scintillation measurements from the polar ionosphere during the October 2003 storm, *Geophysical Research Letters*, *32*, L12S03, doi:10.1029/2004GL021644.

Musko, S. B., C. R. Clauer, A. J. Ridley, and K. L. Arnett (2009), Autonomous low-power magnetic data collection platform to enable remote high latitude array deployment, *Review of Scientific Instruments*, *80*(4), 044501, doi:10.1063/1.3108527.

Nelder, J. A., and R. Mead (1965), A simplex method for function minimization, *Computer Journal*, *7*, 308–313.

Newell, P. T., T. Sotirelis, and S. Wing (2009), Diffuse, monoenergetic, and broadband aurora: The global precipitation budget, *Journal of Geophysical Research (Space Physics)*, *114*, A09207, doi:10.1029/2009JA014326.

Ngwira, C. M., L.-A. McKinnell, and P. J. Cilliers (2010), GPS phase scintillation observed over a high-latitude Antarctic station during solar minimum, *Journal of Atmospheric and Solar-Terrestrial Physics*, *72*, 718–725, doi:10.1016/j.jastp.2010.03.014.

O'Hanlon, B. W., M. L. Psiaki, S. Powell, J. A. Bhatti, T. E. Humphreys, G. Crowley, and G. S. Bust (2011), Cases: A smart, compact gps software receiver for space weather monitoring, in *Proceedings of the 24th International Technical Meeting of The Satellite Division of the Institute of Navigation (ION GNSS 2011)*, pp. 2745–2753, Portland, OR, September 2011.

Press, W., B. Flannery, S. Teukolsky, and W. Vetterling (1992), *Numerical Recipes in C: The Art of Scientific Computing*, Cambridge University Press.

Prikryl, P., P. T. Jayachandran, S. C. Mushini, D. Pokhotelov, J. W. MacDougall, E. Donovan, E. Spanswick, and J.-P. St.-Maurice (2010), GPS TEC, scintillation and cycle slips observed at high latitudes during solar minimum, *Annales Geophysicae*, *28*, 1307–1316, doi:10.5194/angeo-28-1307-2010.

Prikryl, P., L. Spogli, P. T. Jayachandran, J. Kinrade, C. N. Mitchell, B. Ning, G. Li, P. J. Cilliers, M. Terkildsen, D. W. Danskin, E. Spanswick, E. Donovan, A. T. Weatherwax, W. A. Bristow, L. Alfonsi, G. de Franceschi, V. Romano, C. M. Ngwira, and B. D. L. Opperman (2011), Interhemispheric comparison of GPS phase scintillation at high latitudes during the magnetic-cloud-induced geomagnetic storm of 5-7 April 2010, *Annales Geophysicae*, *29*, 2287–2304, doi:10.5194/angeo-29-2287-2011.

Prikryl, P., P. T. Jayachandran, S. C. Mushini, and I. G. Richardson (2012), Toward the probabilistic forecasting of high-latitude GPS phase scintillation, *Space Weather*, *10*, S08005, doi:10.1029/2012SW000800.

Prikryl, P., Y. Zhang, Y. Ebihara, R. Ghoddousi-Fard, P. T. Jayachandran, J. Kinrade, C. N. Mitchell, A. T. Weatherwax, G. Bust, P. J. Cilliers, et al. (2013), An interhemispheric comparison of gps phase scintillation with auroral emission observed at the south pole and from the dmsp satellite, *Annals of Geophysics*, *56*(2), R0216.

Rino, C. L. (1979), A power law phase screen model for ionospheric scintillation. I - Weak scatter., *Radio Science*, *14*, 1135–1145, doi:10.1029/RS014i006p01135.

Rino, C. L. (2010), *The Theory of Scintillation with Applications in Remote Sensing*, John Wiley & Sons.

Rino, C. L., and C. S. Carrano (2011), The application of numerical simulations in Beacon scintillation analysis and modeling, *Radio Science*, *46*, RS0D02, doi:10.1029/2010RS004563.

Rufenach, C. L. (1975), Ionospheric scintillation by a random phase screen Spectral approach, *Radio Science*, *10*, 155–165, doi:10.1029/RS010i002p00155.

Ruohoniemi, J. M., and K. B. Baker (1998), Large-scale imaging of high-latitude convection with Super Dual Auroral Radar Network HF radar observations, *Journal of Geophysical Research*, *103*, 20,797–20,811, doi:10.1029/98JA01288.

Russell, C. T., and R. L. McPherron (1973), The Magnetotail and Substorms, *Space Science Review*, *15*, 205–266, doi:10.1007/BF00169321.

Scott, D. W. (1979), On optimal and data-based histograms, pp. 605–610.

Secan, J. A., R. M. Bussey, E. J. Fremouw, and S. Basu (1995), An improved model of equatorial scintillation, *Radio Science*, *30*, 607–618, doi:10.1029/94RS03172.

Secan, J. A., R. M. Bussey, E. J. Fremouw, and S. Basu (1997), High-latitude upgrade to the Wideband ionospheric scintillation model, *Radio Science*, *32*, 1567–1574, doi:10.1029/97RS00453.

Shkarofsky, I. P. (1968), Generalized turbulence space-correlation and wave-number spectrum-function pairs, *Canadian Journal of Physics*, *46*, 2133, doi:10.1139/p68-562.

Skone, S., and M. Cannon (1999), Ionospheric effects on differential {GPS} applications during auroral substorm activity, *{ISPRS} Journal of Photogrammetry and Remote Sensing*, *54*(4), 279 – 288, doi:http://dx.doi.org/10.1016/S0924-2716(99)00017-9.

Skone, S., and M. De Jong (2000), The impact of geomagnetic substorms on gps receiver performance, *EARTH PLANETS AND SPACE*, *52*(11), 1067–1072.

Skone, S., and K. Knudsen (2000), Impact of ionospheric scintillations on sbas performance, in *Proceedings of the 13th International Technical Meeting of the Satellite Division of The Institute of Navigation (ION GPS 2000)*, pp. 284–293, Salt Lake City, UT, September 2000.

Skone, S., G. Lachapelle, D. Yao, W. Yu, and R. Watson (2005), Investigating the impact of ionospheric scintillation using a gps software receiver, in *Proceedings of the 18th International Technical Meeting of the Satellite Division of The Institute of Navigation (ION GNSS 2005)*, pp. 1126–1137, Long Beach, CA, September 2005.

Smith, A. M., C. N. Mitchell, R. J. Watson, R. W. Meggs, P. M. Kintner, K. Kauristie, and F. Honary (2008), GPS scintillation in the high arctic associated with an auroral arc, *Space Weather*, *6*, S03D01, doi:10.1029/2007SW000349.

Spencer, P. S. J., and C. N. Mitchell (2007), Imaging of fast moving electron-density structures in the polar cap, *Annales Geophysicae*, *50*, 427–434.

Spogli, L., L. Alfonsi, G. de Franceschi, V. Romano, M. H. O. Aquino, and A. Dodson (2009), Climatology of GPS ionospheric scintillations over high and mid-latitude European regions, *Annales Geophysicae*, *27*, 3429–3437, doi:10.5194/angeo-27-3429-2009.

Spogli, L., L. Alfonsi, P. J. Cilliers, E. Correia, G. De Franceschi, C. N. Mitchell, V. Romano, J. Kinrade, and M. A. Cabrera (2013), Gps scintillations and total electron content climatology in the southern low, middle and high latitude regions, *Annals of Geophysics*, *56*(2), R0220.

Strangeways, H. J. (2009), Determining scintillation effects on GPS receivers, *Radio Science*, *44*, RS0A36, doi:10.1029/2008RS004076.

Strangeways, H. J., Y.-H. Ho, M. H. O. Aquino, Z. G. Elmas, H. A. Marques, J. F. G. Monico, and H. A. Silva (2011), On determining spectral parameters, tracking jitter, and GPS positioning improvement by scintillation mitigation, *Radio Science*, *46*, RS0D15, doi: 10.1029/2010RS004575.

Van Dierendonck, A. J., and Q. Hua (2001), Measuring ionospheric scintillation effects from gps signals, in *Proceedings of the 57th Annual Meeting of The Institute of Navigation*, pp. 391–396, Albuquerque, NM, June 2001.

Van Dierendonck, A. J., J. Klobuchar, and Q. Hua (1993), Ionospheric scintillation monitoring using commercial single frequency c/a code receivers, in *Proceedings of the 6th International Technical Meeting of the Satellite Division of The Institute of Navigation (ION GPS 1993)*, pp. 1333–1342, Salt Lake City, UT, September 1993.

Welch, P. D. (1967), The use of fast fourier transform for the estimation of power spectra: A method based on time averaging over short, modified periodograms, *Audio and Electroacoustics, IEEE Transactions on*, *15*(2), 70–73, doi:10.1109/TAU.1967.1161901.

Wernik, A. W., M. Gola, C. H. Liu, and S. J. Franke (1990), High-latitude irregularity spectra deduced from scintillation measurements, *Radio Science*, *25*, 883–895, doi: 10.1029/RS025i005p00883.

Wernik, A. W., J. A. Secan, and E. J. Fremouw (2003), Ionospheric irregularities and scintillation, *Advances in Space Research*, *31*, 971–981, doi:10.1016/S0273-1177(02)00795-0.

Wernik, A. W., L. Alfonsi, and M. Materassi (2007), Scintillation modeling using in situ data, *Radio Science*, *42*, RS1002, doi:10.1029/2006RS003512.

Yeh, K. C., and C.-H. Liu (1982), Radio wave scintillations in the ionosphere, *IEEE Proceedings*, *70*, 324–360.

Appendix A

Simulation Procedure and Setup of SIGMA

In this appendix, we describe a numerical simulation of SIGMA presented in Section 3.2. Following are the steps involved in our simulation procedure to obtain the GPS signal on ground as it traverses through an ionospheric irregularity.

1. Divide an irregularity with a certain thickness (L_{th}) into N layers, making sure the z-dimension of number density ΔN_e is greater than or equal to N.

2. Generate PSD using Equation 3.1 and the coordinate transformation to a reference coordinate system defined in Section 3.2.1. Obtain 3D number density using Equation 3.3.

3. If satellite motion is desired, at each time instance, compute the incidence angle θ which is equal to the elevation angle for a satellite position; otherwise elevation and azimuth values remain the same.

4. Obtain the spatial phase and the electric field at the bottom of irregularity using Equations 3.4 and 3.5, respectively, from Section 3.2.2.

5. Using Equation 3.8 from Section 3.2.3 generate the propagated field and use it as an incident field for the next layer or to propagate to ground.

6. Repeat steps 4 to 5 until the field is propagated to ground.

7. Find the propagated field at a given time instance by moving through the 2D propagated field map with the help of Equations 3.11.

8. Repeat steps 3 to 7 until all the satellite positions and the respective time stamps are covered.

In the above procedure, steps 4 and 5 together represent the split-step method. Figure A.1 displays the flowchart summarizing the simulation procedure.

The input and output parameters of SIGMA are described below. The model depends on eight different physical and propagation parameters. Physical parameters characterize an ionospheric irregularity and include the outer scale l_0, RMS electron number density ΔN, spectral index p, and anisotropy of the irregularity spectrum defined by an axial ratio. The propagation parameters consist of altitude H_{iono}, thickness of the irregularity L_{th}, number of layers N_l and drift velocity $v_d = [v_x, v_y]$ which could be parallel or perpendicular to LOS vector. Finally, the SIGMA expects geographical parameters as input. These include the receiver, satellite locations in ECEF coordinates or simply the azimuth and elevation angles of the LOS vector, and the dip angle at the receiver location. The receiver and satellite locations are converted into local coordinate systems that are in reference coordinates shown in Figure 3.3.

The inner scale or the smallest spatial dimension of the irregularity structure is governed by the computation time for a simulation. A typical spatial resolution of 50 m to 200 m is considered in our simulations. The sampling frequency is taken to be 10 Hz or 20 Hz for a 30 s to 60 s long time series. These are suitable for a sensitivity study where a plethora of simulation runs are explored.

An ideal case would be with a spatial resolution of 10 m or 20 m and 50 Hz sampling for 120 s long time series. The sampling frequency of 50 Hz would generate a sample size similar to the actual observations from a GPS scintillation monitor. But, this ideal case demands a lot of computation time and resources, more suitable for a hand-picked simulation runs.

As an example, using Figure 3.3 and a coordinate transformation given by the following three equations applicable in Southern hemisphere, we can transform the the Hybrid spectrum

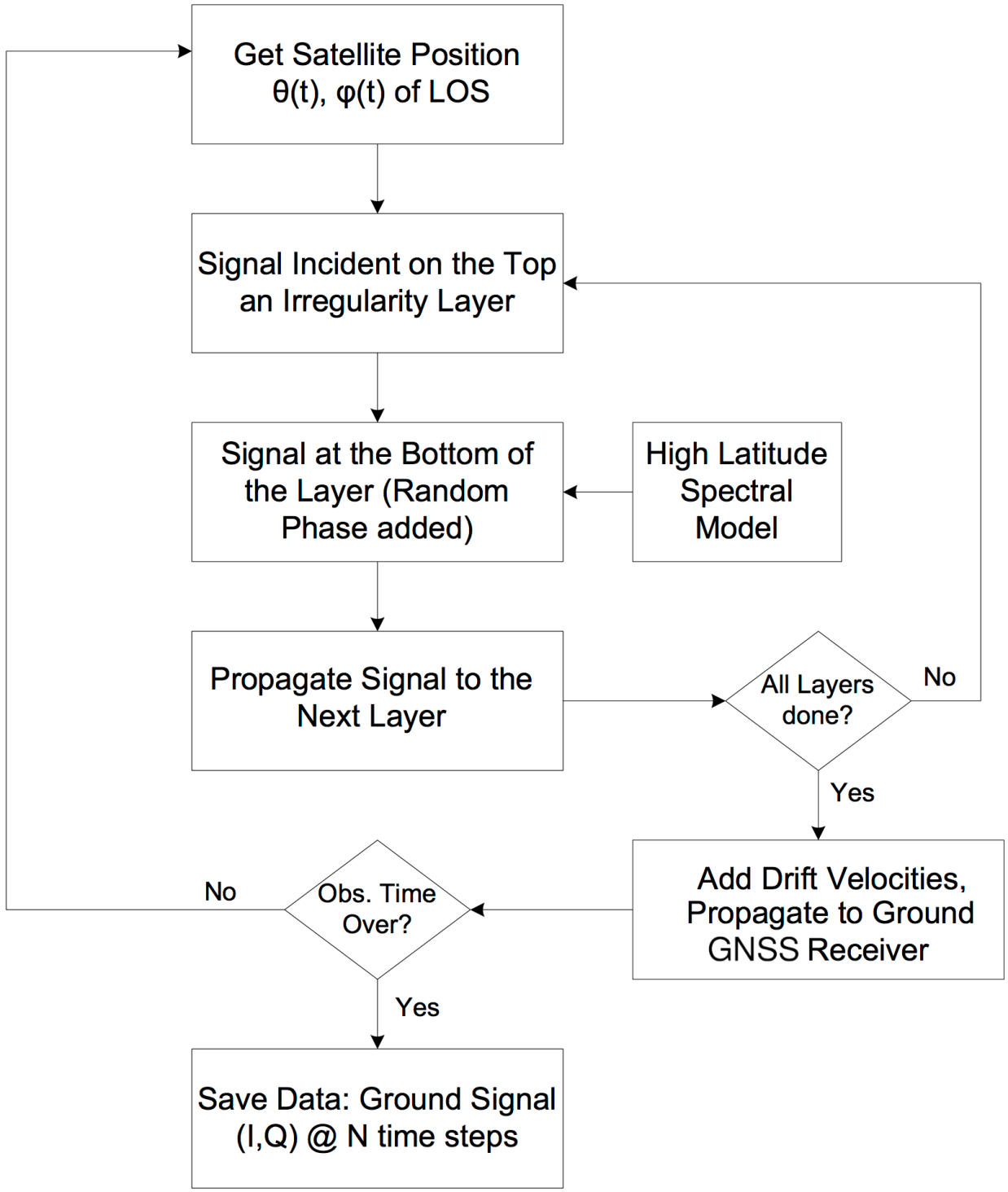

Figure A.1: Flowchart summarizing the different steps in SIGMA that takes the signal from a GPS satellite as an input and determines the signal received on ground after it traverses through an ionospheric irregularity with certain thickness, drift velocity etc.

to the local reference frame.

$$k'_x = k_x, \tag{A.1}$$

$$k'_y = k_y \sin I + k_z \cos I, \tag{A.2}$$

$$k'_z = -k_y \cos I + k_z \sin I. \tag{A.3}$$

The hybrid spectrum in the local reference frame is given as:

$$P_{NH}(k_x, k_y, k_z) = \frac{a(\gamma_H - 2)}{2\pi^{3/2} k_0^2} \, \Delta N^2 \left(1 + \frac{N_{H1}}{k_0^2}\right)^{-\gamma_H/2} \exp\left(-(ak_0)^2 \frac{N_{H2}}{k_0^2}\right), \tag{A.4}$$

where the numerators N_{H1} and N_{H2} are given as:

$$N_{H1} = k_x^2 + k_y^2 \sin^2 I + k_z^2 \cos^2 I + k_y k_z \sin 2I, \tag{A.5}$$

$$N_{H2} = k_y^2 \cos^2 I + k_z^2 \sin^2 I - k_y k_z \sin 2I. \tag{A.6}$$

As described in Section 3.2, an irregularity is divided in N_l layers or random phase screens representing random phase fluctuations pertaining to each layer. At the beginning of our simulation, we generate a random realization of the 3D number density from statistically independent random phase varying between 0 to 2π using equation 3.3 and then determine the number density for shifted coordinates using periodicity as described in Section 3.2.2. While propagating a signal through the irregularity at different time instances using the split step method, the phase at the bottom of every layer is computed at each time instance.

The satellite positions are found out from orbital data recorded in *.sp3* files available on the Scripps Orbit and Permanent Array Center (SOPAC) GPS orbit database. The orbital parameters listed for a particular satellite on a given day are 900 seconds apart. The orbital period of a GPS satellite is 11 hours 58 minutes. The 900 second period is small enough compared to the orbital period to assume a linear orbit during that time. Thus, the satellite

position data is linearly interpolated to obtain higher resolution data to satisfy the 50 Hz sampling frequency requirement. We expect that these interpolated values are close to the actual satellite positions.

Appendix B

Relationship between Spatial Phase and Number Density

From *Rino* [2010], page 50, refractive index of the plasma can be found from cold plasma approximation (since EM wave frequencies in ionosphere $\gg$ plasma frequency):

$$n_p = \sqrt{1 - \frac{\omega_p^2}{\omega^2}} \tag{B.1}$$

With Taylor series expansion:

$$n_p = 1 - \frac{\omega_p^2}{2\omega^2} \tag{B.2}$$

where the plasma frequency is given by:

$$\omega_p^2 = \frac{N_e e^2}{\epsilon_0 m_e} = 4\pi r_e c^2 N_e \tag{B.3}$$

We can get the refractive index fluctuation (or deviation from the mean value) by taking the derivative of refractive index equation (with respect to x, dx is not written explicitly here):

$$\delta n_p = -\frac{2\pi r_e c^2}{\omega^2} \delta N_e \tag{B.4}$$

$$\delta n_p = -\frac{2\pi r_e}{k^2}\delta N_e$$

Equation (4.8) from page 104: $\delta\phi = k\sec\theta\int\delta n_p(\eta, \vec{\rho}+\tan\theta\,\widehat{a}_\perp\,\eta)d\eta$, we get the phase deviation due to electron deviation across a slab from z to z-L at an oblique angle θ as:

$$\delta\phi(\vec{\rho};z,L,\theta,\hat{a}) \;=\; -\lambda r_e\sec\theta\int_z^{z-L}\delta N(\vec{\rho}+\tan\theta\,\widehat{a}_\perp\,z',z')dz' \tag{B.5}$$

The factor of 2 from Rino's equations is dropped here to be consistent with equation (3.9) from *Yeh and Liu* [1982] which gives a relation between phase and vertical TEC ($\Delta N_T(\vec{\rho})$). It is uncertain why there is a difference between Rino's and Yeh-Liu's constant (factor of 2). One possibility is it could be from confusion between refractive index and permittivity.

Appendix C

AAL-PIP Daily Downloading and Housekeeping Alert Codes

This section lists the codes written in Python to send email alerts about missing files in downloaded data, battery temperatures and voltages for all AAL-PIP systems. *CheckAlert.py* checks the files and housekeeping data and calls *AlertFunction.py* to send email alerts.

CheckAlert.py

```
#! /usr/bin/python

import os
import time
import datetime

import fnmatch

#temp check
import csv
import gzip

# Our emailing function is pulled in here
from AlertFunction import EmailAlertCall

MainDir = "/home/aal-pip/ops/aal-pip/data/"

Systems = [3,4,5,6,2]

# Stations setting in 2013-14 season
options = {'2' : 'Sys2',
       '3' : 'Sys3',
       '4' : 'PG2',
           '5' : 'PG3',
           '6' : 'PG4',
}
```

```
subfolders = ['cases','sc','hskp','fg','hf']

# flag to tell if there was any missing folder for any system
flag = 0;

# New email text initialize
text_send_mail = ''

dd = datetime.datetime.now() - datetime.timedelta(days=1)
YY = dd.strftime("%Y")

dd = dd.strftime("%Y_%m_%d")

MainDir = MainDir + YY + '/'

print 'Date: ' + dd

# Check missing data in all subsystems for systems 3 to 6
for sys in range(0, len(Systems)-1):
        SysDir = MainDir + "sys_" + str(Systems[sys])
    Messg = 'AAL-PIP STATION: ' + options[str(Systems[sys])]
        flag = 1
        print Messg
    text_send_mail = text_send_mail + Messg + '\n'
    for subf in range(0, len(subfolders)):
        SubDirPath = SysDir + '/' + subfolders[subf]
        #print SubDirPath
        d2 = SubDirPath + '/' + dd
        #print d2
        # If the directory is missing, send missing data message:
        if not os.path.exists(d2):
            Messg = 'Missing '+str(dd)+' data in : ' "sys_" +
str(Systems[sys]) + '/' + subfolders[subf]
            flag = 1
            print Messg
            text_send_mail = text_send_mail + Messg + '\n'
    text_send_mail = text_send_mail + '\n'

# Check missing data in HSKP and FG subsystems for system 2
sys = len(Systems)-1
SysDir = MainDir + "sys_" + str(Systems[sys])
Messg = 'AAL-PIP STATION: ' + options[str(Systems[sys])]
flag = 1
print Messg
text_send_mail = text_send_mail + Messg + '\n'
for subf in range(len(subfolders)-3, len(subfolders)-1):
    #print subf
    SubDirPath = SysDir + '/' + subfolders[subf]
        #print SubDirPath
    d2 = SubDirPath + '/' + dd
        #print d2
    # If the directory is missing, send missing data message:
    if not os.path.exists(d2):
```

```
        Messg = 'Missing '+str(dd)+' data in : ' "sys_" +
str(Systems[sys]) + '/' + subfolders[subf]
            flag = 1
            print Messg
            text_send_mail = text_send_mail + Messg + '\n'

print ' '
print ' '

text_send_mail = text_send_mail + '\n'
text_send_mail = text_send_mail + '\n'


# State how many files should generally be there
text_send_mail = text_send_mail + 'Expected Daily Number of Files in HSKP,
FG and HF:\n'
text_send_mail = text_send_mail + 'FG -> 24\n'
text_send_mail = text_send_mail + 'HSKP -> 24\n'
text_send_mail = text_send_mail + 'HF -> 12\n'

text_send_mail = text_send_mail + '\n'

# Find number of files (.dat) in all subsystems except HF (.txt files)
# in Systems 3,4,5,6
for subf in range(0, len(subfolders)-1):
        SubDirPath = SysDir + '/' + subfolders[subf]
    for sys in range(0, len(Systems)-1):
            SysDir = MainDir + "sys_" + str(Systems[sys])
                SubDirPath = SysDir + '/' + subfolders[subf]
                #print SubDirPath
                d2 = SubDirPath + '/' + dd
                #print d2
                #Send number of files in data message:
                if os.path.exists(d2):
                        file_count = len(fnmatch.filter(os.listdir(d2), '*.dat*'))
            Messg = '# Files on '+str(dd)+' in ' + options[str(Systems[sys])] + ' : ' + "sys
subfolders[subf] + '  =  ' + str(file_count)
                        flag = 1
            print Messg
                        text_send_mail = text_send_mail + Messg + '\n'
    text_send_mail = text_send_mail + '\n'
    print ' '

# Find number of files in HSKP and FG subsystems in System 2
sys = len(Systems)-1
SysDir = MainDir + "sys_" + str(Systems[sys])
for subf in range(len(subfolders)-1, len(subfolders)-4,-1):
    SubDirPath = SysDir + '/' + subfolders[subf]
        #print SubDirPath
    d2 = SubDirPath + '/' + dd
        #print d2
    #Send number of files in data message:
    if os.path.exists(d2):
```

```
        file_count = len(fnmatch.filter(os.listdir(d2), '*.dat*'))
            Messg = '# Files on '+str(dd)+' in ' + options[str(Systems[sys])] +
' : ' + "sys_" + str(Systems[sys]) + '/' + subfolders[subf] +
'  =  ' + str(file_count)
        flag = 1
            print Messg
            text_send_mail = text_send_mail + Messg + '\n'

text_send_mail = text_send_mail + '\n'
print ' '

# Find number of files in HF subsystem in Systems 3,4,5,6
subf = len(subfolders)-1
SubDirPath = SysDir + '/' + subfolders[subf]
for sys in range(0, len(Systems)-1):
    SysDir = MainDir + "sys_" + str(Systems[sys])
        SubDirPath = SysDir + '/' + subfolders[subf]
        #print SubDirPath
        d2 = SubDirPath + '/' + dd
        #print d2
        #Send number of files in data message:
        if os.path.exists(d2):
            file_count = len(fnmatch.filter(os.listdir(d2), '*.txt*'))
            Messg = '# Files on '+str(dd)+' in ' + options[str(Systems[sys])] +
' : ' + "sys_" + str(Systems[sys]) + '/' + subfolders[subf] +
'  =  ' + str(file_count)
            flag = 1
            print Messg
            text_send_mail = text_send_mail + Messg + '\n'

text_send_mail = text_send_mail + '\n'
print ' '


# Housekeeping only, for battery temperature
Systems = [2,3,4,5,6]

subfolders = ['hskp']


# Check housekeeping temperature for systems 2 to 6
for sys in range(0, len(Systems)):
        SysDir = MainDir + "sys_" + str(Systems[sys])
    for subf in range(0, len(subfolders)):
        SubDirPath = SysDir + '/' + subfolders[subf]
        #print SubDirPath
        d2 = SubDirPath + '/' + dd
        #print d2
        # If the directory is missing, send missing data message:
        if not os.path.exists(d2):
            Messg = 'Missing '+str(dd)+' data in ' + options[str(Systems[sys])] + ' : ' +
"sys_" + str(Systems[sys]) +
'/' + subfolders[subf]
```

```
            flag = 1
            print Messg
            text_send_mail = text_send_mail + Messg + '\n'
        else:
            flag = 1;
            filelist = os.listdir(d2)
            #print filelist
            csvfile = d2 + '/' + filelist[1]
            #print csvfile
            f = gzip.open(csvfile, 'rb')
            reader = csv.reader(f)
            headers = reader.next()
            #print headers
            column = {}
            for h in headers:
                    column[h] = []
            #To get your numeric values into floats
            converters = [str.strip] + [float] * (len(headers) - 1)
            for row in reader:
                for h, v, conv in zip(headers, row, converters):
                    column[h].append(conv(v))
            tbat = column['T_batt_1']
            Messg = 'Battery Temperature on : ' +
options[str(Systems[sys])] + ' = ' + str(sum(tbat)/float(len(tbat))) + ' deg C'
            print Messg
            text_send_mail = text_send_mail + Messg + '\n'

text_send_mail = text_send_mail + '\n'
print ' '


# Housekeeping only, for battery voltage
Systems = [2,3,4,5,6]

subfolders = ['hskp']


# Check housekeeping voltages for systems 2 to 6
for sys in range(0, len(Systems)):
        SysDir = MainDir + "sys_" + str(Systems[sys])
    for subf in range(0, len(subfolders)):
        SubDirPath = SysDir + '/' + subfolders[subf]
        #print SubDirPath
        d2 = SubDirPath + '/' + dd
        #print d2
        # If the directory is missing, send missing data message:
        if not os.path.exists(d2):
            Messg = 'Missing '+str(dd)+' data in ' + options[str(Systems[sys])] + ' : ' + "s
subfolders[subf]
            flag = 1
            print Messg
            text_send_mail = text_send_mail + Messg + '\n'
        else:
```

```
            flag = 1;
            filelist = os.listdir(d2)
            #print filelist
            csvfile = d2 + '/' + filelist[1]
            #print csvfile
            f = gzip.open(csvfile, 'rb')
            reader = csv.reader(f)
            headers = reader.next()
            #print headers
            column = {}
            for h in headers:
                    column[h] = []
            #To get your numeric values into floats
            converters = [str.strip] + [float] * (len(headers) - 1)
            for row in reader:
                for h, v, conv in zip(headers, row, converters):
                    column[h].append(conv(v))
            tbat = column['V_batt_1']
            Messg = 'Battery Voltage on : ' + options[str(Systems[sys])]
+ ' = ' + str(sum(tbat)/float(len(tbat))) + ' V'
            print Messg
            text_send_mail = text_send_mail + Messg + '\n'

print ' '


if flag == 1:
    alert_subject = 'Summary of AAL-PIP Download on: ' + dd
    #print alert_subject
    #print text_send_mail
    EmailAlertCall( text_send_mail, alert_subject )
        print 'sending mail..'

print ' '
print ' '
```

AlertFunction.py

```
#def DstAlertCall( attach, text, Dst_subject ) :
# define a function to send email
def EmailAlertCall( text, alert_subject ) :
        import smtplib
        from email.MIMEMultipart import MIMEMultipart
        from email.MIMEBase import MIMEBase
        from email.MIMEText import MIMEText
        from email import Encoders
        import os

        # Username: AAL-PIP VTacc, Bday 12 Jan 1985
        gmail_user = "aalpipvt@gmail.com"
        gmail_pwd = "alert2aal-pip"
        gmail_mail_to = [ "aalpipvt@gmail.com", "kshitija@vt.edu", "rclauer@vt.edu",
```

```
"hyominkim.space@gmail.com", "zxu77@vt.edu"]
#   gmail_mail_to = [ "aalpipvt@gmail.com", "kshitija@vt.edu"]
        msg = MIMEMultipart()

        msg['From'] = gmail_user
        msg['To'] = "kshitija@vt.edu"
        msg['Subject'] = alert_subject

        msg.attach(MIMEText(text))

        # # For attachment
       # part = MIMEBase('application', 'octet-stream')
       # part.set_payload(open(attach, 'rb').read())
       # Encoders.encode_base64(part)
       # part.add_header('Content-Disposition',
       #         'attachment; filename="%s"' % os.path.basename(attach))
       # msg.attach(part)

        mailServer = smtplib.SMTP("smtp.gmail.com", 587)
        mailServer.ehlo()
        mailServer.starttls()
       # mailServer.ehlo()
        mailServer.login(gmail_user, gmail_pwd)
        mailServer.sendmail(gmail_user, gmail_mail_to, msg.as_string())
        mailServer.close()
```